Time-Dependent Crustal Deformation After Strong Earthquakes - Rheological Model Calculations

Francisco Lorenzo Martín

Thesis presented for the degree of
Doctor rerum naturalium
(Dr. rer. nat.)

Institute of Geology, Mineralogy and Geophysics
Faculty of Geosciences
Ruhr University Bochum
D-44780 Bochum
Germany

January 2006

A mis padres, Rocío y Francisco,
y a mis hermanos, Ernesto y Alberto.

Declaration

Hiermit erkläre ich, dass die Arbeit selbständig und ohne unerlaubte Hilfen ausgeführt und verfasst wurde und dass die Arbeit in dieser oder ähnlicher Form noch bei keiner Fakultät oder einer anderen Hochschule eingereicht wurde.

I declare that this dissertation represents my own work unless referenced to the contrary in the text. All references and other sources used have been appropriately acknowledged in the work. No part of this Thesis has been submitted elsewhere for the purpose of academic examination, either in its original or similar form.

Curriculum Vitae

Francisco Lorenzo Martín. Born in Madrid, June 8^{th} 1975.

- **EDUCATION**
  - PhD student on the subject: "*Time-dependent crustal deformation after strong earthquakes - rheological model calculations*", Ruhr University Bochum, Germany (since July, 2003)
  - MSc in Mathematics, major in Astronomy, Mechanics and Geodesy, Universidad Complutense de Madrid (Sept. 1993 - June 1998)
  - Two years of additional lectures, specializing in Computer Science (Sept. 1996 - Sept. 1998)
- **EMPLOYMENT HISTORY**
  - GeoForschungsZentrum Potsdam, Germany. Scientific assistant for the projects:
    - "*Assessing and forward planning of the Geodetic And Geohazard Observing System for GMES applications (GAGOS)*". Identify user needs for seismic, volcanic and landslide hazard information, assess the most required observables and related observational infrastructure and evaluate the existing observational techniques, networks and modeling capabilities against the user requirements. (January, 2006 - March 2006)
    - "*Modeling of deformation and stress at fault zones*". Analysis of a sequence of earthquakes at the North Anatolian Fault zone, to asses the importance of viscoelastic relaxations in the stress transfer process. (August, 2005 - December 2005)
  - Ruhr University Bochum, Germany (Collaborative Research Center 526: "*Rheology of the Earth, from the upper crust to the subduction zone*"). Scientific collaborator with the projects:
    - "*Time-delayed tectonic effects and interactions of earthquakes*". Extraction of rheological information from the time delay in a sequence of earthquakes, considering the inelastic behavior of the Earth. Intensive use of FORTRAN77 and MATLAB. (July, 2002 - June, 2005)
    - "*Extraction of rheological parameters from modeling of time-dependent crustal deformation*". Use of geodetic data for assessing the time-dependent deformation of the Earth's surface as a basis to derive rheological parameters of the crust and upper mantle. Development of new

  FORTRAN77 code for calculating co- and post-seismic deformations and geopotential changes. (May, 2000 - June, 2002)

- GeoForschungsZentrum Potsdam, Germany. Scientific assistant with the subject:
  - "*Calculation of the co-seismic surface deformation caused by an earthquake nearby a mega-city with proof of the significance of different scenarios considering the historical seismicity and the variations in the focal parameters*". Development of FORTRAN77 and MATLAB software for the calculation of quasi-static deformations, strain, stress and tilt fields in a layered Earth model. (February, 1999 - April, 2000)

- **PUBLICATIONS**

  - Francisco Lorenzo Martín, Frank Roth and Rongjiang Wang, 2006. "*Elastic and inelastic triggering of earthquakes in the North Anatolian Fault zone*", Tectonophysics, vol. 424, issue 3-4, pp. 271-289.
  - Francisco Lorenzo Martín, Frank Roth and Rongjiang Wang, 2006. "*Inversion for rheological parameters from postseismic surface deformation associated to the 1960 Valdivia earthquake, Chile*", Geophys. J. Int., vol 164, pp. 7587.
  - Rongjiang Wang, Francisco Lorenzo Martín and Frank Roth, 2006. "*PSGRN/PSCMP - a new code for calculating co-postseismic deformations and geopotential changes based on the viscoelastic-gravitational dislocation theory*", Computers & Geosciences, vol. 32, pp. 527541.
  - Rongjiang Wang, Francisco Lorenzo Martín and Frank Roth, 2003. "*Computation of deformation induced by earthquakes in a multi-layered elastic crust - FORTRAN programs EDGRN/EDCMP*", Computers & Geosciences, vol. 29/2, pp. 195 - 207.
  - Francisco Lorenzo Martín, Rongjiang Wang and Frank Roth, 2002. "*The effect of input parameters on visco-elastic models of crustal deformation*", Física de la Tierra, vol. 14, pp. 33-54.

Acknowledgements

This work was supported by the Deutsche Forschungsgemeinschaft under grant SFB 526 (Collaborative Research Centre 'Rheology of the Earth - from the Upper Crust to the Subduction Zone') at the Ruhr University Bochum, and by the GeoForschungsZentrum Potsdam. I am very much indebted to these institutions, and especially to Prof. Dr. Bernhard Stöckhert and to Prof. Dr. Jochen Zschau, for granting me the opportunity to carry out the present work, and to Agnes Absch and Heide Vogler for their prompt and friendly help with the many bureaucratic issues.

I want to thank my supervisor, Frank Roth, for his guidance and patience during these years. Also to Wang Rongjiang, who helped me so much to understand the mathematics behind the methods used in my work.

Stefano Parolai and Sandra Richwalski have been absolutely fundamental for me during these years, both at the professional level and, very specially, at the personal one. They have been a model to follow in many different aspects. I am also deeply indebted to José Fernández, Kristi Tiampo and Roland Bürgmann, who taught me so much about the way science should be done; to several reviewers, who carefully read and helped improve the papers I worked on; and to many colleagues, for endless discussions from which I profited so much: Claus and Regina Milkereit, Helmut Grosser, Jürgen Klotz, Heiko Woiht, Peter Bormann... Very special thanks to Birger Lühr, who kept me from quitting on one occasion.

A big thank-you goes to many friends who are (or were) in the juncture of writing a PhD thesis: I will never forget the friendship, support and help of Kevin Fleming (who gave me a hand with my English so often. Thanks, mate!), Sylvia Mackenberg, Eleonora Rivalta, Gregor Hillers, Daniel Melnick, Amérika Manzanares, Benjamín Heit, Gia Khazaradze, Monika Sobiesiak, Dagmar Kesten and so many others.

Of course, my "not-academic" friends also deserve my greatest gratitude, for supporting, distracting and putting up with me at many moments. Very specially, I want to thank María, who got to share the last (and hardest) times of my PhD; the whole Pandicuqui, who never stopped polemising, discussing, entertaining and making fun of... well, of everything, basically; my many old house-mates at the Charlotte and of course so many other "assorted" great friends: Andrea, Anna, Antje, Matthias, Frederik and Ari, Jenny, Karin, Ciaron, Richard...

Finally, and most importantly, I want to deeply and sincerely thank my loving parents and brothers, who always accepted my decisions and always stayed very close to me despite the distance.

Thank you all so much! You will be the best memories of my PhD life.

Contents

Declaration v

Curriculum Vitae vii

Acknowledgements ix

1 Introduction 1

2 Computation of co- and post-seismic deformation induced by earthquakes in a multi-layered half-space 7

2.1 Description of the boundary-value problem 8
2.2 Application of the Hankel transform 10
2.3 Thomson-Haskell propagator algorithm 12
2.4 The improved propagator algorithm 14
2.5 Convergence problems of the numerical Hankel transform 15
2.6 A consistent approach for including the gravitational effect 16
2.7 Implementation of the rheology 19
2.8 A practical anti-aliasing technique 20
2.9 Computation procedures 21
2.10 Comparisons with previously published results 23
2.11 Summary 25

3 The effect of input parameters on viscoelastic models of crustal deformation 29

3.1 Introduction 29
  3.1.1 Motivation 29
  3.1.2 Modeling 30
3.2 Variability analysis 31
  3.2.1 Reference Model 31
  3.2.2 Input parameters 32
  3.2.3 Stability 33
  3.2.4 Effect of input parameters on co-seismic deformation 33
  3.2.5 Effect of input parameters on post-seismic deformation 37
  3.2.6 Distance to the fault plane 37
  3.2.7 Effect of single input parameters 40
3.3 Conclusions 42

4 Inversion for rheological parameters from post-seismic surface deformation associated with the 1960 Valdivia earthquake, Chile 45
4.1 Introduction 46
4.2 The 1960 Valdivia earthquake 48
  4.2.1 Tectonic setting and seismicity 49
  4.2.2 Mechanism and location 49
  4.2.3 Coseismic slip on the rupture surface 50
  4.2.4 Rupture surface geometry 50
4.3 Modeling 51
4.4 Results and discussion 56
  4.4.1 Parameter inversion 56
  4.4.2 Trade-off 58
  4.4.3 Horizontal velocity components 59
  4.4.4 Measurability and time-dependency of the deformation rates . . 62
4.5 Conclusions 62

5 Elastic and inelastic triggering of earthquakes in the North Anatolian Fault zone 65
5.1 Introduction 66
5.2 Tectonic setting 69
5.3 Methodology 70
5.4 Model parameters 70
5.5 Results 72
  5.5.1 Coulomb stress on the rupture surfaces 73
  5.5.2 Coulomb stress at the epicenters 76
  5.5.3 The 1999 Izmit and Düzce events 76
  5.5.4 The Marmara Sea region 78
5.6 Discussion 79
  5.6.1 Coulomb stress on the rupture surfaces and at the epicenters . . 79
  5.6.2 The 1999 Izmit and Düzce events 81
  5.6.3 The Marmara Sea region 85
5.7 Conclusions 86

6 Summary and conclusions 89

Bibliography 91

Appendix 109

A Expansion of the deformation field equation in terms of poloidal and toroidal modes 109
A.1 Introduction to the Hankel transform 109
A.2 Hankel transform of Hooke's law 112
  A.2.1 Derivative of the displacement wavenumber spectrum $U_m(z,k)$. 113
  A.2.2 Derivative of the displacement wavenumber spectrum $V_m(z,k)$. 115
  A.2.3 Derivative of the displacement wavenumber spectrum $W_m(z,k)$. 116
A.3 Hankel transform of the equations of motion 117

A.4 The poloidal- and toroidal-mode systems 123

B Previous published modeling results for gravitational viscoelastic post-seismic relaxation on a layered Earth model 125

List of Figures

2.1 Schematic representation of a layered Earth model. 9
2.2 Model of the SLS rheology. 20
2.3 The flowchart of major subroutines of the program **PSGRN**. 22
2.4 The flowchart of major subroutines of the program **PSCMP**. 22
2.5 Schematic representation of the reference system for **PSCMP** 23
2.6 Coseismic and additional post-seismic surface displacement calculated for two Earth models, for a profile perpendicular to the fault strike through the center of the rupture surface. 24
2.7 Same as Fig. 2.6, but for a buried thrust fault dipping at 30 degree. . . 26

3.1 Schematic representation of the geometry of the fault and the medium used in the modeling. 32
3.2 Averaged absolute deviations from the RM (mm) for the horizontal post-seismic displacement (first 2 years after the event) for different sets of parameters. 34
3.3 Co-seismic horizontal displacement (U_y) for a trace of points perpendicular to the strike of the fault plane. Dependence on dip angle. 35
3.4 Co-seismic horizontal displacement (U_y) for a trace of points perpendicular to the strike of the fault plane. Dependence on elastic layer thickness. 36
3.5 Horizontal post-seismic (first two years after the event) displacement perpendicular to the strike of the fault plane for a trace of points perpendicular to the strike of the fault plane. 37
3.6 Deviations from the RM (mm) for the post-seismic displacement for the first two years after the event for points A, B and C, as indicated in Fig. 3.5. 39
3.7 Horizontal post-seismic (first two years after the event) displacement perpendicular to the strike of the fault plane for a trace of points perpendicular to the strike of the fault plane. 41

4.1 Map of the study area. 46
4.2 Schematic representation of the fault geometry and medium used in the modeling. 53
4.3 Dependence of the deviation (Δ, Eq. 4.2) against each considered parameter. 57
4.4 Trade-off between pairs of the studied parameters. 60
4.5 Horizontal velocity components in the W-E and S-N directions for three latitude intervals (areas A, B and C, Fig. 4.1). 61

4.6 Isochrones for the measurability of the deformation caused by post-seismic relaxation. 63
4.7 Horizontal velocities in the W-E direction for a trace of points at 40^o S. 64

5.1 Map showing the major tectonic elements of Turkey. 67
5.2 Space-time migration of the 10 considered $M_s > 6.5$ earthquakes along the NAF in the period 1939 to 1999. 68
5.3 Graphical representation of Coulomb stresses. 71
5.4 Parameters of the horizontally stratified medium. 72
5.5 Evolution of the Coulomb stress field since 1939. 75
5.6 Time-evolution of Coulomb stress on the epicenters of the considered events (Table 5.1). 77
5.7 Variation of the Coulomb stress changes when possible inaccuracies in the epicentral location are considered. 78
5.8 Coulomb stress change at 10 km depth on optimally oriented fault planes and on given faults in the area around the 1999 Izmit and Düezce events. 79
5.9 Coulomb stress change at 10 km depth on optimally oriented fault planes and on given faults in the Marmara Sea area. 85

B.1 Co-seismic and additional post-thrusting displacement at the surface. . 126
B.2 Co-seismic and post-strike-slip displacement at the surface. 127
B.3 Surface displacements due to a dipping thrust fault in an elastic layer over a viscoelastic half-space and in an elastic-gravitational layer over a viscoelastic-gravitational half-space. 128

List of Tables

1.1 Published solutions for 3-D static deformation induced by earthquakes in a layered half-space 4

2.1 Hankel transformed source functions in the cases of a point single force and a point dislocation 12

3.1 Value list for the model parameters that lead to the top or bottom values for horizontal displacements when the three parameters change. 38
3.2 Value list for the model parameters that lead to the top or bottom values for horizontal displacements when one of the parameters changes. . . . 40

4.1 GPS site velocities from the SAGA network used in the modeling. . . . 52
4.2 Medium model parameters. 53
4.3 Parameter values corresponding to the best-fitting models for four different assumptions about the origin of the deformation. 59

5.1 Parameters of the sequence of earthquakes used. 69
5.2 Maximum and average Coulomb stress changes ($\Delta\sigma_c$) on the ruptures immediately before each considered event. 75
5.3 Percentage of fault rupture showing $\Delta\sigma_c \geq 0.01$ MPa. 76
5.4 Percentage of fault rupture showing $\Delta\sigma_c \geq 0.01$ MPa. 83

Chapter 1

Introduction

Until the beginning of the 20^{th} century, it was thought that ruptures of the surface observed after a strong earthquake were the result of strong ground shaking rather than the other way around. This interpretation changed following the great 1906 earthquake in San Francisco, when Henry Fielding Reid examined the displacement of the ground surface around the San Andreas Fault (Reid, 1910). From his observations, he concluded that the earthquake must have been the result of the elastic rebound of previously stored elastic-strain energy in the rocks on either side of the fault. Geodetic measurements and other evidence confirmed Reid's theory for the movement of the Earth's crust in the so-called seismic cycle. However, traditional methods were for a long time inadequate to measure the deformation caused by a strong shock with more accuracy than several centimeters (e.g. Plafker and Savage, 1970).

The arrival of space geodetic techniques improved the quality of the observations, making measurement campaigns easier, faster and accurate down to a couple of millimeters (see e.g., Klotz et al., 2001; Jacobs et al., 2002; Fialko, 2004). At once, measurements could be carried out both more frequently and more accurately, allowing for the detailed study of time–dependent crustal deformation processes. The slow and small–magnitude nature of these processes has strongly hindered our study of them. However, as the number of stations and campaigns using the Global Positioning System (GPS) increased and, at the same time, more and more Interferograms of Synthetic Aperture Radar (InSAR) data were generated, crustal deformation became visible with higher accuracy and over shorter time intervals.

Based on these developments, the study of deformation associated with strong earthquakes underwent remarkable improvements. Usually, measurements deal with the displacement (e.g. Deng et al., 1998; Freymueller et al., 2000). Additionally, the observed surface displacement after a strong earthquake can be used to infer the slip distribution on its rupture surface (e.g. Reilinger et al., 2000; Bürgmann et al., 2002), and this slip distribution can then be used as an input to model the stress change caused by the shock (e.g. Parsons, 2004). As a consequence, the analysis of earthquake interactions by means of stress transfer has progressed over the last few years parallel to that of the surface deformation. Although the matter of earthquake triggering by stress transfer had been the subject of previous studies (e.g. Healy et al., 1968; Raleigh et al., 1972), during the 1990s the work of several researchers (e.g. King et al., 1994) brought it back into discussion. Since then, the work of numerous research groups around the world has lead to notable improvement in our understanding of earthquake interaction. However, partly due to the novelty of the subject, but mainly due to the lack of an appropriate methodology, the analysis of stress transfer has been limited mainly to that of the elastic co-seismic quasi-static deformation, and even today an important percentage of studies disregard time-dependent post-seismic stress changes (see Freed, 2005; Steacy et al., 2005).

The increase in the accuracy, frequency and coverage of the measurements has provided material for various and still open debates. Although viscoelastic relaxation processes are known to take place, the deformation caused by them is slow. In most cases, the time interval covered by accurate measurements is too short to provide adequate information as to the rate or the kind of temporal development of the deformation. Because of this, estimations for the value of the viscosity of the lower crust and/or upper mantle range by several orders of magnitude, depending not only on the study region (e.g. Pollitz and Sacks, 2002; Piersanti, 1999), but also on the source process causing the relaxation (e.g. James et al., 2000; Hu et al., 2004). In a similar way, it is also not clear yet which rheological model is more adequate to describe the time evolution of the relaxation process. The rheology of a Standard Linear Solid body properly reproduces transient deformation immediately after an earthquake (Cohen, 1982; Pollitz et al., 1998), whereas Maxwell bodies better describe the deformation process once the steady state has been reached (e.g. Khazaradze et al., 2002). According to recent studies, non-linear rheologies could be the most adequate to analyze post-seismic relaxation processes (Freed and Bürgmann, 2004). However, as mentioned before, deformation records are usually either not long enough or their accuracy is insufficient to derive information about the rheological model to better describe these processes.

Probably the most important open questions about post-seismic deformation are which processes are significantly involved in the observed deformation, to what extent, and how far and how long from the triggering event can their effects be observed. Apart from relaxation (e.g. Zweck et al., 2002; Hu et al., 2004), in certain cases other time–dependent processes have been shown to provide an adequate explanation for observed deformations. Examples of these can be velocity-strengthening frictional afterslip (Hearn et al., 2002; Bürgmann et al., 2002), poroelastic rebound (Peltzer et al., 1998; Jónsson et al., 2003) or shear zone strength changes after an earthquake (Montesi, 2004).

As mentioned, displacement measurements can lead to information about the stress field. In general, measurements of some facets of the deformation process can be used to gain insight into other aspects that are not easy to measure. For this, computer modeling is an essential and powerful tool. The development of computer tools and methods to model co- and post-seismic deformation associated with earthquakes run parallel to that of the quality of the measurements. At the first stage, methods and programs to model deformation in a homogeneous elastic half-space were progressively developed under different assumptions and gradually improved. The culmination of this progress was the publication by Okada (1992) of his unified formulation for the internal deformation due to shear and tensile faults in an elastic half-space, a work that is still widely in use today.

For static-elastic deformation in a layered half-space, Table 1 provides an overview of published numerical techniques and software. Most of these methods are based on the wavenumber integration method. From the beginning it was clear that - in contrast to the homogeneous half-space - the wavenumber spectra or kernel functions obtained for the stratified case could not be integrated analytically, so that either the integration should be carried out numerically (cf. Sato, 1971; Sato and Matsu'ura, 1973) or the integrals should be approximated (Ben-Menahem and Gillon, 1970; Jovanovich et al., 1974a; Roth, 1983).

A practical problem is that the number of calculations for the kernel functions increases exponentially with the number of layers. Because of this, algorithms based on analytical or semi-analytical methods were essentially limited to no more than four layers over the half-space (cf. Roth, 1992). Another way to compute the kernel functions is to adopt the propagator algorithm, which was first applied by Thomson (1950) and Haskell (1953) to seismic wave propagation in layered media. Although the formulation of the propagator algorithm was very clear and could be applied to an unlimited number of layers, its numerical results showed the same instability known from dynamic solutions (see for instance Sato, 1971). To overcome these, mathematical improvements in the algorithm were introduced (cf. Dunkin, 1965; Jovanovich et al., 1974a; Roth, 1983). The success was clearly visible but remained limited, until Wang (1999b) approached the problem from a physical point of view and proposed an algorithm that avoids numerical operations between incident waves from the source at each layer interface.

Since the late 1960s, several steps were taken to obtain methods for modeling post-seismic effects more comprehensively. The first attempts to provide inelastic models were made for the 3D deformation field of an elastic crust above a viscoelastic half-space with different rheologies (Braslau and Lieber, 1968; Rosenman and Singh, 1973a,b; Singh and Rosenman, 1974; Nur and Mavko, 1974). For a review of the progress in these efforts until the late 1990's, see Roth (1994) and Piersanti et al. (1997). Gravitational effects were first introduced by Rundle (1980b,a, 1981, 1982), with the assumption of depth-independent gravitational acceleration. Between 1994 and 1996, several subsequent papers were published that presented the viscoelastic-gravitational dislocation theory and the corresponding numerical tools (see Fernández and Rundle, 1994a,b; Fernández et al., 1996a,b; Yu et al., 1996a,b). These were followed by similar approaches for the case of magma intrusions (Folch et al., 2000; Fernández et al., 2001), using the source presentation of Bonafede (1990). Recently, Wang (2005a) found an incorrect formulation included in the earlier treatment of the gravity effect. This resulted in new approaches to solve the problem by Fernández and Rundle (2004) and Wang (2005b). Finally, the effects of earthquakes on a spherical Earth have been considered. From the early works of Ben-Menahem and Israel (1970) and Smylie and Mansinha (1971), subsequent improvements led to several different modeling approaches currently in use, most notable the works of Piersanti et al. (1997) and Pollitz (1997).

In this thesis, a numerical tool for the calculation of post-seismic deformation, PSGRN/PSCMP (Wang et al., 2006), was used. This tool can be used to determine the surface and subsurface time-dependent deformation, as well as changes in the geoid and gravity, produced by dislocation sources embedded in a mixed elastic/inelastic layered half-space. This software uses the elastic-viscoelastic correspondence principle (e.g. Christensen, 1971), which states that a linear viscoelastic boundary-value problem can be solved by adopting the associated elastic solutions in which the elastic moduli

Table 1.1: *Published solutions for 3-D static deformation induced by earthquakes in a layered half-space**

Publication	Source type				Source orientation			Source size point (P) extended (E)	Deformation type displacement (D) or strain (S)	Number of layers**	Gravity‡ included (G)	Remarks
	strike-slip	dip-slip	ex-tens.	ex-plosion	verti-cal	hori-zontal	in-clined					
Ben-Menahem and Singh (1968)	✓	✓		✓	✓	✓		P	D	2		1)
Sato (1971)	✓	✓			✓	✓	✓	E	D	7		
Singh (1971)	✓	✓		✓	✓			P	D	-		2)
Wason and Singh (1972)	✓	✓		✓	✓			P	D	-		3)
Sato and Matsu'ura (1973)	✓	✓		✓	✓	✓	✓	E	D	5		4)
Jovanovich et al. (1974a)	✓	✓		✓	✓	✓	✓	P	D	4		
Jovanovich et al. (1974b)	✓	✓		✓	✓	✓	✓	P	S	5		5)
Matsu'ura and Sato (1975)	✓	✓			✓	✓	✓	E	S	5		4)
Rundle (1980b)	✓	✓			✓			P	D	-	G	6)
Rundle (1981)	✓	✓			✓			E	D	2	G	6)
Rundle (1982)	✓	✓		✓	✓	✓	✓	E	D	2	G	7) †
Roth (1983)	✓	✓		✓	✓	✓	✓	P	D & S	4		8) †
Ma and Kusznir (1992)	✓	✓			✓	✓	✓	E	D	4		9)
Roth (1993)			✓		✓			P	D	3		8)
Fernández and Rundle (1994b)				✓	-	-	-	P	D	3	G	10)
Ma and Kusznir (1994a)	✓				✓			E	D & S	4		†
Ma and Kusznir (1995)		✓			✓	✓	✓	E	D & S	4	G	†
Fernández et al. (1996b)		✓			✓	✓	✓	E	D	2	G	11) †
Yu et al. (1996a)	✓				✓	✓	✓	E	D	2	G	12) †
Fernández et al. (1997)				✓	-	-	-	P	D & S	5	G	13)
Wang (1999b)	✓	✓	✓	✓	✓	✓	✓	P	D	∼ 500		14)
Fernández et al. (2001)				✓	-	-	-	P	D	3	G	15) †
PSGRN/PSCMP	✓	✓	✓	✓	✓	✓	✓	E	D & S	∼ 500		16)

* If not stated otherwise, sources are discontinuities (dislocations) in displacement, Lamé's constants can be chosen independently, the medium is elastic, and fields are given at the surface.

** Layer number limit given in the paper or maximum number of layers shown in an example. The half-space below the layers is included in the layer count. '-' indicates that only formulae are given, but no examples.

† The modelling of inelastic behaviour is included, usually as some approximation.

‡ Gravity effects are included in one of two usually used approximations. For more details see Rundle (1980b) or Piersanti et al. (1997) for an overview.

1) Only the integrals are given for the displacements.
2) Here, sources are discontinuities in stress. The paper also treats the dynamic case.
3) The medium is a layered sphere.
4) The rupture plane can extend through several layers, but see Morelli et al. (1987) or Bonafede and Rivalta (1999) for a more physical treatment.
5) The formulae for all surface strains and tilts are given (in cylindrical coordinates).
6) The displacements are given only in the integral form, the solution of which can be found in Rundle (1980a).
7) Only the vertical displacements are given in the integral form, the solution can be found in Rundle (1980a).
8) Later subsurface deformations were added (see Roth, 1990). Examples for 4 layers see also in Roth (1992, 1994).
9) Includes subsurface displacement and strain fields, elliptical source shapes, and variable slip distributions across the rupture plane; extended to visco-elastic gravitational media in Ma and Kusznir (1994b).
10) Programme code published in Fernández and Rundle (1994a).
11) Only horizontal displacements. Programme code published in Fernández et al. (1996a).
12) Programme code published in Yu et al. (1996b).
13) Possibility to include a water layer at the free surface. Besides strain, tilt can also be computed. Includes programme code.
14) The accuracy and performance was considerably increased with this algorithm (see text). The number of layers is practically unlimited. The dynamic case is also treated.
15) More than one inelastic layer.
16) See footnote 14 for accuracy, performance and layer number.

are replaced by the Laplace or Fourier transformed complex moduli. The time-domain solutions are then obtained using the inverse transform.

Because of the complicated non-linear relationship between geophysical observables and subsurface structure, a direct inversion for rheological parameters is in general difficult. Since PSGRN/PSCMP provides a forward modeling tool, usually a large set of models must be run to select the best-fitting one. Therefore, the efficiency of the software and the stability of its numerical results are crucial. For this purpose, several effective techniques (orthonormalized Thomson-Haskell propagator, analytical asymptotes, filter techniques, etc.) were used to solve the stability and convergence problems when computing the Green's functions (Wang, 1999b; Wang et al., 2003; Wang and Kümpel, 2003). The result is an easy to use, high performing software, with respect to both speed and accuracy. **Chapter 2** deals with the mathematical background of the method used in PSGRN/PSCMP, including the techniques applied to improve the accuracy and speed of the calculations.

This software, in combination with high quality data, can be used to extract details about the space-time development of tectonic processes, especially earthquake-related crustal deformations, and their basic rheological parameters. However, the variables that influence these processes are numerous and the way they affect the deformations is very different. Therefore, it is important to study the effect that the variation of the input parameters have on the modeled results before trying to model observed crustal deformation. In **Chapter 3**, we provide such a sensitivity analysis and offer an interpretation of the results, with suggestions as to what kinds of deformation data are more appropriate to study each parameter.

The information obtained by the sensitivity analysis, however, cannot always be applied directly when modeling real data. This is shown in **Chapter 4**, where we model post-seismic crustal deformation associated with the great 1960 Chilean earthquake (often also referred to as the Valdivia earthquake). For this event, deformation measurements are only available several tens of kilometers away from the area located directly over the inferred rupture surface. The region over the rupture surface, according to our results in Chapter 3, would be the most appropriate one to extract information about the rheological properties of the crust and upper mantle in the region. However, since the 1960 event occurred offshore, measurements in such a region are not available. Nevertheless, a careful and systematic study led to important conclusions, including the identification of viscoelastic relaxation as the cause of the observed anomalous deformation, information about the rheology of the region, as well as predictions of the future development of the deformation. According to our results, the deformation associated with the post-seismic relaxation process after the Valdivia event can still be observed today, and will still be measurable for several decades. It should therefore be taken into account for any application considering crustal deformation.

From the analysis of the stress field, we also conclude that the effects of viscoelastic relaxation should not be neglected. In **Chapter 5** we present results dealing with the stress changes due to strong earthquakes striking along the North Anatolian Fault zone, Turkey, since 1939. Plate motion and co-seismic stress change are usually the only two sources considered for the estimation of stress increase/decrease, and calculations are usually carried out considering only the elastic behavior of the medium. However, according to our results, the stress increase due to viscoelastic relaxation after a strong event is comparable, and sometimes larger, than that corresponding to plate motion. Therefore, it is not an acceptable simplification to limit similar studies to plate motion and elastic co-seismic stress changes, and the exclusion of viscoelastic post-seismic effects may neglect an important part of the actual stress change.

In summary, the results presented in this thesis demonstrate that the methodology and software used provide adequate and powerful tools for the calculation of co- and, especially, post-seismic deformation associated with earthquakes. The tools themselves and the results from their application, both theoretical and applied, are of use to very different fields of geophysics, from modeling the of deformation to earthquake probability calculation and seismic-hazard assessment. The viscoelastic relaxation process after a strong earthquake has an effect on the deformation field that cannot be neglected, and the PSGRN/PSCMP software provides an optimum way to model it appropriately.

The contents of this thesis that have been published are listed below:

- **Chapter 2**:
  - Wang, R., F. Lorenzo Martín, F. Roth, 2003. *Computation of deformation induced by earthquakes in a multi-layered elastic crust - FORTRAN programs EDGRN / EDCMP.* Computers & Geosciences, 29 (2): 195-207,
  - Wang, R., F. Lorenzo Martín, F. Roth, 2006. *A semi-analytical software PSGRN/PSCMP for calculating co- and post-seismic deformation on a layered viscoelastic-gravitational half-space.* Computers & Geosciences, 32: 527541 (doi: 10.1016/j.cageo.2005.08.006).
- **Chapter 3**:
  - Lorenzo Martín, F., R. Wang, F. Roth, 2002. *The effect of input parameters on viscoelastic models of crustal deformation.* Física de la Tierra, 14: 33-54.
- **Chapter 4**:
  - Lorenzo Martín, F., F. Roth, R. Wang, 2006. *Inversion for rheological parameters from post-seismic surface deformation associated to the 1960 Valdivia earthquake, Chile.* Geophys. J. Int., 164: 7587 (doi: 10.1111/j.1365-246X.2005.02803.x).
- **Chapter 5**:
  - Lorenzo Martín, F., F. Roth, R. Wang, 2006. *Elastic and inelastic triggering of earthquakes in the North Anatolian Fault zone.* Tectonophysics, 424 (3-4): 271-289 (doi: 10.1016/j.tecto.2006.03.046).

Chapter 2

Computation of co- and post-seismic deformation induced by earthquakes in a multi-layered half-space

The methodology adopted for the results presented in this thesis has been developed during the last years by Wang Rongjiang and his co-workers, and can be found in several publications. Wang (1999b) presented the basic structure of the method for stable and efficient computation of Green's functions in a multi–layered half–space. His approach was later used for solving elastic (Wang et al., 2003), poroelastic (Wang and Kümpel, 2003), and viscoelastic problems (Wang et al., 2006). Also, two recent papers (Wang, 2005a,b) proposed a new and consistent approach for including the gravity effects in plane-Earth models. In the following we compile the results presented in the mentioned papers in a systematic way, in order to provide a clear overview of the methodology used in the subsequent Chapters. First, the solution to the static elastic problem is given. Then, the effects of gravity are included and the solution is extended into the viscoelastic case.

In the first place, the equations of the elastic boundary-value problem are obtained. Using the Hankel transform, the partial differential equations of motion are converted into a set of ordinary differential equations governing the deformation field in the wavenumber domain. For each homogeneous layer, all fundamental solutions of the latter equation are given in closed analytical form. The special solution satisfying the source and boundary conditions will be obtained by the Thomson-Haskell propagator algorithm. When the wavenumber domain problem has been solved, the desired deformation field in the spatial domain is then obtained through the inverse Hankel transform. In general, Green's functions are calculated for four fundamental different dislocations sources (the strike-slip double-couple, the dip-slip double-couple, the compensated linear vertical dipole (CLVD) and the point inflation) at different depths, so that any finite dislocation can be modeled via linear superposition. Theoretically, all calculations in the propagator algorithm are based on analytical formulae. Only the inverse Hankel transform has to be carried out numerically. In practice, however, numerical problems appear in both procedures above.

According to the correspondence principle, the same propagator algorithm used in the static elastic case can be adopted to compute the spectral Green's functions. The time-dependent inelastic Green's functions are then obtained by the Fast Fourier Transform (FFT), extended with an anti-aliasing technique that ensures numerical stability when calculating the post-seismic transients. Moreover, the coupling between the deformation and the Earth's gravity field is considered, so that results are obtained not only for the complete deformation field consisting of 3 displacement components, 6 stress (strain) components and 2 tilt components, but also the geoid and gravity changes.

2.1 Description of the boundary-value problem

For an isotropic and elastic medium, Hooke's linear constitutive relation between the stress and strain holds,

$$\sigma_{ij} \;=\; \lambda \varepsilon_{kk} \delta_{ij} + 2\mu \varepsilon_{ij}, \tag{2.1}$$

where σ_{ij} and ε_{ij} are the components of the stress and strain tensors, λ and μ are the two elastic parameters termed Lamé's constants and δ_{ij} is the Kronecker delta. The summation convention applies, that is, $\varepsilon_{kk} = \varepsilon_{11} + \varepsilon_{22} + \varepsilon_{33}$. The strain components are related to the derivatives of the the displacement as follows:

$$\varepsilon_{ij} \equiv \frac{1}{2}\left(\frac{\partial u_i}{\partial x_j} + \frac{\partial u_j}{\partial x_i}\right), \tag{2.2}$$

where u_i are the components of the displacement vector, $\mathbf{u}$.

Using tensor notation, Eq. 2.1 can be written as

$$\mathbf{\Gamma} \;=\; (\lambda \nabla \cdot \mathbf{u})\, \mathbf{I} + \mu \left(\nabla \mathbf{u} + (\nabla \mathbf{u})^t\right), \tag{2.3}$$

where boldface denotes a vector, $\mathbf{\Gamma}$ is the stress tensor, $\mathbf{I}$ is the unit tensor and $(\nabla \mathbf{u})^t$ denotes the tensor transpose of $\nabla \mathbf{u}$.

The partial differential equations governing the static deformation in an elastic medium are given by the equilibrium conditions of forces,

$$\nabla \cdot \mathbf{\Gamma} + \mathbf{f} \;=\; \mathbf{0}, \tag{2.4}$$

where $\mathbf{f}$ is the body force representing the source. In combination with Hooke's law, the governing equations can be written in terms of displacements of the medium. We have

$$\begin{aligned}
\nabla \cdot \mathbf{\Gamma} \;&=\; \nabla \cdot \left((\lambda \nabla \cdot \mathbf{u})\, \mathbf{I} + \mu \left(\nabla \mathbf{u} + (\nabla \mathbf{u})^t\right)\right) \\
&=\; \lambda \nabla \cdot \begin{pmatrix} u_{k,k} & 0 & 0 \\ 0 & u_{k,k} & 0 \\ 0 & 0 & u_{k,k} \end{pmatrix} + \mu \nabla \cdot \begin{pmatrix} 2u_{1,1} & u_{1,2} + u_{2,1} & u_{1,3} + u_{3,1} \\ u_{2,1} + u_{1,2} & 2u_{2,2} & u_{2,3} + u_{3,2} \\ u_{3,1} + u_{1,3} & u_{1,3} + u_{3,1} & 2u_{3,3} \end{pmatrix} \\
&=\; (\lambda + 2\mu)\, \nabla \left(\nabla \cdot \mathbf{u}\right) - \mu \begin{pmatrix} u_{1,22} - u_{2,12} - u_{3,13} + u_{1,33} \\ u_{2,11} - u_{1,21} - u_{3,23} + u_{2,33} \\ u_{3,11} - u_{1,31} - u_{2,32} + u_{3,22} \end{pmatrix} \\
&=\; (\lambda + 2\mu)\, \nabla \left(\nabla \cdot \mathbf{u}\right) - \mu \nabla \times \left(\nabla \times \mathbf{u}\right),
\end{aligned} \tag{2.5}$$

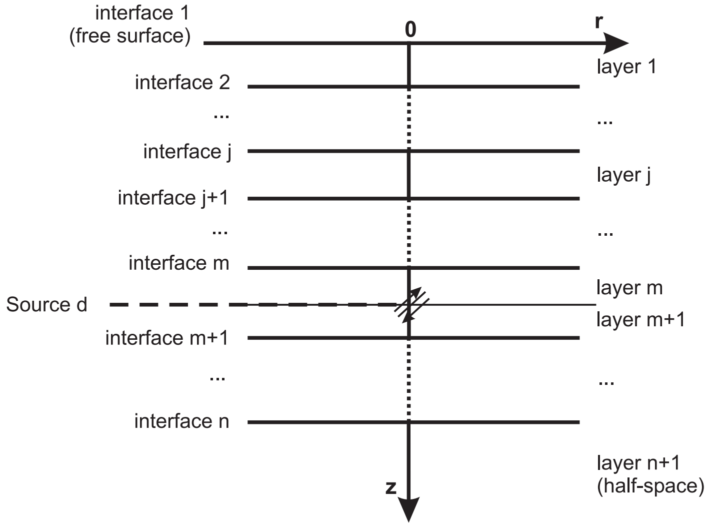

Figure 2.1: *Schematic representation of a layered Earth model. Within each layer, rock parameters are homogeneous and the deformation equation in a homogeneous medium applies (Eq. 2.7). At the interfaces, displacement and stress must satisfy the continuity conditions, given by Eqs. 2.8 and 2.9. For convenience, the plane at the source depth will be defined as a pseudo interface.*

where the subindex behind the coma represents a partial derivative, that is

$$u_{i,j} \equiv \frac{\partial u_i}{\partial x_j}. \tag{2.6}$$

Therefore Eq. 2.4 reads

$$(\lambda + 2\mu)\,\nabla\,(\nabla \cdot \mathbf{u}) - \mu\nabla \times (\nabla \times \mathbf{u}) + \mathbf{f} \;=\; \mathbf{0}. \tag{2.7}$$

If we consider a layered medium, as depicted in Fig. 2.1, displacement and stress satisfy the continuity conditions at an interior material interface

$$\mathbf{u}\,\Big|_{-}^{+} \;=\; \mathbf{0}, \tag{2.8}$$

$$\mathbf{e}_n \cdot \mathbf{\Gamma}\,\Big|_{-}^{+} \;=\; \mathbf{0}, \tag{2.9}$$

where $\mathbf{e}_n$ is the unit normal vector of the interface, and the symbol $\Big|_{-}^{+}$ denotes the increment of the respective quantity from one side to the other side of the interface. The stress-free surface is expressed by

$$\mathbf{e}_n \cdot \mathbf{\Gamma} \;=\; \mathbf{0}. \tag{2.10}$$

In the Green's function approach, the function $\mathbf{f}$ describes a point source. For convenience in numerical calculations, the plane at the source depth will be defined as a pseudo interface. Then, the point source can be represented by a jump of the displacement and stress components. In case that $\mathbf{f} = \mathbf{f}_s\delta(z - z_s)$, for example, where $\delta(z - z_s)$ is a Chirac's delta function, the source is then represented by a stress jump through the horizontal plane at $z = z_s$,

$$\mathbf{e}_n \cdot \mathbf{\Gamma}\,\Big|_{-}^{+} \;=\; \mathbf{f}_s. \tag{2.11}$$

2.2 Application of the Hankel transform

For a layered half-space model which consists of an arbitrary but finite number of horizontal layers, with a free surface on top and the deepest layer extending to infinite depth, it is convenient to use the cylindrical coordinate system $\mathbf{x} = (z, r, \theta)$ in which z is the symmetry axis through the point source and positive downwards. In this reference system, the Bessel functions of the first kind, $J_m(x)$, are used to obtain the cylindrical surface harmonics

$$Y_k^m(r,\theta) \;=\; J_m(kr) \begin{pmatrix} \cos m\theta \\ \sin m\theta \end{pmatrix}, \tag{2.12}$$

or, using an equivalent notation

$$Y_k^m(r,\theta) \;=\; J_{|m|}(kr)e^{im\theta}, \tag{2.13}$$

for ($0 \leq k < \infty$, $m \in \mathbb{Z}$). These are used to obtain the surface vector harmonics, given by

$$\mathbf{Z}_k^m(r,\theta) \;=\; \mathbf{e}_z Y_k^m(r,\theta), \tag{2.14}$$

$$\mathbf{R}_k^m(r,\theta) \;=\; \left(\frac{\mathbf{e}_r}{k}\frac{\partial}{\partial r} + \frac{\mathbf{e}_\theta}{kr}\frac{\partial}{\partial \theta}\right) Y_k^m(r,\theta), \tag{2.15}$$

$$\mathbf{T}_k^m(r,\theta) \;=\; \left(\frac{\mathbf{e}_r}{kr}\frac{\partial}{\partial \theta} - \frac{\mathbf{e}_\theta}{k}\frac{\partial}{\partial r}\right) Y_k^m(r,\theta), \tag{2.16}$$

Consider the Hankel transforms (c.f. Bracewell, 1965, pp. 244)

$$\begin{aligned} \mathbf{u}(z,r,\theta) \;&=\; \sum_m \int_0^\infty [U_m(z,k)\,\mathbf{Z}_k^m(r,\theta) \\ &\quad + V_m(z,k)\,\mathbf{R}_k^m(r,\theta) + W_m(z,k)\,\mathbf{T}_k^m(r,\theta)]\,kdk, \end{aligned} \tag{2.17}$$

$$\begin{aligned} \mathbf{e}_z \cdot \mathbf{\Gamma}(z,r,\theta) \;&=\; \sum_m \int_0^\infty [E_m(z,k)\,\mathbf{Z}_k^m(r,\theta) \\ &\quad + F_m(z,k)\,\mathbf{R}_k^m(r,\theta) + G_m(z,k)\,\mathbf{T}_k^m(r,\theta)]\,kdk, \end{aligned} \tag{2.18}$$

where U_m, V_m, …are the wavenumber spectra of the displacement and stress field. Application of the Hankel transform to Eq. 2.7 yields two systems of ordinary differential equations which are decoupled from each other and govern the depth-dependent coefficient sets (U_m, E_m, V_m, F_m) and (W_m, G_m), respectively. A detailed obtention of these two systems of ordinary differential equations can be found in the Appendix A.

The first system is called the poloidal mode and corresponds to the P-SV wave field in seismology. In matrix notation it is written as

$$\frac{d}{dz}\mathbf{y}_m = \mathbf{A}\,\mathbf{y}_m, \tag{2.19}$$

where

$$\mathbf{y}_m \;=\; (U_m, E_m, V_m, F_m)^t \tag{2.20}$$

expresses a generalized 4-dimensional displacement vector in the wavenumber domain, and

$$\mathbf{A} = \begin{pmatrix} 0 & \dfrac{1}{\lambda+2\mu} & \dfrac{\lambda k}{\lambda+2\mu} & 0 \\ 0 & 0 & 0 & k \\ -k & 0 & 0 & \dfrac{1}{\mu} \\ 0 & -\dfrac{\lambda k}{\lambda+2\mu} & \dfrac{4k^2\mu(\lambda+\mu)}{\lambda+2\mu} & 0 \end{pmatrix} \tag{2.21}$$

is the coefficient matrix.

The second system is a 2-dimensional toroidal mode corresponding to the SH wave field in seismology,

$$\frac{d}{dz}\mathbf{x}_m = \mathbf{B}\,\mathbf{x}_m, \tag{2.22}$$

where

$$\mathbf{x}_m = (W_m, G_m)^t, \tag{2.23}$$

and

$$\mathbf{B} = \begin{pmatrix} 0 & \dfrac{1}{\mu} \\ \mu k^2 & 0 \end{pmatrix}. \tag{2.24}$$

The functions L_m, M_m and N_m are the wavenumber spectra of the the body force $\mathbf{f}$.

The interface conditions, Eqs. 2.8 and 2.9, are then expressed by the continuity conditions of the generalized displacement vectors $\mathbf{y}_m$ and $\mathbf{x}_m$,

$$\mathbf{y}_m\,\big|_-^+ = \mathbf{0}, \tag{2.25}$$

$$\mathbf{x}_m\,\big|_-^+ = \mathbf{0}, \tag{2.26}$$

the free surface conditions, Eq. 2.10, by

$$\mathbf{y}_m = (U_m, 0, V_m, 0)^T, \tag{2.27}$$

$$\mathbf{x}_m = (W_m, 0)^T, \tag{2.28}$$

and the source conditions, Eq. 2.11, in general by

$$\mathbf{y}_m\,\big|_-^+ = \Delta\mathbf{y}_m(z_s), \tag{2.29}$$

$$\mathbf{x}_m\,\big|_-^+ = \Delta\mathbf{x}_m(z_s), \tag{2.30}$$

where $\Delta\mathbf{y}_m(z_s)$ and $\Delta\mathbf{x}_m(z_s)$ are the poloidal and toroidal source functions, respectively. These are obtained by integration of the body force $\mathbf{f}$, and depend therefore of the function used to describe it. For a single force and a point dislocation, Table 2.1 shows the Hankel transformed source functions.

Y_k^m	$J_m(kr)\cos m\theta$			$J_m(kr)\sin m\theta$	
m	0	1	2	1	2
ΔU_m	$-\frac{M_{zz}}{2\pi(\lambda+2\mu)}$	0	0	0	0
ΔE_m	$\frac{f_z}{2\pi}$	0	0	0	0
ΔV_m	0	$-\frac{M_{xz}}{2\pi\mu}$	0	$-\frac{M_{yz}}{2\pi\mu}$	0
ΔF_m	$\frac{(2\mu+3\lambda)M_{zz}}{2\pi(\lambda+2\mu)}k$	$\frac{f_x}{2\pi}$	$\frac{M_{xx}-M_{yy}}{4\pi}k$	$\frac{f_y}{2\pi}$	$\frac{M_{xy}}{2\pi}k$
ΔW_m	0	$\frac{M_{yz}}{2\pi\mu}$	0	$-\frac{M_{xz}}{2\pi\mu}$	0
ΔG_m	0	$-\frac{f_y}{2\pi}$	$-\frac{M_{xy}}{2\pi}k$	$\frac{f_x}{2\pi}$	$\frac{M_{xx}-M_{yy}}{4\pi}k$

Table 2.1: *Hankel transformed source functions in the cases of a point single force (f_x, f_y, f_z) and a point dislocation with the moment tensor components ($M_{xx}, M_{xy} = M_{yx}, M_{xz} = M_{zx}, M_{yy}, M_{yz} = M_{zy}, M_{zz}$) with $M_{xx} + M_{yy} + M_{zz} = 0$.*

2.3 Thomson-Haskell propagator algorithm

Solutions of Eqs. 2.19 and 2.22 can be obtained in the closed analytical form as follows. For the poloidal displacement, the solutions to Eq. 2.19 are given by

$$\mathbf{y}(z) \;=\; e^{\mathbf{A}z}. \tag{2.31}$$

By the eigen decomposition theorem, the matrix exponent can be written as

$$e^{\mathbf{A}z} = \mathbf{L}_p(z)\mathbf{E}_p(z)\mathbf{L}_p^{-1}(z), \tag{2.32}$$

$\mathbf{E}_p(z)$ is the (4×4) diagonal eigenvalue matrix

$$\mathbf{E}_p(z) \;=\; dia\left(e^{\lambda_i z}\right) = dia\left(e^{kz}, e^{-kz}, e^{kz}, e^{-kz}\right), \tag{2.33}$$

with λ_i being the eigenvalues of the matrix $\mathbf{A}$. $\mathbf{L}_p(z)$ is the (4×4) poloidal layer matrix, whose 4 columns consist of the 4 eigenvectors of the coefficient matrix $\mathbf{A}$, $\mathbf{l}_p^i$, and $\mathbf{L}_p^{-1}(z)$ is the inverse of the layer matrix $\mathbf{L}_p(z)$.

Since $+k$ and $-k$ are both second order eigenvalues, their corresponding eigenvectors should be linear functions of z instead of constant, that is

$$\mathbf{l}_p^i = \mathbf{a} + \mathbf{b}z \tag{2.34}$$

with both $\mathbf{a}$ and $\mathbf{b}$ being constant vectors. Hence, the eigenvalue problem is equivalent to the (8×8) matrix system

$$\begin{pmatrix} \mathbf{A} \mp k\mathbf{I} & -\mathbf{A} \\ \mathbf{0} & \mathbf{A} \mp k\mathbf{I} \end{pmatrix} \begin{pmatrix} \mathbf{a} \\ \mathbf{b} \end{pmatrix} = \mathbf{0} \tag{2.35}$$

After calculations, we find that the poloidal layer matrix is given by

$$\mathbf{L}_p(z) = \begin{pmatrix} 1 & 1 & 1+\frac{\lambda+\mu}{\mu}(1-kz) & 1+\frac{\lambda+\mu}{\mu}(1+kz) \\ 2\mu k & -2\mu k & 2(\lambda+\mu)(1-kz)k & -2(\lambda+\mu)(1+kz)k \\ 1 & -1 & -1-\frac{\lambda+\mu}{\mu}kz & 1-\frac{\lambda+\mu}{\mu}kz \\ 2\mu k & 2\mu k & -2(\lambda+\mu)k^2 z & 2(\lambda+\mu)k^2 z \end{pmatrix}, \tag{2.36}$$

The individual solutions to Eq. 2.19 are then

$$\mathbf{y}_i(z) = \mathbf{l}_p^i \cdot e^{\lambda_i z}. \tag{2.37}$$

and the general solution is a linear combination of the individual solutions

$$\mathbf{y}(z) = \sum_{i=1}^{4} c_{p_i} \cdot \mathbf{l}_p^i \cdot e^{\lambda_i z} = \mathbf{L}_p(z)\,\mathbf{E}_p(z)\,\mathbf{c}_p, \tag{2.38}$$

where $\mathbf{c}_p$ is an arbitrary constant vector,

$$\mathbf{c}_p = (A_+, A_-, B_+, B_-)^t, \tag{2.39}$$

Note that the displacement in the form of Eqs. 2.38 and 2.39 shows again an analogy to seismology. The terms with constants $A_\pm$ and $B_\pm$ correspond to amplitudes of the up- and down-going P and SV waves, respectively. Their depth-dependence is characterized by the terms $e^{\pm kz}$ and $(kz)e^{\pm kz}$, respectively.

For a homogeneous layer of thickness h, we find from Eq 2.38 that

$$\mathbf{y}(0) = \mathbf{L}_p(0)\,\mathbf{E}_p(0)\,\mathbf{c}_p = \mathbf{L}_p(0)\mathbf{c}_p, \tag{2.40}$$

hence, we can relate the displacement vector at the upper and lower boundaries of the layer by

$$\mathbf{y}(h) = \mathbf{H}_p(h)\,\mathbf{y}(0), \tag{2.41}$$

where

$$\mathbf{H}_p(h) = \mathbf{L}_p(h)\,\mathbf{E}_p(h)\,\mathbf{L}_p^{-1}(0). \tag{2.42}$$

The matrix $\mathbf{H}_p$ is known as the Thomson-Haskell propagator, and relates the displacement vector from depth to depth. Using this approach, the boundary-value problem is converted to an algebraic problem. The boundary conditions are supplied by the free surface conditions and the conditions in infinity. On one side, we can choose any two independent starting values for the displacement vector, both of which satisfy the free surface conditions ($E_m = F_m = 0$), and propagate it downwards until the source plane. Similarly, the same procedure can be done from the deepest interface upwards to the source plane. The only difference is that the start values here should satisfy the conditions for infinity, that is, $A_+ = B_+ = 0$, because there are no upgoing waves from infinity. The displacement vectors determined this way are the fundamental bases of solutions of the present boundary-value problem. The desired displacement is a linear superposition of them. The weights will be determined by the source conditions.

The situation for the toroidal mode is similar but easier than the poloidal mode shown above because the dimension is reduced from 4 to 2. The general solution to Eq. 2.22 is

$$\mathbf{x}(z) \;=\; \mathbf{L}_t(z)\,\mathbf{E}_t(z)\,\mathbf{c}_t, \tag{2.43}$$

where the (2×2) toroidal layer matrix, whose 2 columns consist of the 2 eigenvectors of the coefficient matrix $\mathbf{B}$, $\mathbf{l}_t^i$, is given by

$$\mathbf{L}_t(z) \;=\; \begin{pmatrix} 1 & 1 \\ \mu k & -\mu k \end{pmatrix}, \tag{2.44}$$

$\mathbf{E}_t(z)$ is the (2×2) diagonal eigenvalue matrix

$$\mathbf{E}_t(z) \;=\; dia\left(e^{kz}, e^{-kz}\right), \tag{2.45}$$

and $\mathbf{c}_t$ is the constant vector

$$\mathbf{c}_t \;=\; (C_+, C_-)^t\,. \tag{2.46}$$

Similarly, for a homogeneous layer of thickness h, we can also derive the relationship

$$\mathbf{x}(h) \;=\; \mathbf{H}_t(h)\,\mathbf{x}(0), \tag{2.47}$$

where

$$\mathbf{H}_t(h) \;=\; \mathbf{L}_t(h)\,\mathbf{E}_t(h)\,\mathbf{L}_t^{-1}(0). \tag{2.48}$$

2.4 The improved propagator algorithm

Calculations with the algorithm described above are not stable for the poloidal mode. It might appear that the problem is caused by operations between the large e^{kz} terms and the small e^{-kz} term. However, the results for the toroidal mode are stable, so this cannot be the reason for the instability of the poloidal mode. In reality, the problem is caused by operations between the two increasing vectors. For example, when a displacement vector is being propagated from the surface downwards (in the positive z direction), the terms A_+e^{kz} and $B_+(kz)e^{kz}$ represent two increasing waves and the terms A_-e^{-kz} and $B_-(kz)e^{-kz}$ two amplitude-decreasing waves. It is obvious that through operations with the Thomson-Haskell propagator the two amplitude-increasing waves included in the displacement vector become more significant than the two decreasing waves. In the extreme, i.e., when $kh >> 1$, the latter can even lose their numerical presence. Additionally, when the product between the wavenumber and the layer thickness is large, also the less strongly increasing A_+e^{kz} wave, should have lost its significance to a certain extent due to the operation with the more strongly increasing $B_+(kz)e^{kz}$ wave. If such a process is repeated by a number of thick layers, all displacement vectors may finally be dominated by the single $B_+(kz)e^{kz}$ wave, regardless what start values of them were chosen. Consequently, the fundamental displacement vector bases computed this way will loss their independence and the numerical instability arises when they are superposed to satisfy the source conditions.

From the physical point of view, the two decreasing e^{-kz} and $(kz)e^{-kz}$ waves describe the reflection from the top of a layer. When the layer thickness, measured by the wavelength $1/k$, is large enough, the evanescent reflection effect can not be observed at the bottom of the layer. Thus, the vanishing of the decreasing waves is of physical nature. In contrast, however, the vanishing of one increasing wave due to operations with the other increasing wave is purely of numerical nature because both include independent and complementary information about the radiation characteristic of the source. Therefore, to solve the loss-of-precision problem, any direct numerical operations between the two increasing waves should be avoided. For this purpose, Wang (1999b) proposed an orthonormalisation extension to the propagator algorithm. As has been stated, there are two fundamental displacement vector bases to be determined for the poloidal mode. In the improved propagator algorithm, the two vector bases are not computed separately but simultaneously. At each interface, they are linearly transformed, or orthonormalised in a wide sense, to the other two vector bases so that each of them includes only one increasing wave for the next homogeneous layer. Then, the new vector bases can be propagated to the next interface without any numerical operations between the two increasing waves and the loss-of-precision problem is fully solved.

The orthonormalised propagator algorithm has been successfully applied to the computation of synthetic seismograms (Wang, 1999b) and quasi-static deformations in poro-plastic media (Wang and Kümpel, 2003). The same computation strategy is also adopted for the calculations presented in the following Chapters.

2.5 Convergence problems of the numerical Hankel transform

In the software used for the results presented here, equidistant wavenumber sampling is used in the numerical Hankel transform (wavenumber integrations in Eqs. 2.17 and 2.18). The sampling interval Δk can be chosen between 1-10% of the Nyquist wavenumber $2\pi/r_{max}$, where r_{max} is the maximum horizontal distance from the test points to the source. A practical problem here is the cut-off value of the wavenumber k, which depends upon how fast the integrands in Eqs. 2.17 and 2.18 converge to zero. In case that the observation points are located at a different depth than the source, the integrands decrease with wavenumber k approximately by e^{-kd} or ke^{-kd}, where d is the depth difference between the observation points and the source. Then, the cut-off wavenumber can be determined so that all integrands become insignificant, for example, several orders smaller than their maxima. However, if the source and the observation points are located at the same depth, the integrands at large wavenumbers either converge to non-zero constants or linearly increase with the wavenumber. The difficulty is caused by the idealized point source and can be solved using a similar technique as the one used by Farrell (1972) for calculating the deformation of a spherical earth induced by surface loading. Using this technique, the asymptotic terms are expressed in the analytical form and removed from the numerical wavenumber integrations as follows

$$\begin{aligned}\int_0^\infty U(k)J_2(kr)kdk &= \int_0^\infty \Delta U(k)J_2(kr)kdk + U_\infty \int_0^\infty J_2(kr)kdk \\ &= \int_0^\infty \Delta U(k)J_2(kr)kdk + \frac{2}{r^2}U_\infty, \end{aligned} \qquad (2.49)$$

where where U_∞ is the limit value of $U(k)$ for $k \to \infty$ and $\Delta U(k)$ is the difference $U(k) - U_\infty$.

In addition, the δ point source function is replaced by an extended disk source with a characteristic radius r_o which is much smaller than the distance to the observation points. For example, if an extended source with a normal distribution is used, the only difference to the point source is an additional factor $e^{-k^2r_o^2}$ to be multiplied to the wavenumber integrands. In practice, this factor can effectively accelerate the convergence of the numerical integrations. Therefore

$$\int_0^\infty U(k)J_2(kr)kdk \approx \int_0^{k_\infty} \Delta U(k)J_2(kr)e^{-k^2r_o^2}kdk + \frac{2}{r^2}U_\infty, \qquad (2.50)$$

where k_∞ is the cut-off wavenumber, and $r_o << r$ is the characteristic spatial extension of the physical point source. Presently, k_∞ is determined through a rough sampling so that the integrands decrease by 3–4 orders for $k > k_\infty$ in comparison with their maxima, and r_o is about 1% of the source-observation distance r.

2.6 A consistent approach for including the gravitational effect

The extension of the earlier elastic dislocation theory with the gravitational effect was first made by Rundle (1980b) based on the generally governing equations for infinitesimal static deformation in a self-gravitating, hydrostatically prestressed Earth (Love, 1911),

$$\nabla \cdot \mathbf{\Gamma} + \rho\nabla(\psi + \mathbf{u}\cdot\mathbf{g}) - \mathbf{g}\nabla\cdot(\rho\mathbf{u}) = \mathbf{0}, \qquad (2.51)$$

$$\nabla^2\psi - 4\pi G\nabla\cdot(\rho\mathbf{u}) = 0, \qquad (2.52)$$

where $\mathbf{\Gamma}$ is the Lagrangian incremental stress tensor, $\mathbf{u}$ is the displacement vector, ψ is the Eulerian incremental potential, $\mathbf{g}$ is the acceleration due to gravity, G is the gravitational constant, and ρ is the density.

In order to apply Eqs. 2.51 and 2.52 to a simplified plane-Earth model, Rundle approximates the Earth's gravity $\mathbf{g}$ by its surface value and treats it as a constant external body force. Since the self-gravitating term, $\rho\nabla\psi$ in Eq. 2.51, is negligible for co- and post-seismic deformation, it is in general enough to consider the so-called reduced problem, in which the deformation equations are decoupled from the potential field equation (Rundle, 1982). To construct the Haskell propagator for the reduced problem, four Hankel-transformed fundamental displacement solutions of the poloidal (P-SV) type and two of the toroidal (SH) type are needed, as in the elastic, non-gravitational case. Since the SH solutions include only horizontal movements without volume changes, they are not affected by the gravity field. The Hankel-transformed P-SV solutions with the gravity effect have been given in the form

$$\begin{bmatrix} U_z(k,z) \\ U_r(k,z) \end{bmatrix} = \begin{bmatrix} p^{\pm}_{1,2}(k) \\ 1 \end{bmatrix} exp\left[\pm m_{1,2}(k)z\right], \tag{2.53}$$

with

$$p^{\pm}_{1,2} = \frac{(\lambda+2\mu)k^2 - \mu\, m^2_{1,2}}{k\left[\rho g \pm (\lambda+\mu)m_{1,2}\right]}, \tag{2.54}$$

where k is the horizontal wavenumber (parameter of the Hankel transform), $\pm m_{1,2}$ are the four vertical wavenumbers of the deformation field,

$$\pm m_1 = \pm\sqrt{k^2 + kk_g}, \tag{2.55}$$

$$\pm m_2 = \pm\sqrt{k^2 - kk_g}, \tag{2.56}$$

and

$$k_g = \frac{\rho g}{\sqrt{\mu(\lambda+2\mu)}}. \tag{2.57}$$

For $k > k_g$, the elastic-gravitational Haskell propagator can be constructed in analogy to the purely elastic one (see Appendix). Particularly for $k >> k_g$, the elastic-gravitational solutions converge to the purely elastic ones, implying that the gravity can only affect deformation over long wavelengths.

However, a problem occurs for $k \leq k_g$. In this case, the boundary value problem has no solution at all because only one of the four fundamental solutions given by Eq. 2.53 is regular at infinite depth, but two are in general required. It should be mentioned that the regularity at infinite depth is necessary from both the physical and the mathematical points of view. If any non-regular solution is used instead of the missing regular one, two consequences are expected: (1) A small local perturbation may cause a global reaction of the half-space, and (2) the reaction cannot be uniquely determined because there are two non-regular solutions for choice. The parameter k_g therefore represents a critical wavenumber of the model. As shown by Wang (2005a), this regularity problem was ignored in many previous studies. In fact, the solution given in Eq. 2.53 that is valid for $k > k_g$ was implicitly extrapolated to the invalid wavenumber region $0 \leq k \leq k_g$. Consequently, kernel functions (i.e. the Hankel-transformed response functions) obtained became complex even in the static elastic case and exhibit singularities near the critical wavenumber.

The regularity problem can be explained by the physically inconsistent assumptions made for the half-space model. In fact, any compressible medium should become more compact under hydrostatic pressure. Therefore, when including the constant gravity, a self-consistent half-space model should either be incompressible, or have an increasing density with depth. Otherwise, the model is not in a hydrostatical equilibrium state and is therefore unstable. The existence of the critical wavenumber implies that an unpredictable deformation at infinite depth can be induced by a small near-surface perturbation, if the wavelength of the perturbation is large enough – a certainly non-physical consequence.

Another problem is the long-term instability occurring when the shear modulus of a compressible layer of the model relaxes to a very small value. In contrast to the regularity problem for the low wavenumber range, the instability may appear at any wavenumber. However, the physical causes for these two different problems are the same, that is as $\mu \rightarrow 0$, the finite compressible layer becomes practically an infinite medium considering the vanishing gravitational wavelength of this layer ($1/k_g \rightarrow 0$).

Wang (2005b) has shown that these two numerical problems can be overcome by using the Adams-Williamson condition (Longman, 1963). This condition requires the density gradient resulting from the initial hydrostatic equilibration. It is given by

$$\frac{d\rho}{dz} = \frac{\rho^2 g}{\kappa}, \tag{2.58}$$

where the parameter $\kappa = \lambda + 2\mu/3$ is the bulk modulus which is assumed to be constant during the viscoelastic relaxation (see below). In fact, the Adams-Williamson condition is well satisfied by most realistic Earth models, except for an asthenospheric structure.

When including this density gradient, the equation for the reduced problem reads

$$\nabla \cdot \mathbf{\Gamma} + \rho g \nabla u_z - \left(\rho \nabla \cdot \mathbf{u} + \frac{\rho^2 g}{\kappa} u_z \right) g \mathbf{e}_z \; = \; \mathbf{0}, \tag{2.59}$$

where $\mathbf{g} = g\mathbf{e}_z$ has been used.

In the upper and lower Earth's crust, the density deviations needed to satisfy the Adams-Williamson condition are within a few percent. Therefore, after the density gradient is explicitly considered, the remaining density parameter ρ in Eq. 2.59 can still be treated as a constant value. Using this approximation, we find that the four vertical wavenumbers given by Eqs. 2.55 and 2.56 are modified to

$$\pm m_1 \;=\; \pm\sqrt{k^2 + \frac{2}{3}\left(\tilde{k}_g^2 + \tilde{k}_g \sqrt{\tilde{k}_g^2 - k^2} \right)}, \tag{2.60}$$

$$\pm m_2 \;=\; \pm\sqrt{k^2 + \frac{2}{3}\left(\tilde{k}_g^2 - \tilde{k}_g \sqrt{\tilde{k}_g^2 - k^2} \right)}, \tag{2.61}$$

where

$$\tilde{k}_g \;=\; \frac{\rho g}{\sqrt{\frac{4}{3}\kappa(\lambda + 2\mu)}}. \tag{2.62}$$

The coefficients given by Eq. 2.54 are still valid.

Note that the real part of the modified eigenvalues $\pm m_{1,2}$ never vanishes for $k > 0$. Thus, no critical wavenumber exists even for $\mu \rightarrow 0$. The regularity problem for the low wavenumber range and the numerical instability for the long-term relaxation are therefore avoided by this regularization approach.

2.7 Implementation of the rheology

According to viscoelasticity theory, post-seismic deformation transients are controlled by (1) the source time function, usually a Heaviside step function, and (2) the relaxation of the shear stress in the inelastic media with time. To avoid the complicated convolution in the time domain, all approaches use the correspondence principle (cf. Christensen, 1971), which states that a linear viscoelastic boundary-value problem can be solved by adopting the associated elastic solutions, in which the elastic moduli are replaced by the Laplace or Fourier transformed complex moduli. Then the time-domain solutions are obtained via the inverse Laplace transform. Since the viscoelastic response spectra are usually complicated functions of the Laplace time-conjugate parameter (frequency), results in the closed analytical form are only possible for few particularly simple models, for example the homogeneous viscoelastic half-space without gravity effects. For more complicated models, numerical methods must be used, which in general require a dense sampling of the response spectra that are obtained by the Haskell propagator algorithm and the Hankel transform. The numerical tool used for the results presented in the following Chapters is based on the Riemann-Mellin contour integral in combination with the FFT technique, a straightforward and full-spectrum method for ensuring numerical stability in calculating post-seismic transients. Because of the complicated non-linear relationship between geophysical observables and subsurface structure, a direct inversion for rheological parameters is in general difficult. Since the software provides a forward modeling tool, usually a large set of models must be run to select the best-fitting one. Therefore, the efficiency of the software and the stability of its numerical results are crucial. This is achieved by the effective techniques (orthonormalized Haskell propagator, analytical asymptotes, filter techniques, etc.) used to solve the stability and convergence problems when computing the Green functions (Wang and Kümpel, 2003; Wang, 1999b; Wang et al., 2003). These techniques lead to small, fast and very accurate programs.

In most seismic reference Earth models, the quality factor of the bulk modulus is at least one order higher than that of the shear modulus. On that account, only the shear modulus will be considered to be viscoelastic while the bulk modulus remains elastic. Viscoelasticity is described by the SLS rheology defined by three parameters: the unrelaxed shear modulus μ_o, the viscosity η and the parameter α which is the ratio of the fully relaxed modulus to the unrelaxed modulus (Fig. 2.2). In the frequency domain, the complex shear modulus is then given by

$$\mu(i\omega) \;=\; \mu_o \frac{\alpha(1-\alpha) + i\omega\eta/\mu_o}{(1-\alpha) + i\omega\eta/\mu_o}, \tag{2.63}$$

where ω is the angular frequency, and $i \;=\; \sqrt{-1}$. Note that the complex shear modulus defined here differs from the Fourier transform of the shear relaxation function by the factor $i\omega$ (see e.g., Christensen, 1971).

Obviously, the SLS rheology becomes identical to the Maxwell rheology when the relaxation ratio $\alpha \;\rightarrow\; 0$. Another special case is $\alpha \;\rightarrow\; 1$ for the perfect elasticity. For the latter case, the viscosity parameter in Eq. 2.63 is meaningless.

The complex Lamé constant $\lambda(i\omega)$ can be derived from the complex shear modulus

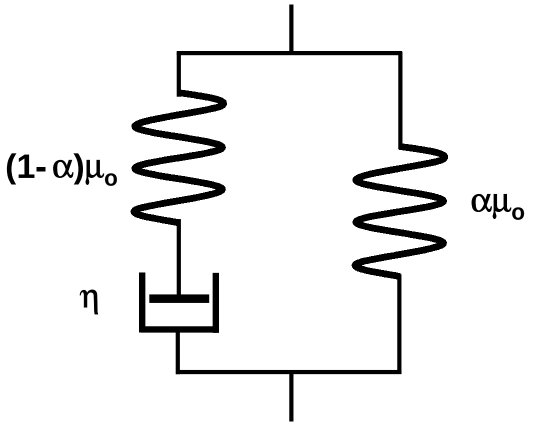

Figure 2.2: *Model of the SLS rheology.* μ_o *is the unrelaxed modulus,* η *is the viscosity, and* $0 \leq \alpha \leq 1$ *is the relaxation ratio. Note the two special cases,* $\alpha = 1$ *and* $\alpha = 0$*, representing perfect elasticity and the Maxwell rheology, respectively.*

$\mu(i\omega)$ by assuming a constant bulk modulus:

$$\lambda(i\omega) \;=\; \lambda_o + \frac{2}{3}\left[\mu_o - \mu(i\omega)\right], \tag{2.64}$$

where λ_o represents the unrelaxed Lamé constant.

2.8 A practical anti-aliasing technique

Once the boundary-value problem has been solved in the frequency domain using the correspondence principle, the time-dependent Green functions can be obtained by the inverse Fourier transform. It is known that aliasing problems may appear when using the discrete FFT algorithm.

If the sampling interval of the frequency, which is antiproportional to the time window used, is not high enough, signals beyond the time window will appear at the wrong frequency. These alias signals may result in a wrong estimation of the co-seismic deformation. To solve the problem, we adopt the anti-aliasing technique that has been used in computing synthetic seismograms (Kind and Seidl, 1982). Instead of the Fourier spectrum, for example $X(i\omega)$, the Laplace spectrum $X(\sigma + i\omega)$, where σ is a small positive constant, will be computed. The inversion for its time-domain function $x(t)$ is then given by

$$\begin{aligned} x(t) \;&=\; e^{\sigma t}\, F^{-1}\left[X(\sigma + i\omega)\right] \\ &=\; e^{\sigma t}\, \frac{1}{2\pi} \int_{-\infty}^{+\infty} X(\sigma + i\omega) e^{i\omega t} d\omega. \end{aligned} \tag{2.65}$$

In fact, Eq. 2.65 can be directly derived from the well-known Riemann-Mellin inversion formula.

Note that $X(\sigma + i\omega)$ is the Fourier spectrum of the function $e^{-\sigma t}x(t)$, i.e. $x(t)$ filtered by the window function $e^{-\sigma t}$. Using Eq. 2.65, the amplitude of the alias signals appearing at the origin time are reduced by the factor $e^{-\sigma T}$, where T is the length of the time window used. We therefore define $\beta = e^{-\sigma T}$ and call it the alias-suppression factor. The smaller the β factor chosen, the more effectively are the alias signals suppressed. On the other hand, a too small β value will enhance at the same time the numerical errors of the long-term relaxation signals. In most practical cases, to choose $0.1 \leq \beta \leq 0.5$ should be appropriate if the time window used is large enough to cover the main relaxation process.

Another aliasing problem are numerical oscillations due to the limited cut-off frequency used, which is antiproportional to the sampling interval. In general, the viscoelastic response to a Heaviside dislocation source is characterized by three stages: (1) the instantaneous elastic response, (2) the transient viscoelastic relaxation process, and (3) the steady end state. An approximation of such time behavior using a single relaxation time can be expressed in the form

$$x(t) \;=\; \left[x_p + (x_i - x_p)e^{-t/\tau}\right] H(t), \tag{2.66}$$

where x_i is the instantaneous co-seismic change, x_p is the permanent change, τ is the relaxation time, and $H(t)$ is the Heaviside function.

The Laplace transform of the function $x(t)$ is

$$X(\sigma + i\omega) \;=\; \frac{x_p}{\sigma + i\omega} + \frac{x_i - x_p}{\sigma + i\omega + 1/\tau}. \tag{2.67}$$

For a multi-layered model, there may be several relaxation times or even a continuous relaxation spectrum. In this case, the parameter τ represents the main relaxation time of the model. Because the spectrum given by Eq. 2.67 converges slowly to zero, numerical oscillations related to the cut-off frequency may appear when using the discrete FFT. To overcome the problem, the co-seismic and steady-state solutions, x_i and x_p, respectively, are also computed. Then, Eq. 2.67 is used for the first-order prediction and subtracted from the computed spectra. The numerical inverse FFT is then only applied to the residual spectra, and the end result is obtained by adding Eq. 2.66 to the inverse FFT of the residual spectra. The key point of this approach is the estimation of the main relaxation time τ, which may be different for different observables at different positions. In the present implementation, the parameter τ is estimated independently for each Green function component, following the criterion that the residual takes a value as small as possible at the cut-off frequency.

Numerical tests have shown that the above two techniques are very efficient. The two aliasing problems have been satisfactorily solved. In most cases, a stable FFT result can be obtained even if the time window used is not large enough and/or the time sampling rate is not high enough.

2.9 Computation procedures

The described methodology for calculation of deformation in a layered viscoelastic gravitational Earth model has been programmed into a code consists of two programs. The first program, PSGRN, is used to prepare the time-dependent Green's functions that describe the response of the viscoelastic-gravitational model to the 4 fundamental dislocation sources at different depths with a Heaviside time history. The second program, PSCMP, is used to compute the transient deformation, as well as changes in the geoid and gravity field induced by finite fault planes of an earthquake via linear superposition. Usually, PSGRN is considerably more time-consuming than PSCMP.

However, once the Green's functions have been calculated, they can be repeatedly used for different earthquakes, as long as the Earth model remains unchanged. This is the reason why the computation is divided into these two steps. The flowcharts of major subroutines of the two programs are shown in Fig. 2.3 and Fig. 2.4, respectively.

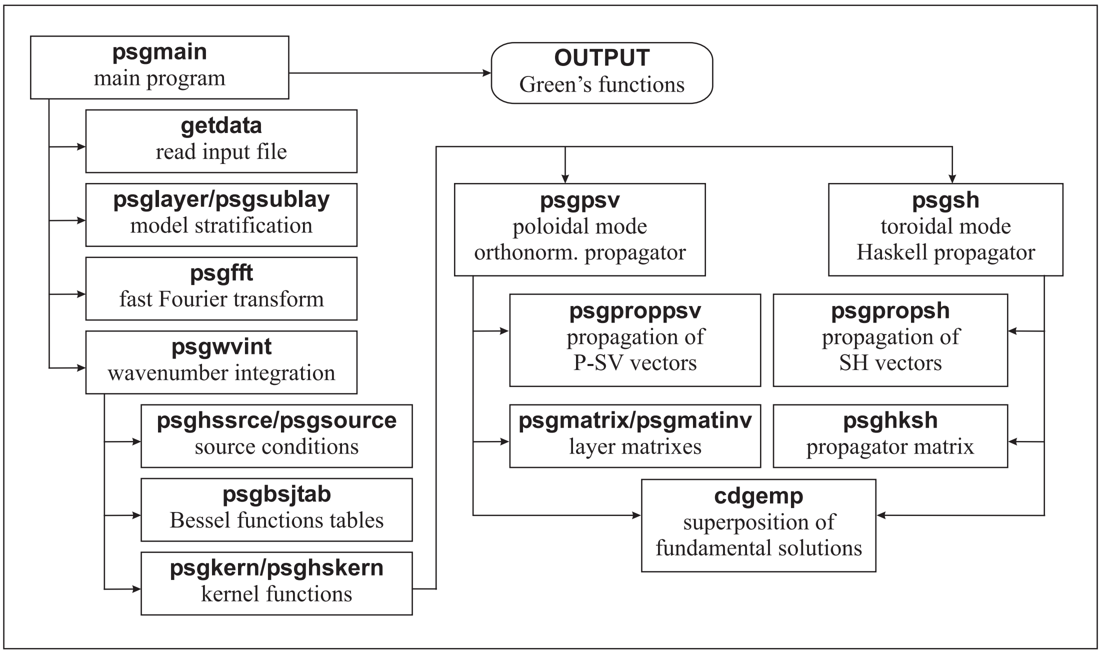
psgmain
main program
OUTPUT
Green's functions
getdata
read input file
psglayer/psgsublay
model stratification
psgfft
fast Fourier transform
psgwvint
wavenumber integration
psghssrce/psgsource
source conditions
psgbsjtab
Bessel functions tables
psgkern/psghskern
kernel functions
psgpsv
poloidal mode
orthonorm. propagator
psgsh
toroidal mode
Haskell propagator
psgproppsv
propagation of
P-SV vectors
psgpropsh
propagation of
SH vectors
psgmatrix/psgmatinv
layer matrixes
psghksh
propagator matrix
cdgemp
superposition of
fundamental solutions

Figure 2.3: *The flowchart of major subroutines of the program* **PSGRN**.

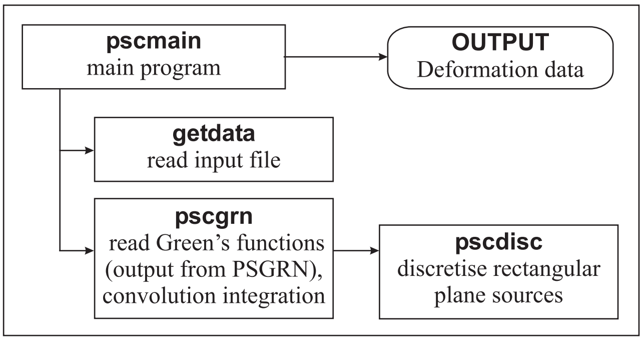
pscmain
main program
OUTPUT
Deformation data
getdata
read input file
pscgrn
read Green's functions
(output from PSGRN),
convolution integration
pscdisc
discretise rectangular
plane sources

Figure 2.4: *The flowchart of major subroutines of the program* **PSCMP**.

The output from PSGRN are Green's functions covering 13 observables (3 displacement components, 6 stress components, 2 tilt components, and 2 geopotential components, i.e. the gravity and geoid changes) induced by the 4 different dislocation sources (strike-slip, dip-slip, CLVD and inflation). For a fixed uniform observation depth, the observables depend in general not only on the source depth and the observation distance but also on the observation azimuth angle θ. However, since the CLVD and inflation sources are axisymmetric, the associated observables are reduced by their tangential components. The azimuthal dependence for the other two source types can be expressed by a simple azimuthal factor, that is, $(\sin 2\theta,\ \cos 2\theta)$ for the strike-slip source and $(\sin\theta,\ \cos\theta)$ for the dip-slip source. Whether the cosine factor

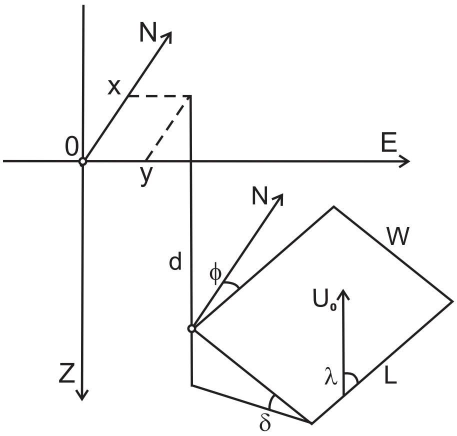

Figure 2.5: *Schematic representation of the reference system used to define the rectangular fault planes that serve as input to* **PSCMP**. *x, y and d are the North and East coordinates and the depth of the upper left corner of the rupture surface. L and W are the length and width of the rupture. Its orientation is fixed by the strike (ϕ) and dip (δ) angles, and the average displacement on the rupture surface is given by its magnitude U_0 and the rake angle (λ).*

or the sine factor is used depends on which of the observables is considered. In case of the dip-slip source ($M_{xz} \neq 0$), for example, both the vertical and radial displacements are proportional to $\cos\theta$, but the tangential displacement is proportional to $\sin\theta$. The Green's functions are thus stored without the azimuthal factor. In summary, there are 44 independent Green's functions in the discrete form. They may then be stored in a given directory to serve as a data base. The stepping of source depths and observation distances should be dense enough so that a linear interpolation can be applied later to any individual source-observation configurations. In practice, the step should be comparable with the discretisation size to be applied later to the finite source plane.

As an input of PSCMP, an earthquake is represented by an arbitrary number of rectangular fault planes with different location, area and orientation (strike, dip and rake, see Fig 2.5). PSCMP discretises these fault planes automatically to a set of point dislocations using the same spatial resolution as used for Green's functions, and carries out the convolution integration. The observation positions can be either a set of irregular stations, a 1D equidistant profile or a 2D equidistant array. In addition, users can choose either a local Cartesian coordinate system or the geographic coordinate system. In the latter case, a projection to the local Cartesian system which is needed for the internal convolution procedure will be made using the equality criterion for distance and azimuth. Output from PSCMP are all or a selected part of the 13 observables in the form of time series and/or scenarios ("snapshots").

2.10 Comparisons with previously published results

Wang (2005b) compared the gravity effects on the co- and post-seismic surface deformation computed by PSGRN/PSCMP and by the code FLTGRV published by Fernández et al. (1996a). In general, both results show that the gravity reduces the magnitude of the long-wavelength part of the vertical displacement of the crust due to the buoyancy effect at the surface and internal density discontinuities. For example, for large thrust earthquakes with a rupture area as large as 400 × 120 km^2, the results of the present code indicate that gravity can affect the co-seismic vertical movement by up to 4 percent. Over longer timescales, when ductile flow in the lower crust must be accounted for, the gravity effect on the vertical displacement can reach up to 20 percent. In comparison, the gravity effect obtained by the code FLTGRV showed a similar

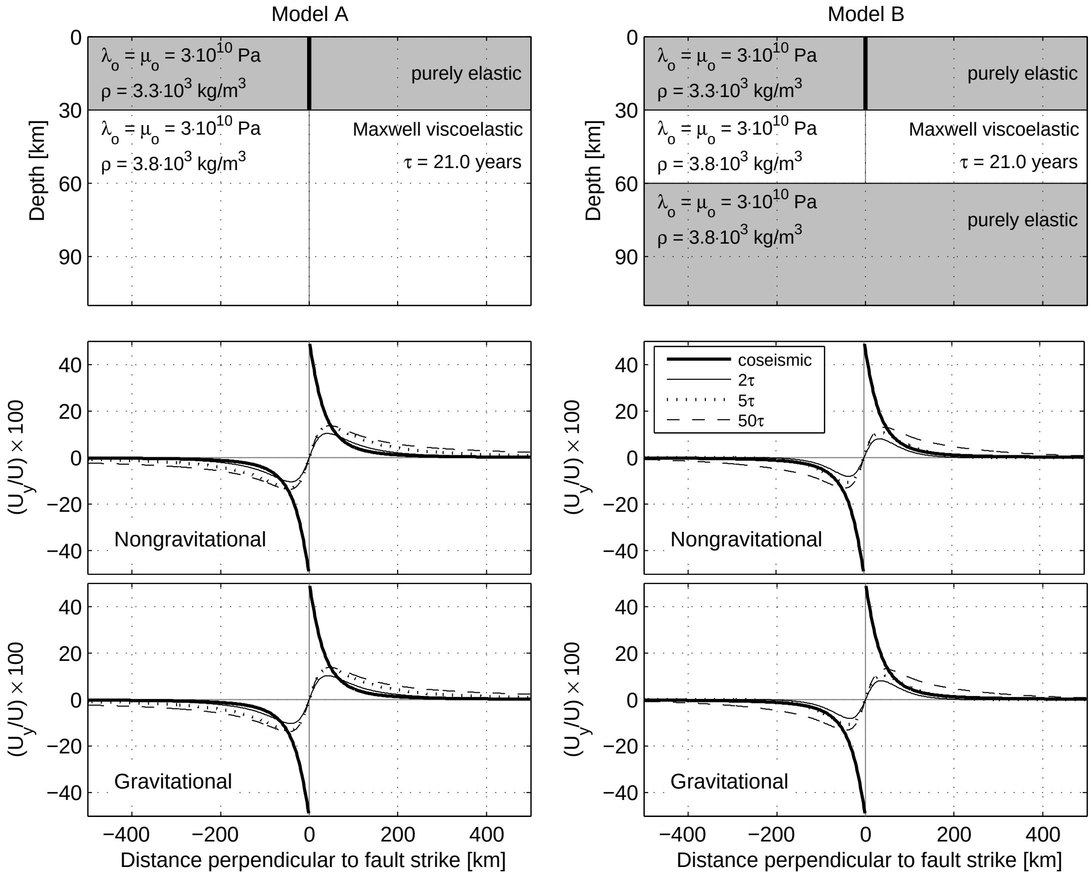

Figure 2.6: *Coseismic and additional post-seismic surface displacement calculated for two Earth models, for a profile perpendicular to the fault strike through the center of the rupture surface. The source is a vertical strike-slip dislocation. The fault is 200 km along the strike and 30 km along the dip (penetrating the entire elastic upper layer).* τ *(*$= 2\eta/\mu_o$*) is the characteristic Maxwell relaxation time.* U *represents the magnitude of slip on the fault plane and* U_y *is the displacement parallel to the fault strike. These results are comparable with Figs. 9 and 10 of Pollitz (1997).*

spatial form, but seems to include a constant offset, like a rigid-body motion of the crust, in both co- and post-seismic cases. Wang (2005b) concluded that such an offset (comparable with the peak-to-peak amplitude of the gravity effect in the thrust zone.) is unrealistic because it leads to an average surface subsidence, which is inconsistent with thrust-fault mechanisms.

Here we have recomputed deformation models presented by Pollitz (1997). Two Earth models (A and B) were used (see the upper panels of Fig. 2.6 and 2.7). Figure 2.6 shows the co- and post-seismic displacement parallel to the fault strike of a strike-slip dislocation. For both models, our results indicate no significant influence of gravity on deformation of strike-slip earthquakes, and agree with those obtained by Pollitz (1997), who used a spherical geometry (see Fig. B.2 in Appendix B).

Figure 2.7 is comparable with Figs. 3 and 6 in Pollitz (1997) (see Fig. B.1 in Appendix B), showing the vertical displacement and the displacement perpendicular to the fault strike of a buried thrust event. For Model A, we can reproduce Pollitz's results at the co-seismic and early post-seismic period, but find some differences at the late post-seismic period. In particular, for $t = 45\tau$ in the nongravitational case, our results indicate smaller subsidence at the far ends of the half-space profile than those of Pollitz (1997) for the spherical profile. Similar differences can also be seen for Model B. Additionally, our results indicate a smaller gravity effect for Model B than Pollitz's results. All these differences may be attributed to the curvature effect neglected in the present plane-Earth model, but also to the wavelength cut-off (the limited maximum degree of the spherical harmonics) used for the spherical model. It should be mentioned that such a cut-off problem does not exist in the present code, in which the analytical half-space solution (Okada, 1992) is used for the short-wavelength asymptote, so that the numerical calculation is only needed for the long-wavelength residuals due to the gravity effect and the layering of the model. In addition, the analytical propagator scheme used for plane-Earth models is in general more accurate than the numerical propagator scheme (for example the Runge-Kutta integration) used for spherical Earth models.

Model A with the same half-space geometry was also considered by Rundle (1982) (see Fig. B.3 in Appendix B). There is a good agreement between his results and ours for the vertical displacement in the nongravitational case, and a slight difference (a few percent) at $t = 45\tau$ in the gravitational case. It seems that numerical errors caused by the previous regularity problem are not so serious for earthquakes with a small to moderate magnitude, but they become non-negligible for large-scale earthquakes (for example $M_w \geq 8$) as shown by Wang (2005b).

2.11 Summary

In the present software, the numerical Green's function approach is used to calculate earthquake's viscoelastic deformations based on a layered half-space Earth model. In general, the computation task is fulfilled by two separate programs. The first program **PSGRN** prepares all fundamental Green's functions of the given multi-layered half-space, and the second program **PSCMP** carries out the convolution integrations. The advantage of this construction is the following: Once the Green's functions have been computed, they can be used repeatedly for different earthquakes as long as the earth model remains unchanged. In the program **PSGRN**, the stable and accurate results are guaranteed by the orthonormalised propagator algorithm, and the computation efficiency is achieved using the convergence accelerator technique applied to the numerical Hankel transform.

In comparison to spherical models such as those used by, for example Pollitz (1997) and Wang (1999a), an obvious disadvantage of the plane-Earth model is that it neglects the Earth's surface curvature, which may affect an earthquake's far-field deformation. However, since the source extension of a large earthquake is in general limited to about 1000 km, significant co- and post-seismic deformation may arise at distances of up to a few hundred kilometers from the earthquake's rupture edges. Therefore, the spatial extension of the deformation field, even for the largest earthquake, is smaller than about 1500 km. The maximum arch height of such a spherical area over its average plane surface is less than 25 km, or 2 percent of its horizontal extension. For such a small geometric deviation, we may expect that its influence on the deformation field

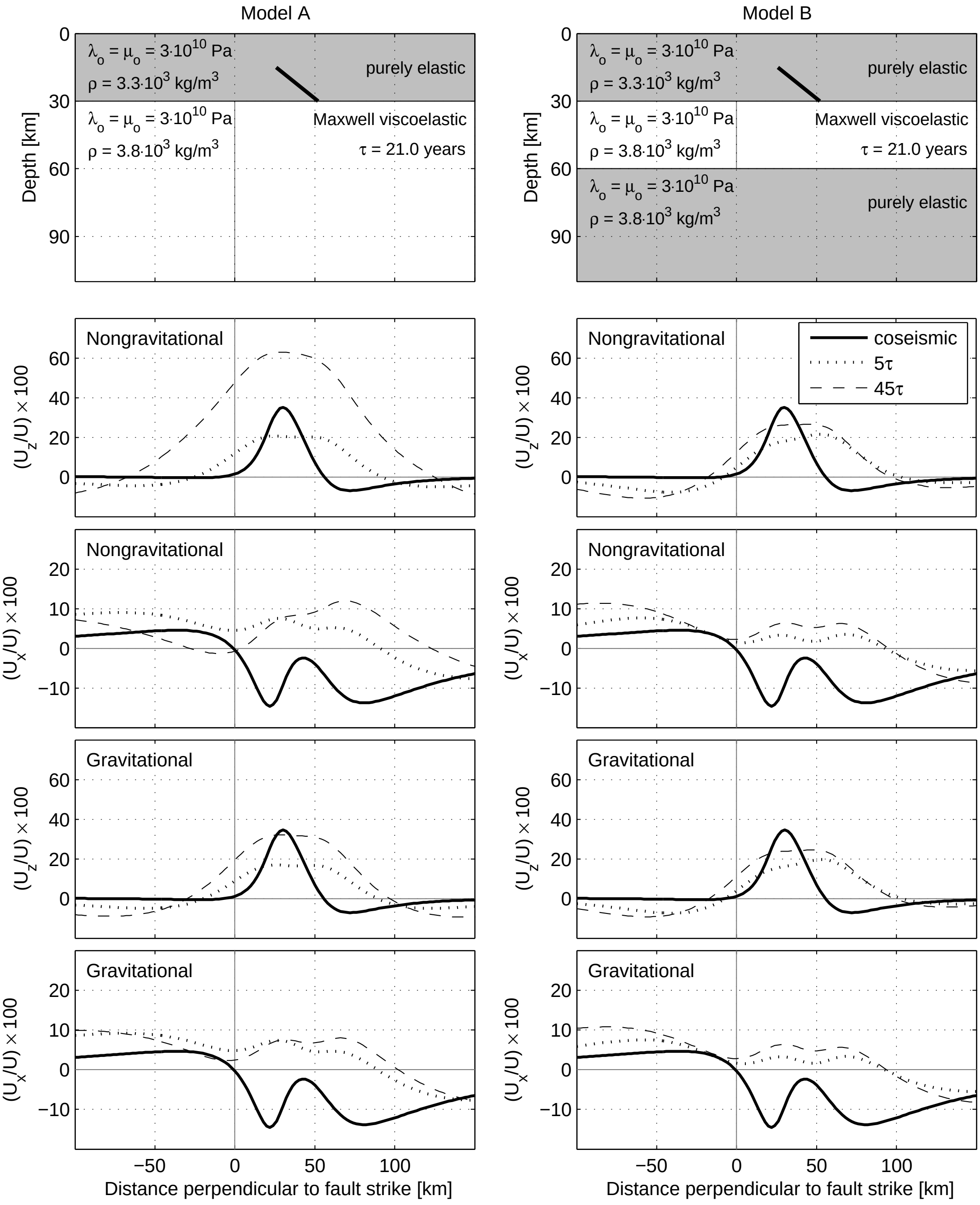

Figure 2.7: *Same as Fig. 2.6, but for a buried thrust fault dipping at* 30 *degree.* U_x *and* U_z *are the displacement perpendicular to the fault strike and the vertical displacement, respectively. These results are comparable with Figs. 3 and 6 of Pollitz (1997) and, for the vertical displacement of Model A, with Figs. 6 and 7 of Rundle (1982).*

is similarly small. Thus, the curvature effect should not be larger than a few percent. Additionally, we should keep in mind that the static displacements decrease with distance by about $1/r^2$. Therefore, the co- and post-seismic deformation calculated by PSGRN/PSCMP should be accurate enough for most applications to present-day data sets.

In comparison with other similar modeling tools published previously, the present software PSGRN/PSCMP includes several improvements:

- A new and consistent approach is used for including the gravity effects in the plane-Earth models.
- The loss-of-precision problem of the Haskell propagator algorithm is fully avoided by the orthonormalization technique.
- The numerical accuracy of the inverse Laplace transform is remarkably improved by using FFT with the anti-aliasing extension.
- A data-base of Green's functions is automatically generated, which can be used repeatedly for modeling the deformation field of different earthquakes.
- There is no restriction on the number of layers of the model used.
- Large-scale earthquakes are represented by a number of rectangular fault planes with different locations and orientations, allowing for the consideration of complicated geometries in an easy and straight-forward way.
- The output includes a complete set of deformation components and the geopotential changes at the surface or any given depth in the form of time series and/or scenarios ("snapshots").

Chapter 3

The effect of input parameters on viscoelastic models of crustal deformation

The increasing quality of data on time-dependent deformation of the Earths surface can be used to extract more details on the spatial and temporal development of earthquake-related crustal deformation. Different variables are involved in these processes, some of them more accurately determined than others. In this Chapter, we model surface deformation on a subduction zone, in a medium composed of an elastic layer over an inelastic half-space. We analyze the effect that three variables (viscosity of the half-space, thickness of the elastic layer and dip angle of the fault plane) that are less accurately determined from data have on the displacement field. We show that the variation of model parameters leads to stable variations in the deformation fields. From the variability analysis, we derive which is the most appropriate data to be used to obtain values for the studied parameters. According to our results, the best data to derive the value of the viscosity is the post-seismic deformation over the area where the rupture takes place, although any area with large magnitude post-seismic displacements can provide profitable data. For the thickness of the elastic layer it is also advisable to use post-seismic data from the area above the fault plane, whereas the dip is better determined by means of co-seismic data.

3.1 Introduction

3.1.1 Motivation

Geodetic data on time-dependent deformation of the Earth's surface can be used as a basis to derive rheological parameters of the crust and upper mantle by forward modeling. With the installation of the GPS system, especially with the recently started continuous measurements and, at the same time, since more Interferograms of Synthetic Aperture Radar (InSAR) data are generated, the sampling rate in monitoring recent crustal movements has drastically increased. This high data quality can be used to extract more details on the space-time development of tectonic processes, especially earthquake-related crustal deformations, and their basic rheological parameters. However, the variables that influence these processes are numerous and the way they affect the deformations is very different. Therefore, it is important to study the effect of the variation of the input parameters before trying to model any real data on crustal deformation.

Seismology might provide accurate values for the magnitude of an event and its seismic moment. Also, the average displacement over the fault plane can be accurately calculated from those values. The distribution of aftershocks immediately after the event leads to information about the depth at which the crust starts to behave viscoelastically rather than elastically. Also the location and orientation of the rupture plane, as well as its length and width, can be deduced from the aftershock distribution or from fault plane solutions. Nevertheless, the depth for the elastic to viscoelastic border and the size and geometry of the fault plane cannot be inferred with the same accuracy as magnitude, seismic moment or average displacement over the fault plane.

Information on surface rupture and deformation at certain points on the surface can be available from geological and geodetic observations. This can lead to further information about the event that caused the deformation and the area where it took place. In addition, post-seismic geodetic measurements on time-dependent deformation can provide information about the viscosity of the lower crust and upper mantle, as well as about the rheological law that governs the relaxation process. Nevertheless, this process takes place very slowly, covering time intervals much longer than those for which accurate geodetic measurements have been carried so far. For this reason, in our analysis of the rheology, we confine ourselves to cases with Maxwell rheology with different values for the viscosity.

3.1.2 Modeling

There are two main modeling concerns. Firstly, the results should provide values that are in the range of what is measurable. Interpretations would be useless if the results from modeling are too small to exceed the resolution of real measurements. Secondly, it is important to check for the stability and uniqueness of the solution when we derive any source parameter from measured data. We must show that a best-fitting model can be found, so that we can find the most likely values for our parameter set. Also, we have to study which parameters influence the results, and how strong this influence is.

In our study, we fix the parameters that are usually accurately determined: seismic moment, average displacement over the fault plane and elastic rock properties for the layered half-space. The displacement on the fault plane is taken to be the same all over the rupture surface: there is no need to complicate the model excessively. Also, the size of the fault plane is not changed, in order to avoid making our analysis too extensive. We chose to model deformations on a medium with an elastic layer over a viscoelastic half-space, since this is a reasonable simplification that nevertheless represents the properties of the crust and upper mantle appropriately. Such a medium has been widely used in former publications (e.g. Cohen, 1980b,a, 1994; Rundle, 1982; Fernández et al., 1996b; Yu et al., 1996b), although the study of the effects of the input parameters on crustal deformation is in general not as systematic and includes not as many studied parameters as in the present paper.

Cohen (1980b) showed the effect that a change in the rheological model has on the modeled results for a strike-slip source, and Cohen (1980a) extended the study to the effects of the depth of the source, its length and width, and the lithospheric thickness. Rundle (1982) analyzed the result of considering a thrust fault in a viscoelastic-gravitational model. Calculations for fault planes that break the elastic layer fully or only partially were compared. Also deformation caused by faults of different size was analyzed, as well as the differences arising from considering a viscoelastic-gravitational medium instead of a purely viscoelastic one. Ma and Kusznir (1994b) studied the effect of the rock parameters, the depth and width of the source and its dip angle for a fault in a three-layer medium. Cohen (1994) analyzed the effect of the viscosity when modeling a dip-slip fault. Also, deformation due to a fault with constant dip was compared to that due to a fault with a variable one. Fernández et al. (1996b) and Yu et al. (1996b) analyzed the effect of gravity on the results for a dipping thrust fault and for a strike-slip fault respectively. They also included calculations for two different dip angles, as well as for fault planes that break the elastic layer fully or only partially. Roy and Royden (2000a,b) considered two layers over the half-space, to analyze how the rheological stratification within the crust affects the formation and long-term evolution of fault systems.

In the following study, three parameters are systematically varied: the thickness of the elastic layer, the viscosity of the underlying half-space and the dip angle of the fault plane. Values for these parameters are, as stated before, generally not very well determined. We analyze the effect that small changes on these three parameters have on the resulting deformation. We created a so-called Reference Model (from now on RM), with average values for the parameters and vary these to compare the effect that this variation has on the deformation. The deformation caused by the RM played the role of synthetic geodetic data that we tried to model by means of different sets of parameters.

For the RM we chose the parameters to represent an earthquake on a subduction zone. Some of the values were taken from a concrete case, namely the 1960 Valdivia earthquake. This event was the largest recorded in the last century, with a moment magnitude of 9.5 (Kanamori, 1977). GPS measurements in 1994 and 1996 in Chile and Argentina (Klotz et al., 2001) show that the deformation associated to the earthquake can still be observed. However, we did not want to confine the analysis to this event, so several parameters were substituted by more general ones.

3.2 Variability analysis

3.2.1 Reference Model

As was already mentioned, some values for the RM were taken from the 1960 Valdivia earthquake. A reference value of 41 km was used for the thickness of the elastic layer, in accordance with receiver function images across the southern Andes (Kind et al., 2001). Since our model considers horizontal layers, lateral inhomogeneities from the crust, typical of subduction zones, cannot be taken into account.

The dip angle of the fault plane was 20^o for the Valdivia earthquake, with a depth for the upper limit of the rupture plane of 6 km (Barrientos and Ward, 1990). These

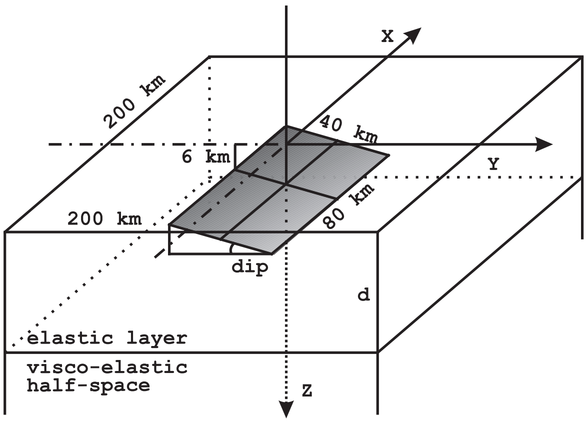

Figure 3.1: *Schematic representation of the geometry of the fault and the medium used in the modeling. The half-space was made up of an elastic layer of variable thickness "d" and a viscoelastic half-space. The origin of the reference system is above the center of the fault plane, with the x-axis parallel to the strike of the fault plane. The upper boundary of the fault plane is located at a depth of 6 km. The fault plane is 80 km long, 40 km wide and has a variable dip angle "dip".*

values were adopted for the RM (see Fig. 3.1). Although the rake differed slightly from 90^o for this event, we modeled a pure dip-slip event, in order not to take too many parameters into account. An arbitrary slip of 5 m and a surface of $80 \times 40 \text{km}^2$ was taken. The slip on the fault plane influences the final deformation in a linear way, so re-scaling the results would be straightforward. Similar media to the one described has been used by Thatcher et al. (1980); Rundle (1982); Thatcher and Rundle (1984) or Fernández et al. (1996b).

In addition to the geometry and position of the source, the physical media had to be described by means of some other values. We choose for these parameters representative values for a subduction zone (Dziewonski and Anderson, 1981). The upper layer was given the following rock properties: $V_p = 6.7$ km/s; $V_s = 3.87$ km/s; $\eta = 2.9 \cdot 10^3$ kg/m^3.

The homogeneous half-space beneath this layer has Maxwell rheological properties. Piersanti (1999), compared post-seismic deformation data with synthetic results and concluded that the viscosity of the asthenosphere beneath the Chilean region should be between $8 \cdot 10^{19}$ and 10^{20} Pa·s. Vermeersen et al. (1998), by means of the study of the effects of the post-glacial rebound, obtained viscosities in the range of 10^{20} up to a few times 10^{20} Pa·s for the upper mantle. According to these studies, we decided to use a reference value of 10^{20} Pa·s for the viscosity.

The rock parameters for the half-space are: $V_p = 8.0$ km/s; $V_s = 4.62$ km/s; $\rho = 3.4 \cdot 10^3$ kg/m^3.

The values listed above were used to create the RM. Subsequent models varying the dip angle, the thickness of the elastic layer and the viscosity of the inelastic half-space were also created. Then the deformation in these models was compared to the one from the RM.

3.2.2 Input parameters

Models with values for the viscosity from $0.5 \cdot 10^{20}$ Pa·s to $2.0 \cdot 10^{20}$ Pa·s in steps of a factor $\sqrt{2}$ were calculated. All the models had Maxwell rheological properties. The range covered by these values is almost one order of magnitude. The reason for this is that the viscosity is not very well known in most of the cases, and some studies show that traditional standard values used in simulations may be incorrect by up to one order of magnitude (Vermeersen et al., 1998).

For each of the values of the viscosity, the thickness of the elastic layer took also different values, from 35 km to 45 km every 2 km. This variation range reflects a realistic inaccuracy of 10% in the determination of this parameter.

For a subduction zone it would be realistic to increase the value of the dip angle with the depth. However, for simplicity, we decided to use a plane for the rupture area, and then vary the dip angle within values for this parameter at different depths in a subduction zone. For this reason, for every combination for the values of the former two parameters, values of the dip angle from 14^o to 24^o every 2^o were also used. A total number of 180 different models were calculated.

Calculations were made for a grid of 41×41 test points, uniformly distributed every 5 km on a surface of 200×200 km^2 with the origin over the center of the fault plane. However, in some cases only a trace of test points perpendicular to the strike of the fault plane is used to show the main dependencies.

3.2.3 Stability

To study the stability of the problem we compared the result of the RM with that of the other models. The difference in displacement was averaged for all the 1681 test points in the area above the rupture plane. The absolute deviation was calculated for every point as follows:

$$\sigma = |Ux_{RM} - U_x| + |Uy_{RM} - U_y|, \tag{3.1}$$

where $(Ux_{RM},\ Uy_{RM})$ are the displacement at that point in the x and y direction for the RM, and $(U_x,\ U_y)$ are the same values for the compared model. Fig. 3.2 shows the averaged absolute deviations from the RM for the horizontal post-seismic displacement during the first 2 years after the event for different sets of parameters. In each of the panels there is only one minimum: the deviations increase with the difference of the input parameters from the ones of the RM. Thus, our variations lead to a unique solution. It may be necessary though to have some limit for the variability of the parameters involved.

3.2.4 Effect of input parameters on co-seismic deformation

To avoid treating fault tip effects along strike we confine ourselves to a trace of 41 test points on the surface, perpendicular to the strike of the fault plane.

The upper panels on Figs. 3.3 and 3.4 show the co-seismic horizontal displacement (U_y, positive along dip direction) along the trace. The shaded area displays the variability of the displacement with the dip angle of the fault plane (Fig. 3.3) or with the thickness of the elastic layer (Fig. 3.4). The fault plane dips towards positive values of the y-axis.

To analyze these curves in more detail, three test points were selected from this trace: B and C, 25 and 60 km distance from the center of the fault, along dip, and A, 10 km distance in the opposite direction. The three points are marked with triangles on the upper panels of Figs. 3.3 and 3.4. Test point A is situated in the area where maximum co-seismic and post-seismic displacement occurs. Test point B is located on a plateau for the co-seismic displacement and, as will be seen later, in the area where the post-seismic deformation changes direction. It will also be shown later that test point

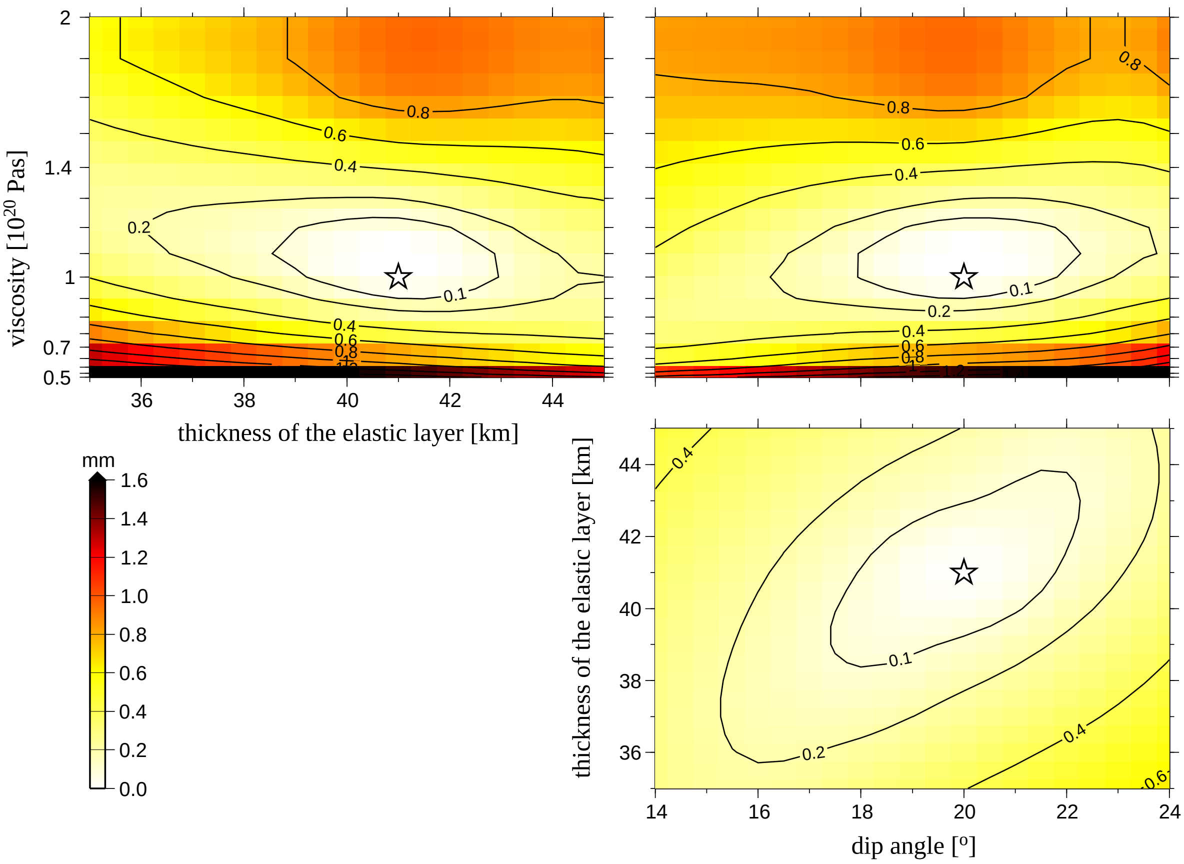

Figure 3.2: *Averaged absolute deviations from the RM [mm] for the horizontal post-seismic displacement (first 2 years after the event) for different sets of parameters. The upper panel shows values for a fixed dip angle of 20°. For the middle panel a thickness of the elastic layer of 41 km was used. In the lower panel, a viscosity value of* $1.0 \cdot 10^{20}$ *Pa·s was used. The minimum (value 0, corresponding to the RM) is marked with a star on every panel. Values for the error increase as the compared models differ more from the RM.*

C lies in the area where the post-seismic displacement reaches the greatest magnitude in the opposite direction to the overall displacement field. For these three points, the lower panels on Figs. 3.3 and 3.4 show the difference in displacement between the RM and models with other values for the parameters.

When the thickness of the elastic layer is fixed (Fig. 3.3), small variations in the dip angle correspond to noticeable changes of the deformation. This parameter influences the geometry and distribution of the deformation in such a strong way that deviations from the RM are very large. Basically, the difference in displacement increases as the magnitude of the displacement does, and deviations are remarkably large even for small magnitude displacements.

We conclude therefore that the effect of the dip angle in the co-seismic displacement is so strong that a value could be resolved best for this parameter by means of the analysis of data on the co-seismic displacements associated to a seismic event.

If the dip angle is fixed and the thickness of the elastic layer varied (Fig. 3.4, deviations have an exaggeration factor of 10 on the upper panel), the deviations for

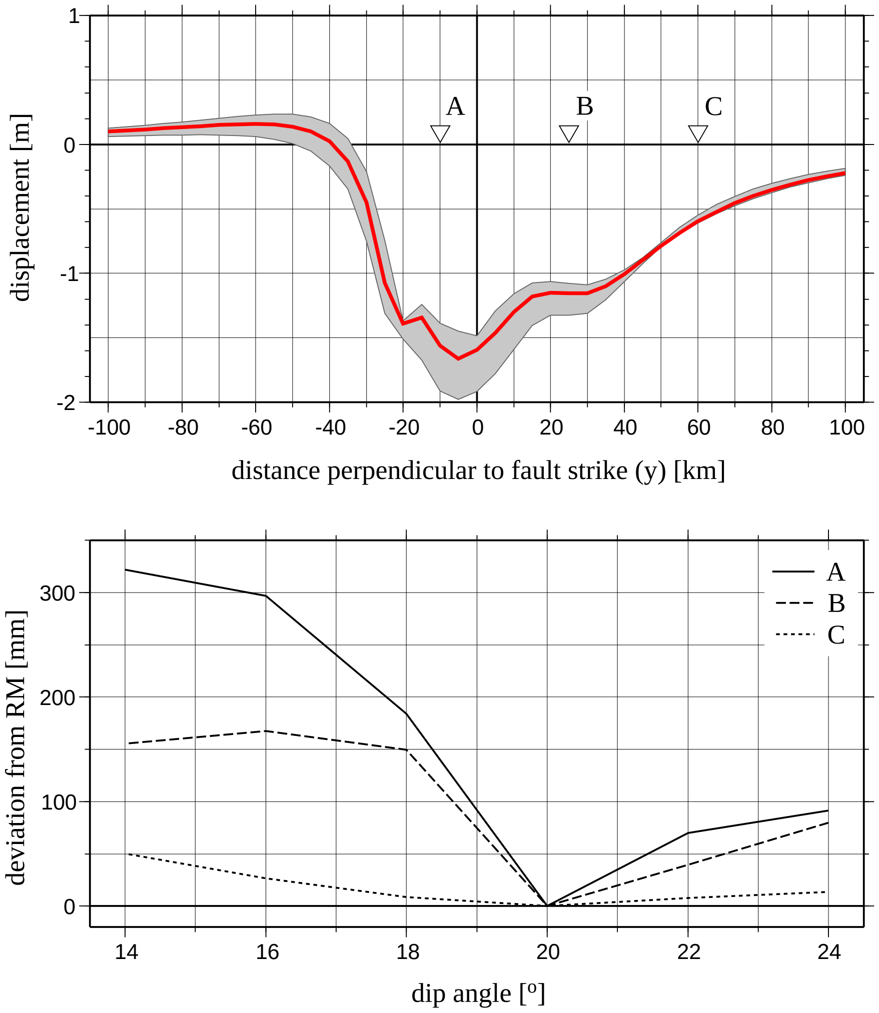

Figure 3.3: *Co-seismic horizontal displacement (U_y) for a trace of points perpendicular to the strike of the fault plane. The fault plane dips towards positive values of the y-axis. The thickness of the elastic layer was fixed to 41 km. The upper panel shows the displacement together with its variability (as a shaded area) when different values for the dip angle of the fault plane are used (no vertical exaggeration for the deviations). The lower panel shows the deviations from the RM for the three points at the surface: A ($y = -10$ km), B ($y = 25$ km) and C ($y = 60$ km) for the different values of the dip angle of the fault plane. Even a small variation of the dip angle leads to notable changes in the displacement.*

the co-seismic displacement are much smaller than in the previous case. There is also a rough direct relation between magnitude of the displacement and its variability. However, this does not hold true for the area where test point B is located. Deviations for this point may be too small to be measured (Fig. 3.4, lower panel). For the test points A and C, any change away from the RM leads to variations over 2 mm.

As we have just shown, the position of the test point can diminish the variability of the displacement drastically. In the case that measurements are taken at such points, it may not be possible to infer a value for the elastic layer thickness only by means of the analysis of the co-seismic deformation. Other information, like the fault plane solution or aftershocks distribution, may be needed to constrain the value of this parameter.

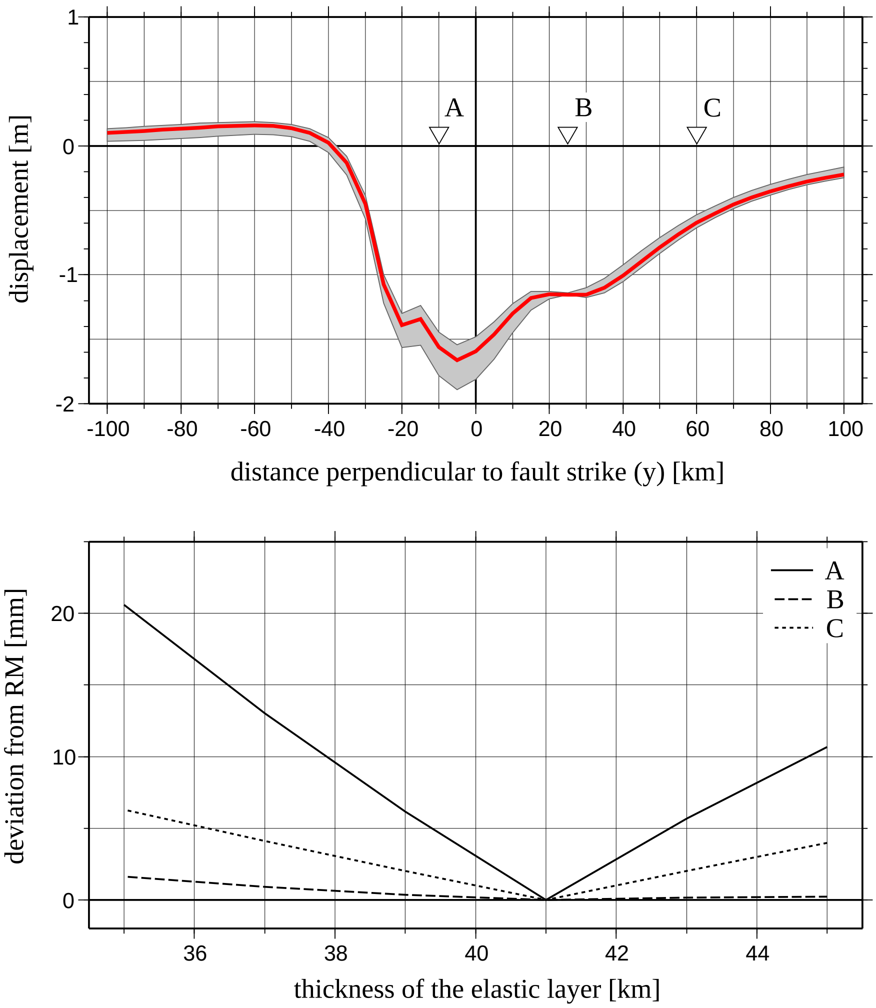

Figure 3.4: *Co-seismic horizontal displacement (U_y) for a trace of points perpendicular to the strike of the fault plane. The fault plane dips towards positive values of the y-axis. The dip angle was fixed to 20°. The upper panel shows the displacement together with its variability (as a shaded area) when different values for the thickness of the elastic layer are used (vertical exaggeration for the deviations: factor 10). The lower panel shows the deviations from the RM for the three points at the surface: A ($y = -10$ km), B ($y = 25$ km) and C ($y = 60$ km) for the different values of the thickness of the elastic layer. Notice the different vertical scale here and in Fig. 3.3. In this case, deviations for point B are very small.*

It should be noted that the difference in deformation associated to a change of the thickness of the elastic layer depends on the contrast in the two Lamé's constants between the elastic layer and the ones for the viscoelastic half-space. However, this study did not analyze this possibility of modifying the model, and was limited to the contrast induced by the relaxation with time of the physical rock parameters in the viscoelastic half-space.

3.2.5 Effect of input parameters on post-seismic deformation

We consider again the trace of 41 test points perpendicular to the strike of the fault plane. For these points, the red line in Fig. 3.5 show the horizontal post-seismic displacement in the y-direction for the first two years after the event. Its variation with the three studied parameters is represented by means of the shaded area. The fault plane dips towards positive values of the y-axis.

Varying the three parameters at the same time leads to big changes in the results. We only include the results starting from the value $\eta = 0.7 \cdot 10^{20}$ Pa·s. A value for the viscosity of $0.5 \cdot 10^{20}$ Pa·s only leads to bigger deviations. The values for the parameters that lead to the top and bottom values for the displacement are listed in Table 3.1.

Although the variability of the displacement is remarkable, it is not evident which variables have a stronger influence, and how this influence depends on the distance to the fault plane. This is now analyzed in greater detail, first taking account of the location of the test point, and then varying only one of the parameters at a time.

3.2.6 Distance to the fault plane

If we consider the test points A, B and C as before, we again observe that the different parameters have a different influence on the deformation depending on the location. Figure 3.6 shows the deviations for the post-seismic displacement for the first two years after the event at these three test points. At test point A (Fig. 3.6, first column), located in the area of maximum deformation, deviations are on average greater than at the other two test points. In the two lower panels, variations with the dip angle are much smaller than those with the other two parameters, showing that varying the dip angle does not influence the results as much as the viscosity or the thickness of the

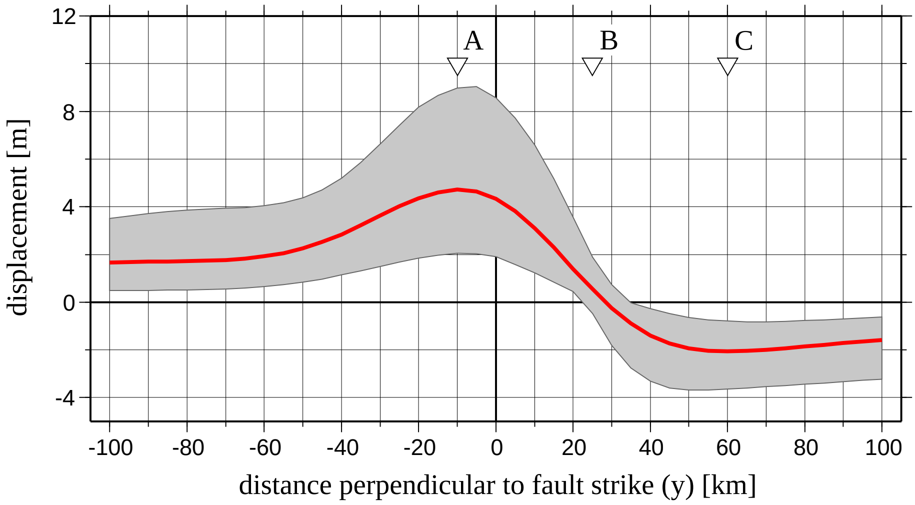

Figure 3.5: *Horizontal post-seismic (first two years after the event) displacement perpendicular to the strike of the fault plane for a trace of points perpendicular to the strike of the fault plane. For every point, the displacement corresponding to the RM is plotted (red line), together with its variation when the thickness of the elastic layer, the viscosity of the half-space and the dip angle of the fault plane changes. See Table 3.1 for the parameters that lead to the maximum or minimum displacement.*

distance to fault plane center [km]	model parameters leading to largest deviation					
	top			bottom		
	dip angle [^{o}]	thickness [km]	viscosity [10^{20}Pa·s]	dip angle [^{o}]	thickness [km]	viscosity [10^{20}Pa·s]
-100 to -15	24	35	0.7	14	45	2.0
-10	18	35	0.7	14	45	2.0
-5	18	35	0.7	24	45	2.0
0	18	35	0.7	22	45	2.0
5	16	35	0.7	24	45	2.0
10	14	35	0.7	24	45	2.0
15	14	35	0.7	24	45	2.0
20	14	35	0.7	24	45	2.0
25	14	35	0.7	24	35	0.7
30	14	45	0.7	24	35	0.7
35 to 100	14	45	2.0	24	35	0.7

Table 3.1: *Value list for the model parameters that lead to the top or bottom values for horizontal displacements when the three parameters change. For example, on the surface, 5 km away from the origin of coordinate in the dipping direction, the model that leads to the maximum displacement is the one with a dip angle of 16^o, an elastic layer 35 km thick and a viscosity of* $0.7 \cdot 10^{20}$ *Pa·s. The values for the resulting displacement were used for the shaded area on Fig. 3.5.*

elastic layer. The same holds true for test point C (Fig. 3.6, last column), although in this case the magnitude of the deviations is much smaller.

On the contrary, test point B (Fig. 3.6, middle column) shows that deformation in this area is actually more sensitive to the dip angle than to the other two parameters (Fig. 3.6, middle column, lower two panels). However, the magnitude of these deviations is still smaller than the deviations at test point A.

It should be noticed that each panel in this figure shows results for a single test point. In some cases there are other local minima apart from the one corresponding to the RM, or the models around the latest show small deviation. This simply demonstrates that it would be very difficult to infer the value of our parameters from the deformation observed at a single test point.

These results provide important information on the optimal location of the test points required to extract information from post-seismic data. Measurements around test point A or C will be useful for determining the thickness of the elastic layer or the viscosity of the half-space, but will provide poor information on the dip angle, whereas the area around point B will behave the opposite way.

The area of maximum deformation provides data that can be measured easily. In addition, the results depend heavily on the viscosity, so interpretation of the measurements could provide reliable values for this parameter. Measurements around test points B and C, although smaller in magnitude, could be useful for obtaining results about the other two variables if, as might be the case, no reliable value is available for the viscosity.

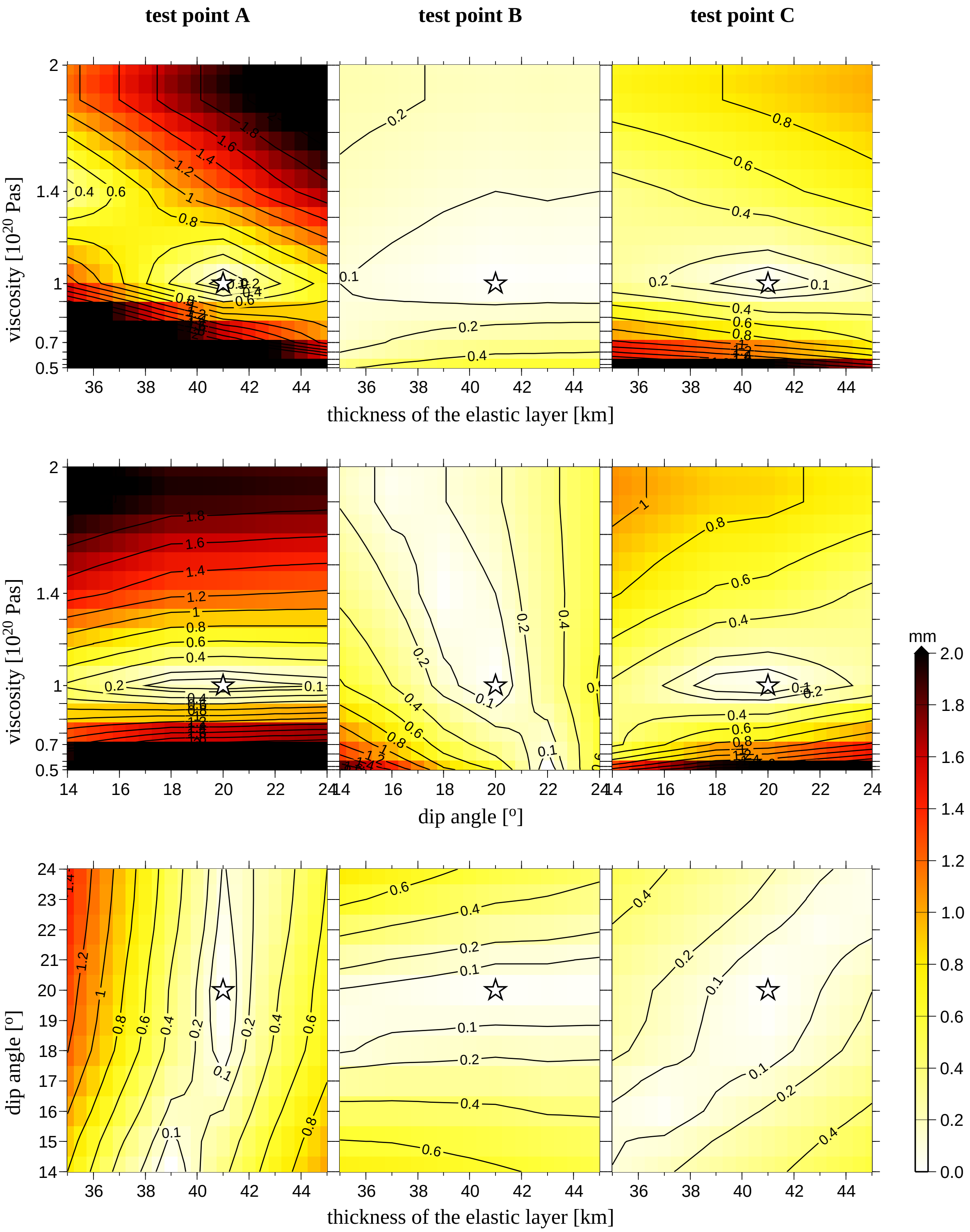

__Figure 3.6:__ Deviations from the RM (mm) for the post-seismic displacement for the first two years after the event for points A, B and C, as indicated in Fig. 3.5. The first row shows values for a fixed dip angle of 20°. For the second row a thickness of the elastic layer of 41 km was used. In the third row, a viscosity value of $1.0 \cdot 10^{20}$ *Pa·s was used. The minimum, corresponding to the RM, is marked with a star on every panel.*

3.2.7 Effect of single input parameters

We plotted the horizontal (U_y) post-seismic displacement for the trace of test points perpendicular to the fault plane strike (Fig. 3.7). On the upper panel, we represent the variability of the displacement with the viscosity of the half-space. Once again, we only include the results starting from the value $\eta = 0.7 \cdot 10^{20}$ Pa·s, since a value for the viscosity of $\eta = 0.5 \cdot 10^{20}$ Pa·s only leads to bigger deviations from the RM.

The magnitude of the displacement increases as the viscosity decreases and vice versa. The values for the viscosity that lead to the greater or smaller displacement are listed in Table 3.2. At test points where the displacement is large, there is also large variability of the results. This indicates that data from areas of large deformation is appropriate for finding a value for the viscosity.

distance to fault plane center [km]	model parameters leading to largest deviation					
	half-space viscosity [10^{20}Pa·s]		thickness of the elastic layer [km]		dip angle of fault plane [^{o}]	
	top	bottom	top	bottom	top	bottom
-100 to -10	0.7	2.0	35	45	24	14
-5	0.7	2.0	35	45	18	14
0	0.7	2.0	35	45	18	22
5	0.7	2.0	35	45	16	24
10	0.7	2.0	35	45	14	24
15	0.7	2.0	35	45	14	24
20	0.7	2.0	35	45	14	24
25	0.7	2.0	41	35	14	24
30 to 100	2.0	0.7	45	35	14	24

Table 3.2: *Value list for the model parameters that lead to the top or bottom values for horizontal displacements when one of the parameters changes. For example, on the surface, 5 km along dip from the origin of the coordinate system, when only the viscosity changes, the model that leads to the maximum displacement is the one with a viscosity of* $0.7 \cdot 10^{20}$*Pa·s. The values for the resulting displacement were used for the shaded area on the upper panel (half-space viscosity), central panel (thickness of the elastic layer) and lower panel (dip angle) on Fig. 3.7.*

The central panel of Fig. 3.7 shows the same curve with its variability when only the thickness of the elastic layer changes. Basically, once again there is an inverse relationship between this parameter and the magnitude of the displacement: smaller magnitude displacements correspond to the model with a thicker elastic layer. Nevertheless, 25 km away from the center, where the displacement almost vanishes, the maximum displacement corresponded to the RM itself (see triangles in Fig. 3.7, central panel). The values from the rest of the models are smaller. The model that leads to the minimum displacement at this test point is the one with an elastic layer 35 km thick, the same as for all the test points with negative displacement (see Table 3.2). In this case, the greatest variation occurs where the deformation is greater as long as the displacements are positive (along dip). When the displacement takes negative values, this relation does not hold, and the magnitude of the deviations from the RM

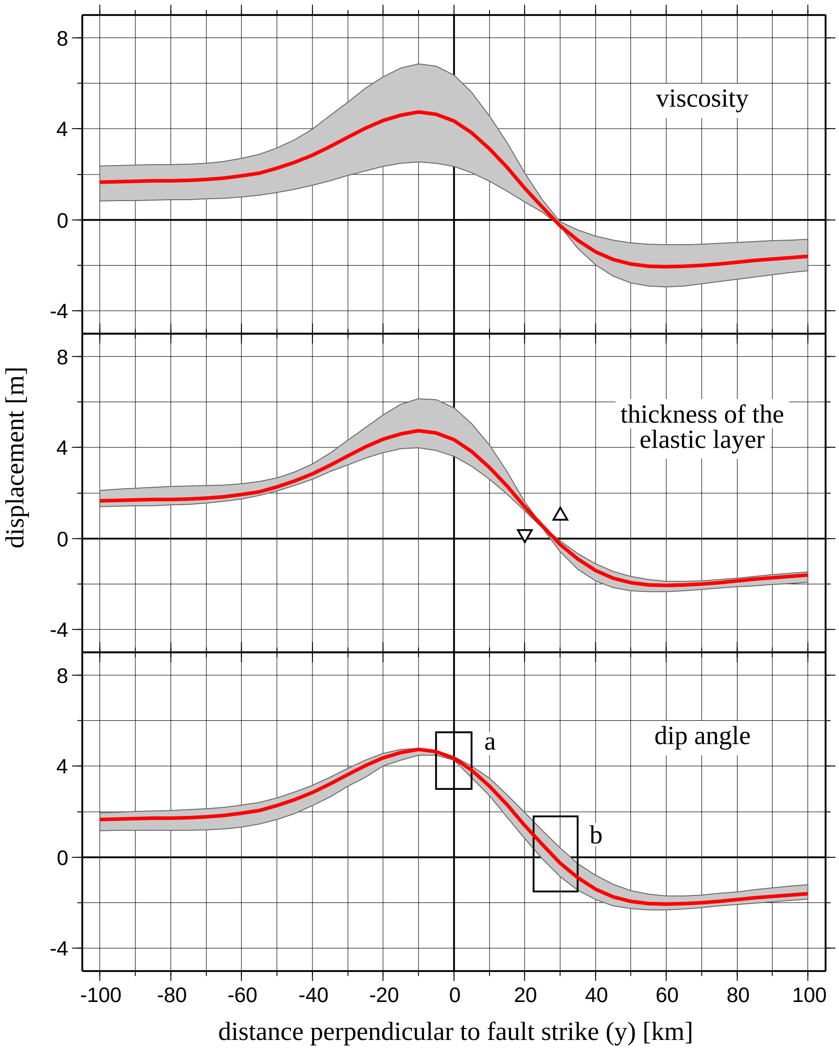

Figure 3.7: *Horizontal post-seismic (first two years after the event) displacement* U_y *for a trace of points perpendicular to the strike of the fault plane. In every panel the displacement is plotted with a red line, and for every point also the variation of the displacement with one parameter is included. The upper panel shows the variation when viscosity changes, whereas the middle and lower panels show the variation with the thickness of the elastic layer and the dip angle of the fault plane, respectively. The triangles in the middle panel show the test point where the thickness of the elastic layer for maximum and minimum displacement changes. Box "a" in the lower panel shows the area for which the dip angle of the fault plane for maximum and minimum displacement changes. Box "b" shows the area for which a change in the dip angle can lead to a change in the sign of the displacement. For the parameters that lead to the maximum or minimum displacement see Table 3.2.*

is generally smaller. This means that data from the area of maximum displacements is the most appropriate when looking for a value for the elastic layer thickness.

The variation of the dip angle of the fault plane affects the displacement in a more complicated way (Fig. 3.7, lower panel). The dip angle values that provide the top and bottom values for the displacements change more smoothly than in the case of the other two parameters (see box a in Fig. 3.7 and Table 3.2). Moreover, box b shows an area where changing the parameters for the model can lead to a change in the direction of the displacement. In addition, the greatest variability of the displacement does not correspond to the test points where the magnitude of the displacement is greatest (although this was the case for the co-seismic displacement, Fig. 3.2). The dip angle, in contrast to the viscosity or the thickness of the elastic layer, is a geometrical variable that only affects the distribution of the displacements and not their development in time. These facts stress the importance of observation points in the area where the post-seismic displacement changes direction. Data from this area should be used to resolve the value of the dip angle.

3.3 Conclusions

The spatial and temporal development of earthquake-related crustal deformation processes involve multiple variables, some of which are less precisely determined than others. Former works on forward modeling usually include no analysis of the effect of these parameters on the deformation or this analysis is not systematic (Cohen, 1980b,a; Thatcher and Rundle, 1979). Furthermore, usually only one variable is analyzed, or the study is constrained to not more than two or three values for each variable (Fernández et al., 1996b; Yu et al., 1996b). In the present study, the effect of three different variables (lithospheric thickness, asthenospheric viscosity and dip angle of the fault) is analyzed in detail for the co- and post-seismic deformation due to a thrust event, to ascertain how heavily results depend on which parameter. From this analysis the following conclusions were derived:

- When analyzing the **co-seismic** displacement, a strong dependency on the dip angle of the fault plane is found. Points with large displacements show also a large variability when the dip angle varies. The area over the rupture plane is the one where the largest displacements take place. Therefore, surface measurements in this area are the most suitable for ascertaining the most likely value for the dip angle.

  By contrast, varying the thickness of the elastic layer leads to small differences in general, especially small in the area immediately beyond the surface projection of the lower end of the rupture plane. This indicates that co-seismic displacement measurements, especially around the mentioned area, are not recommendable for trying to ascertain an accurate value for this parameter.

- In the analysis of the **post-seismic** deformation we find that, on average, deviations from a reference model are large above the rupture plane when varying the viscosity and the thickness of the elastic layer. In this area, the dip angle does not influence the results as much as the other two parameters. Further away from the rupture surface along dip direction, in the area immediately beyond the surface projection of the lower end of the rupture plane, the dip angle becomes the most influential parameter. Further away, where the magnitude of the horizontal displacement reaches another maximum, the viscosity and the thickness of the elastic layer have again a greater effect than the dip angle of the rupture surface.

Accordingly, measurements in areas of large post-seismic displacements are suitable for deriving a value for the viscosity. In particular, above the rupture area, values depend heavily on this parameter. The same region can also provide data that is useful for ascertaining the thickness of the elastic layer, although for this parameter the area where the minimum displacement occurs is not as appropriate as for the viscosity.

The dip angle, in general, cannot be accurately derived using post-seismic deformation data. The magnitude of the variability associated with this parameter is very small. The best place to find a value for this parameter is the area where the post-seismic displacement changes direction.

Chapter 4

Inversion for rheological parameters from post-seismic surface deformation associated with the 1960 Valdivia earthquake, Chile

Data collected during two Global Positioning System (GPS) campaigns in 1994 and 1996 across Chile and western Argentina (22 stations), in the area where the $M_w = 9.5$ May 22^{nd} 1960 Valdivia earthquake took place, shows ground motion velocities that cannot be fully explained by the elastic strain accumulation during the inter-seismic phase of an earthquake deformation cycle. We use dislocation models to reproduce the observed velocities, with a 3D source in a medium with one elastic layer overlying a Maxwell viscoelastic half-space, and a planar rupture surface with uniform coseismic slip. The reason for avoiding a more detailed and elaborated model is that knowledge about the Valdivia earthquake source parameters and the area where the event took place is poor. We focus therefore on examining the first-order post-seismic deformation, and ignore finer details about the heterogeneity of the Earth. By means of a grid search inversion over more than a million different models, we derived the most likely values for some of the medium and source parameters involved in the deformation process, namely viscosity (η), thickness of the elastic layer (D), average slip on the rupture surface (U_0) and the seismic coupling coefficient (χ). According to our study, the optimum values are: $\eta = 10^{20}$ Pa·s, $D = 46$ km, $U_0 = 15$ m and $\chi = 96$. A clear difference is seen between the surface deformation caused by silent-slip on the rupture surface and the one caused by post-seismic relaxation processes, two possibilities proposed to explain the anomalous velocities. We find that the deformation associated with the 1960 Valdivia event can still be observed after several decades and it is the most likely explanation for the velocity component that cannot be explained by plate convergence. Our model also predicts that this deformation will still be measurable for several more decades. Our model reproduces the first-order pattern of the measured GPS velocities, showing good agreement with recent finite element studies, with the advantage of simplicity and short computation time, allowing the extensive search for the best fitting model.

4.1 Introduction

With the establishment of the Global Positioning System (GPS), the accuracy of observations of time-dependent deformation of the Earth's surface has significantly improved and continues to do so. Also, with an increasing number of sites providing continuous measurements and with more numerous Interferograms of Synthetic Aperture Radar (InSAR), both the sampling rate and areal coverage in monitoring recent crustal movements have drastically increased. The data obtained can be used to extract more details about the space-time development of tectonic processes, such as earthquake-related crustal deformations, and their basic rheological parameters, in a way that was not possible in the recent past. Post-seismic relaxation, plate convergence or silent earthquakes, for example, can now be studied with a high accuracy, despite the intrinsically low magnitude of the deformation involved.

Thanks to this recently acquired data accuracy, an interesting feature can be observed around the area where the great 1960 Valdivia earthquake took place. GPS velocities for sites at latitudes further north have a direction parallel to the convergence between the Nazca and South American plates, but observations from sites located close to the area of the earthquake are not coherent with deformation caused by plate motion, but show anomalous seaward velocities (Klotz et al., 2001; Khazaradze and Klotz, 2003). The deformation further north can be fully explained by the elastic strain accumulation during the inter-seismic phase of an earthquake deformation cycle. These velocities agree with a full rate of convergence, in other words, a 100% locking of the Andean Subduction Zone is needed to explain them. On the contrary, other processes must be involved to produce the deformation observed in the area of the Valdivia earthquake.

An explanation for this incoherence could be that the Valdivia earthquake may still have an influence on the crustal motion in this area. Very large earthquakes, such as subduction events of $M_w \geq 9$, may induce large stresses in the mantle over a very broad region, and the relaxation process may cause prolonged crustal deformation far

▷

Figure 4.1: *Map of the study area. The triangles show the 22 GPS sites used for this work. Thin arrows and error ellipses show the measured annual velocities (Klotz et al., 2001; Khazaradze and Klotz, 2003). Numerical values for these velocities are shown in Table 1. The thick arrows display the annual velocities obtained by means of the best-fitting model. The dashed-line rectangle shows the projection of the rupture surface used for calculations. The thick black line shows the position of the Chile trench. Squares display the most important cities. White dots display the seismicity (events with magnitude at least 5) between 1961 and 1981 from the South American SISRA Catalog (Askew and Algermissen, 1985). Stars show the location of the epicenter of the 1960 Valdivia earthquake after Talley and Cloud (number 1, (Talley and Cloud, 1962)), Cifuentes (number 2, two subevents, (Cifuentes and Silver, 1989)) and Krawczyk (number 3, (Krawczyk and the SPOC team, 2003)). Areas delimited by dashed lines (A, B and C) display latitude intervals for the panels shown in Fig. 4.5.*

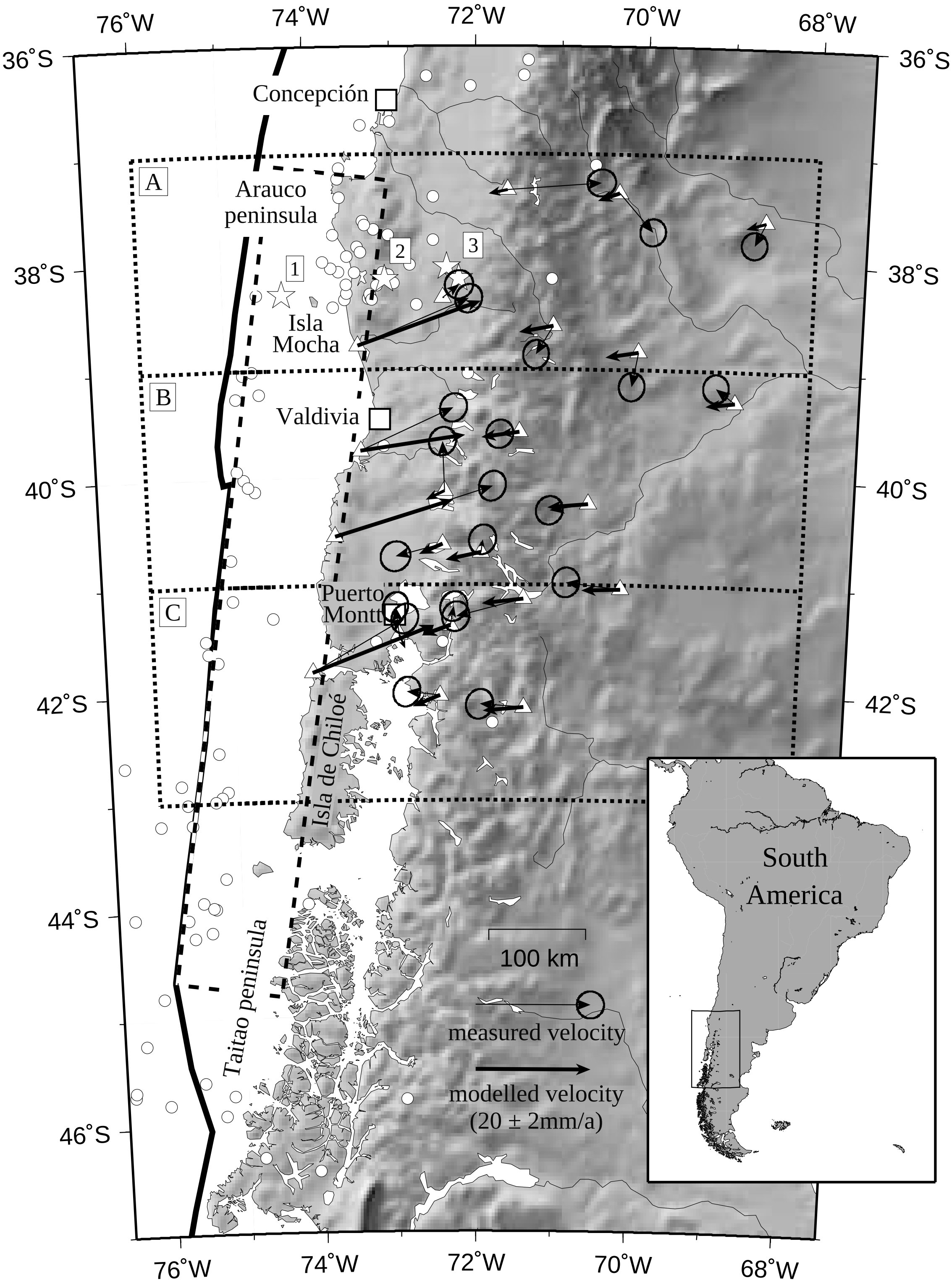
76˚W
74˚W
72˚W
70˚W
68˚W
36˚S
38˚S
40˚S
42˚S
44˚S
46˚S
Concepción
A
B
C
Arauco peninsula
1
2
3
Isla Mocha
Valdivia
Puerto Montt
Isla de Chiloé
Taitao peninsula
100 km
measured velocity
modelled velocity (20 ± 2mm/a)
South America

away from the coseismic rupture zone for several decades after the event (Nur and Mavko, 1974; Thatcher and Rundle, 1984). Other possible explanations could be aseismic slip on the coseismic rupture surface (Nason and Weertman, 1973), deep slip on its down-dip prolongation or even a combination of the three processes. Freymueller et al. (2000) and Zweck et al. (2002) interpreted the inter-seismic crustal motion observed on the western Kenai Peninsula as resulting from a delayed or continuing post-seismic transient response of the 1964 $M_w = 9.2$ Alaska earthquake. Savage and Plafker (1991) and Brown et al. (1977) attributed the immediate post-seismic relaxation after this event to post-seismic slip on the plate interface directly downdip from the coseismic rupture. Kasahara (1975) suggested delayed strain release by aseismic faulting following the 1973 Nemuro-Oki earthquake, Japan. Fitch and Scholz (1971) explained post-seismic movements after the 1946 Nankaido earthquake, Japan, with a combination of reversed slip on the coseismic rupture surface and delayed forward slip on the deeper parts of the fault.

Deep slip was also suggested for the 1960 Valdivia earthquake (Linde and Silver, 1989; Barrientos et al., 1992). However, these and other early works (Plafker and Savage, 1970; Plafker, 1972; Barrientos and Ward, 1990) tried to explain the observed deformation around the area of the event using elastic models and, in most cases, including both co- and post-seismic deformation with the observations. This approach cannot properly consider effects from viscoelastic relaxation, which might not be negligible. Piersanti (1999) modeled uplift and uplift rates by means of a layered spherical Earth model with Maxwell rheology, but this work was based on data from only two stations. Khazaradze et al. (2002) modeled GPS velocities as a combination of plate motion and continuous post-seismic crustal deformation using a 3-D viscoelastic finite-element model. However, the geometry of the subduction zone in this area is not well constrained by data, and the sensitivity of the results to the model parameters remains unclear. Their work was continued by Hu et al. (2004), including a separate analysis of deformation due to the earthquake alone and deformation due to fault locking. Choosing 2-3 values for their model parameters, they did a simplified check for the sensitivity of their results.

In this study we used data from 22 GPS stations across Chile and western Argentina (Fig. 4.1), collected during two GPS campaigns in 1994 and 1996 (Klotz et al., 2001; Khazaradze and Klotz, 2003). We modeled the measured deformation by means of the method described in Chapter 2. This method allows us to consider co- and post-seismic deformation processes in an adequate manner. Its speed also allows us to carry out a systematic global search for an optimum model with a fairly broad parameter space. These facilities are used to search for an explanation for the anomalous velocities around the earthquake's location. We also carried out an inversion for rheological and structural parameters in this area using the GPS data, and found the most likely values for these parameters and their reliability. We also estimate the time for which deformation due to the earthquake will still be measurable.

4.2 The 1960 Valdivia earthquake

The Valdivia earthquake of May 22^{nd}, 1960, is until now the largest event ever recorded by a seismic network. The main shock consisted of two sub-events adding up to a moment magnitude of 9.5 (Kanamori, 1977). The destruction area extended for more than 800 km in a north-south direction. Surface deformation related to the earthquake, including both uplift and subsidence relative to sea level, was observed over an even larger area of southern Chile (Talley and Cloud, 1962; Álvarez, 1963; Plafker and Savage, 1970).

Despite the intensive scientific and engineering studies made shortly after the disaster, surprisingly little has been published concerning the generative mechanism of this event. Nor is much information about the area of occurrence of the event. Most studies related to the South American Subduction Zone have been carried for latitudes further north (Jordan et al., 1983; Cahill and Isacks, 1992; Araujo and Suárez, 1994) or, in the best of the cases, only over the northernmost part of the Valdivia rupture area (Tichelaar and Ruff, 1991; Bohm et al., 2002; Krawczyk and the SPOC team, 2003; Lüth et al., 2003). In the following sections, we briefly present background information relevant to our work, i.e. the subduction zone and the source mechanism of the event and its geometry.

4.2.1 Tectonic setting and seismicity

The 1960 Valdivia earthquake sequence ruptured about 1000 km of the southernmost section of the South American Subduction Zone. In this region, the Nazca Plate is being subducted beneath South America along the Peru-Chile Trench at a rate of 78 mm/a, according to the analysis of sea-floor paleo-magnetic data (DeMets et al., 1994; Somoza, 1998). Space-geodetic estimates provide a value considerably lower for the convergence velocity (66 mm/a (Angermann et al., 1999); 69 mm/a (Norabuena et al., 1998, 1999)). These results are based on observations over a relatively short time span, and may therefore be affected by short-term deformation processes, while paleo-magnetic studies provide only a long-term average velocity that may not be representative of the current convergence rate. We favored for this reason the use of the results from the recent geodetic studies.

4.2.2 Mechanism and location

There were no fault displacements at the surface to provide direct geological evidence as to the orientation and sense of slip on the causative fault or faults (Álvarez, 1963). Similarly, the seismological data was generally inadequate to permit either reliable focal mechanism solutions or precise delineation of the focal region (Plafker and Savage, 1970). No fault-plane solution is available for the main shock of the 1960 sequence because the first arrivals were masked on most seismograms by the large foreshock that immediately preceded it (Cifuentes and Silver, 1989).

Precise location of the epicenter of the main shock was not possible for the same reason. The U. S. Coast and Geodetic survey located the epicenter on the continental shelf, approximately 80 km offshore from the coastline and 60 km west of Isla Mocha (38.30^o S, 74.30^o W, (Talley and Cloud, 1962); see Fig. 4.1 for these geographical locations). Cifuentes and Silver (1989) relocated the sequence of the earthquake using the master-event technique. According to her work, the two sub-events of the main shock were relocated to 38.05^o N, 72.34^o W and 38.16^o N, 72.20^o W. Recently, Krawczyk and the SPOC team (2003) presented for the first time the slab geometry of this area, based on a near-vertical seismic reflection experiment, and proposed a new location at 73.08^o W. This recent work gives an idea of how many aspects of this earthquake are still not well known.

4.2.3 Coseismic slip on the rupture surface

Plafker and Savage (1970) and Plafker (1972), by means of the dislocation analysis of vertical surface deformation several years after the earthquake, found that the most plausible model for the Valdivia earthquake would be a fault with an average slip of about 20 m. Strain modeling suggested, however, that the slip required to satisfy the surface displacement may be as large as 40 m. Kanamori and Cipar (1974) estimated an average dislocation of 24 m from the analysis of a long-period strain seismogram. Barrientos and Ward (1990) employed surface deformation data from more than 300 data points to investigate the slip distribution on the rupture surface. Several slip peaks appeared on this surface, in some cases exceeding 40 m. However, the average repeat time has been estimated to be 128 ± 31a (Nishenko, 1985) and, by the present convergence rate of the Nazca and South America plates, much less slip would accumulate during such a period.

4.2.4 Rupture surface geometry

The Wadati-Benioff zone is delineated well enough to infer the dip of the subducting Nazca Plate only in the Arauco Peninsula region, the northern section of the rupture area of the Valdivia earthquake. There, the Wadati-Benioff zone does not extend deeper that 160 km. The Nazca Plate in the Arauco Peninsula region dips at a shallow angle of about 15^o to a depth of 40 km, where it steepens to a moderate dip of about 30^o to reach a depth of about 125 km beneath the volcanoes (Bohm et al., 2002; Krawczyk and the SPOC team, 2003; Lüth et al., 2003). The average dip might be larger than for the Arauco Peninsula region, as the dip in the region north of the 1960 rupture area (Jordan et al., 1983; Cahill and Isacks, 1992). It might also be less, because of the increase in buoyancy due to the southward decrease in the age of the oceanic lithosphere being subducted. Plafker and Savage (1970) estimated the dip angle to be of the order of 35^o. Plafker changed this value to 20^o in a later work (Plafker, 1972).

The width of the rupture surface of the Valdivia earthquake is poorly constrained. An approximate measure is obtained from the dip of the Nazca Plate in the Arauco Peninsula region and the probable depth range of faulting. The width of the aftershock distribution, excluding the events close to the trench axis as they are not on the main thrust zone, yields an approximate width for the rupture area of 140 km (Cifuentes and Silver, 1989). However, the depth of aftershocks are poorly determined, and thus the depth range is not well constrained.

The rupture length of the main shock is also not well known. In contrast to the northern endpoint, the southern endpoint is not clearly determined, due to the lack of information south of 45^oS. In any case, the sites we used for our analysis are located around its northern half (Fig. 4.1). Thus, the exact southern end of the rupture is not critical for our study. Benioff et al. (1961) made the first determination of fault length from instrumental data, suggesting a value of 960 km to 1200 km. The distribution of aftershocks during the first month leads to a value of 930 km (Cifuentes and Silver, 1989). An estimate of rupture length can also be obtained from the extent of crustal deformation. The southernmost point of vertical displacement measured by Plafker and Savage (1970) is at 45.21^o S, but the extent of vertical displacement could reach as far south as the Taitao Peninsula, where a few centimeters of uplift were reported after the earthquake. The rupture length can be estimated as the distance between the initiation of the earthquake and the southern limit of crustal deformation. This length is 800 km to the southernmost measured point, and 920 km to the Taito Peninsula. According to this, Cifuentes and Silver (1989) proposed a value of 920 ± 100 km for the rupture length, within the range of values previously presented (Benioff et al., 1961; Press et al., 1961).

4.3 Modeling

For our study of the post-seismic deformation associated with the 1960 Valdivia earthquake, we use observations from 22 sites from the SAGA (South American Geodynamic Activities) GPS network (Klotz et al., 2001; Khazaradze and Klotz, 2003). The stations cover the northernmost part of the rupture area of the 1960 event (Fig. 4.1). The values used are listed in Table 4.1. The collected data was processed and transformed to a fixed South America reference frame (Klotz et al., 2001).

The mean value of position residuals for these stations, reflecting the achieved regional network precision, is of the order of 2 mm and 5-7 mm for horizontal and vertical displacement, respectively. Since the expected surface uplift in the Andean Subduction Zone does not exceed 2 mm per year, two observations separated by 2 years are not sufficient to resolve the possible vertical motions with adequate confidence. For this reason we only considered the two horizontal components of the deformation in our work.

As already mentioned, different approaches have been used by other authors to model the subduction zone where the Valdivia earthquake took place. The most important conclusions from their analyze are:

- The predicted deformation is notably sensitive to the distribution of slip on the rupture surface (Linde and Silver, 1989; Barrientos and Ward, 1990). However, external constraints are needed to realistically resolve this parameter.

- Effects due to post-seismic relaxation are not negligible. When considered, models with viscosity in the range of 10^{19} (Khazaradze et al., 2002; Hu et al., 2004) to a few times 10^{20} Pa·s (Piersanti, 1999) provide good results for this area.

- The geometry of the rupture surface is an important parameter (Klotz et al., 2001; Khazaradze et al., 2002; Khazaradze and Klotz, 2003; Hu et al., 2004). However, external information is required to describe it. Unfortunately, such information is scarce or not available in detail for the Valdivia area.

- The structure of the medium layering has also a significant effect on the modeled data (Piersanti, 1999). Lateral inhomogeneities also have a significant effect on

Station ID	Longitude [^{o}]	Latitude [^{o}]	W-E vel. [mm/a]	1σ error [mm/a]	S-N vel. [mm/a]	1σ error [mm/a]	correl. coeff.
ANTU	288.3745	−37.3358	16.4	2.1	1.3	2.0	0.05
AUMA	291.4048	−37.6065	−1.9	1.9	−4.0	2.0	0.01
BARI	288.5865	−41.1321	−11.7	2.0	−3.2	2.2	0.09
CALF	286.6116	−39.7539	16.3	2.0	7.4	2.1	0.12
CEPI	289.3679	−40.2494	−6.7	2.0	−1.2	2.1	0.07
CHOL	287.5584	−42.0279	−5.8	2.0	0.6	2.2	0.12
CHOS	289.6855	−37.3608	5.9	1.9	−6.7	2.0	0.04
COMA	289.7824	−41.0363	−9.5	2.0	1.0	2.2	0.06
ELCH	291.1123	−39.2906	−3.4	1.9	2.5	2.1	0.02
EPUY	288.5956	−42.1405	−7.6	2.0	0.5	2.2	0.10
FTRN	287.6233	−40.1304	−0.3	2.0	8.6	2.1	0.10
GUAB	285.9728	−41.8063	16.2	2.0	9.2	2.2	0.15
LAAM	289.9449	−38.8360	−1.1	1.9	−6.0	2.1	0.04
LINC	287.5962	−40.6233	−8.2	2.2	−2.2	2.2	0.08
PAST	288.5272	−39.5835	−3.4	2.0	−0.4	2.1	0.08
PEHO	288.9261	−38.5967	−3.0	1.9	−5.0	2.1	0.06
PPUY	288.0646	−40.7007	0.3	2.0	2.2	2.2	0.10
PSAA	286.5942	−38.7788	19.5	2.0	8.1	2.1	0.10
PTMT	287.0523	−41.4628	−0.6	1.9	4.8	2.2	0.14
PUAW	287.6075	−38.3383	2.9	2.1	2.3	2.1	0.05
PUCA	286.2800	−40.5468	27.6	2.0	8.5	2.2	0.13
RALU	287.6879	−41.3785	0.6	2.0	3.3	2.2	0.12

Table 4.1: *GPS site velocities from the SAGA network used in the modeling (Klotz et al., 2001; Khazaradze and Klotz, 2003).*

the deformation field (Khazaradze et al., 2002; Hu et al., 2004). However, the model details might not be resolved by the available data.

- Sensitivity studies for the parameters involved in the modeling have been seldom conducted.

- Trade-off between different parameters has been discussed briefly in earlier works (Hu et al., 2004), but no further testing has been carried out so far.

With this factors in mind, we performed an inversion on four source and medium parameters for the Valdivia earthquake and the area where it took place: the average coseismic slip on the rupture surface U_0, the viscosity of the underlying viscoelastic half-space η, the thickness of the overlying elastic layer D and the seismic coupling coefficient χ (Scholz and Campos, 1995). Fig. 4.2 shows a schematic representation of the fault geometry and the medium used in the modeling. We model the deformations using an elastic layer over a viscoelastic half-space with linear Maxwell rheology. This rheological model is a reasonable simplification that nevertheless represents the properties of the crust and upper mantle appropriately. Such a medium has been widely used in earlier publications (Cohen, 1980b,a; Rundle, 1982; Cohen, 1994; Fernández et al., 1996b;

Yu et al., 1996b), although systematic studies of the effects of the rheological input parameters on crustal deformation, similar to the one shown in Chapter 3, are sparse. Table 4.2 compiles the rock parameters used in our models to describe the medium. These are standard values for the crust and upper mantle, consistent with seismic refraction studies for this area (Bohm et al., 2002; Lüth et al., 2003).

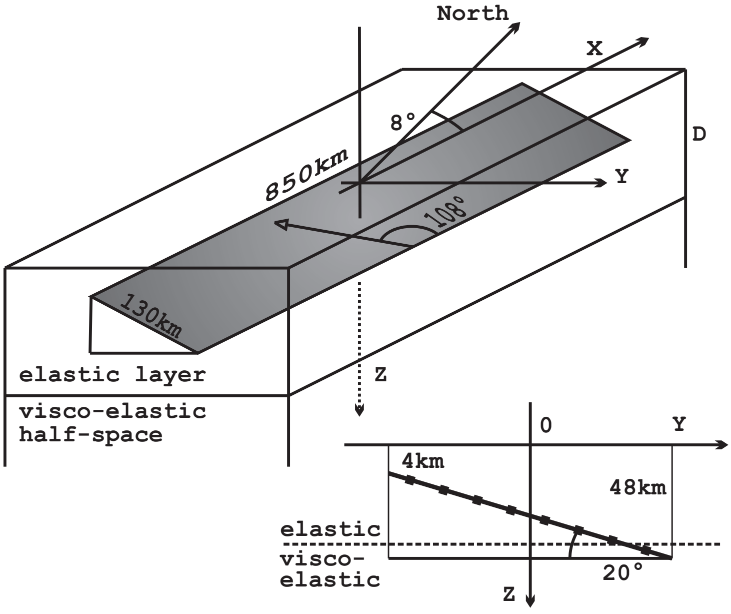

Figure 4.2: *Schematic representation of the fault geometry and medium used in the modeling. On the vertical section, the points on the rupture surface represent the point sources into which the extended surface is discretized (see Chapter 2).*

depth [km]	ρ [10^3 kg/m^3]	V_p [km/s]	V_s [km/s]	$\lambda = \mu$ [10^{10} Pa]	visc. [Pa $\cdot$ s]
$0 - D$	2.9	6.7	3.87	4.34	–
$D - \infty$	3.4	8.0	4.62	7.25	η

Table 4.2: *Medium model parameters used. The elastic layer extended from 0 km to a depth D, varying from 30 to 98 km. The viscosity of the underlying half-space, η, varied from 10^{18} Pa·s to $8.0 \cdot 10^{22}$ Pa·s.*

Other authors have considered different rheological models to analyze post-seismic relaxation processes, like the Standard Linear Solid rheology (Cohen, 1982; Pollitz et al., 1998) or power-law, non-linear rheologies (Pollitz et al., 2001; Freed and Bürgmann, 2004). These approaches are adequate to model the transient creep immediately after an earthquake. On the other side, linear Maxwell rheology is adequate when the steady-state has been reached. Given the time interval between the Valdivia event and the observations ($\sim$ 35a) and the estimated average repeat time (128 ± 31a Nishenko, 1985), we can assume that the steady-state has been reached and that the Maxwell linear rheology properly reproduces the relaxation process. In addition, the limited amount of data justifies the use the linear Maxwell rheology instead of more complicated models.

For the inversion, we performed a parameter-space grid search on the four parameters of interest. Besides their most likely values, we also obtained information about the sensitivity of the modeled data to each parameter. Also, we studied the different kinds of processes that (may) contribute to the observed deformation, in order to determine whether it is possible to distinguish their effects on the measurements and therefore to establish the cause for the anomalous velocities around the Valdivia earthquake area.

The slip on the fault plane was assumed to be uniform. It may be more realistic to divide the whole rupture surface into patches with different average slip (Linde and Silver, 1989; Barrientos and Ward, 1990), but we opted not to do so, since the small amount of data available and the distance from the rupture surface to the stations does not allow for such detailed slip inversion. Also, slip along the rupture surface should tend to zero towards the edges of the fault. Hence, it would be correct to include tapering of the slip on the rupture surface. However, the effects of such a tapering are only perceptible close to the rupture edges. The stations closest to the fault plane are directly above its deeper edge, so that their distance from to the rupture edges is over 40 km. The tapering in the slip distribution would not have any visible effect on the observation point.

The size and orientation of the fault plane was also fixed, in order to avoid making our analysis too extensive. The rupture surface had an area of 850×130 km^2, dipping 20^o E. These values are consistent with recent studies (Oleskevich et al., 1999; Bohm et al., 2002; Krawczyk and the SPOC team, 2003) and similar to those considered or derived by other authors (Plafker, 1972; Kanamori and Cipar, 1974; Cifuentes and Silver, 1989; Barrientos and Ward, 1990). For a subduction zone, it would be realistic to increase the value of the dip angle with depth in the seismogenic zone (Linde and Silver, 1989; Barrientos et al., 1992), but, on the other hand, the dip angle is a geometrical variable that mainly affects the distribution of the deformation and less its development in time (see Chapter 3), i.e., the post-seismic velocity. Thus, we use a planar rupture area for simplicity. The rake angle was fixed to 108^o to coincide with the long-term direction of relative motion between the Nazca and South American plates, projected onto the rupture surface (Chase, 1978; DeMets et al., 1990, 1994; Norabuena et al., 1998; Angermann et al., 1999; Norabuena et al., 1999). The strike of the rupture surface and the depth of the upper limit of the fault plane were chosen in our model to coincide with the local trend of the Peru-Chile trench (N8^oE) and its local depth (4 km) (Smith and Sandwell, 1997).

The observed velocities could in principle include deformation proceeding from different processes in addition to plate motion: post-seismic relaxation, silent slip on the coseismic rupture surface or aseismic slip on its down-dip prolongation. Several attempts incorporating deep slip did not lead to a better fit of the data, hence the total observed deformation was modeled as follows:

$$\mathbf{x} = \chi \, \mathbf{x}_{plate}(D) + \mathbf{x}_{relax}(U_0, \eta, D) + (1-\chi) \, \mathbf{x}_{ss}(D), \tag{4.1}$$

where $\mathbf{x}$ is the total modeled deformation, $\mathbf{x}_{plate}$ is the deformation caused by plate convergence, $\mathbf{x}_{relax}$ is the contribution from post-seismic relaxation and $\mathbf{x}_{ss}$ is the deformation created by silent slip. The seismic coupling coefficient regulates which percentage of plate convergence is stored on the fault and later released by earthquakes. Here, we assume that the rest of the convergence gets released in the form of silent slip. The steady nature of $\mathbf{x}_{plate}$ and $\mathbf{x}_{ss}$ allows to model them elastically, so that they do not depend on the viscosity. Also, these contributions to the total deformation are exclusively determined by the plate convergence and the medium parameters, so that they do not depend on U_0. Hence, $\mathbf{x}_{plate}$ and $\mathbf{x}_{ss}$ depends only on D. On the contrary,

$\mathbf{x}_{relax}$ depends on the manner in which both medium and event are modeled, so that it is dependent on U_0, η and D. It must be noted that the three contributions to the total deformation are time dependent. $\mathbf{x}_{plate}$ and $\mathbf{x}_{ss}$ increase linearly with time and the time evolution of $\mathbf{x}_{relax}$ is determined by the choice of the rheological model and the value of the viscosity.

Models with viscosity values covering several orders of magnitude, from 10^{18} Pa·s to $8.0 \cdot 10^{22}$ Pa·s, were considered. All models have a Maxwell rheology for the half-space below the seismogenic layer. The reason for this wide range is that viscosity is not well known, with some studies showing that traditional standard values used in simulations may be incorrect by up to one order of magnitude (Vermeersen et al., 1998). Previous inferences for this parameter in the area of the Valdivia earthquake range from $3 \cdot 10^{19}$ Pa·s (Khazaradze et al., 2002; Hu et al., 2004) to several times 10^{20} Pa·s (Piersanti, 1999). In addition, the average viscosity of the mantle has been estimated to be 10^{21} Pa·s from post-glacial rebound (James et al., 2000) and rotational dynamic studies (Lambeck, 1980).

For each viscosity value, the thickness of the elastic layer was varied between 30 km to 98 km. Tichelaar and Ruff (1991) estimated the depth of seismic coupling in Chile to be 48-53 km, while Oleskevich et al. (1999) proposed 40-50 km. Recent seismic refraction studies propose a crustal thickness of at least 35 km at $\sim 38.15^o$ S (Bohm et al., 2002; Krawczyk and the SPOC team, 2003). However, some modeling approaches by other authors considered a much thicker elastic layer (Piersanti, 1999).

It must be noted at this point that we are limited to modeling homogeneous horizontal layers. Hence, the thickness of the elastic layer may not be directly interpreted as the thickness of the crust in the area where the earthquake occurred. The latter shows strong lateral variations, especially in the trench-perpendicular direction. Rather, our elastic layer thickness reflects the depth range where both oceanic and continental plates are coupled and where the material behaves elastic/brittle, so that seismicity can occur.

We considered a range of different values for the average slip on the rupture surface, between 10 to 45 m. Different authors consider different values for this parameter, ranging from 17 m (Barrientos and Ward, 1990) to 40 m (Plafker and Savage, 1970). With the rupture surface and medium rock parameters of our model, a coseismic average slip of at least 40 m is required to fit the moment magnitude, hence the high upper limit for the values that we regard as possible.

No specific study has been done for the state of coupling of the Chilean Subduction Zone at the latitudes in this work. It is clear that this subduction zone, with young lithosphere subducting rapidly, must be strongly coupled and has a highly compressive strain regime (Uyeda, 1982; Scholz and Campos, 1995; Klotz et al., 2001; Conrad et al., 2004). Therefore, the seismic coupling coefficient (reflecting the degree of mechanical coupling at the plate interface) for this subduction zone must be close to 1. We consider a number of different values for the seismic coupling coefficient, ranging from 1, meaning totally locked (Klotz et al., 2001), down to 0.65. Lower values are not reasonable.

Altogether, a total number of 1,224,720 different models were considered.

To evaluate the fit between the models and the data, we calculated the deviation as follows:

$$\Delta = \sum_{i=1}^{22} \left[\left(\frac{x_i - x_i^{GPS}}{\sigma_{x_i}} \right)^2 + \left(\frac{y_i - y_i^{GPS}}{\sigma_{y_i}} \right)^2 \right], \tag{4.2}$$

where $\left(x_i^{GPS}, y_i^{GPS}\right)$ are the measured displacement at the i-th station in the South-North and West-East direction, respectively, $(\sigma_{x_i}, \sigma_{y_i})$ are the corresponding error estimations and (x_i, y_i) are the respective modeled displacement values.

4.4 Results and discussion

4.4.1 Parameter inversion

From the grid search we found that the best-fitting model has an elastic layer $D = 46$ km overlying a viscoelastic half-space with a viscosity of $\eta = 10^{20}$ Pa·s, an average slip of $U_0 = 15$ m and a seismic coupling coefficient of $\chi = 0.96$. This set of parameters is represented by small white circles in Figs. 4.3 and 4.4.

The soundness of these inversion results was tested by means of a Monte-Carlo error propagation analysis (Metropolis and Ulam, 1949). This is a statistically robust approach to evaluate the stability of the parameters' estimation by reiterating the inversion for sets of potential deformation rates at the GPS sites, taking into account the uncertainties in the velocity values. We considered 2 times 550 random sets of velocities falling into the 1σ and 2σ GPS error ellipses. They led to the values respectively shown by crosses and dots in Figs. 4.3 and 4.4. The results must not be mistaken with the analysis of the deviation curves. The latter only provides a qualitative estimation of the dependence of the deviation on the considered parameter and cannot be used to extract a confidence interval. The Monte Carlo method offers alternative possible best-fitting models when inaccuracies in the data are considered. It propagates the confidence ellipses in the GPS measurements to the determination of the minimum deviation and therefore to the estimation of the most likely value for the parameters.

The displacements calculated by means of the best-fitting model are shown in Fig. 4.1 by thick-line vectors. The average difference between model velocities and GPS observations is 6 mm/a, comparable to the 3σ errors of the GPS velocities. If we only consider the stations south of latitude 38^o S, the differences are reduced to 4 mm/a, the same value obtained by Hu et al. (2004) by means of their finite element modeling.

Fig. 4.3 shows the dependence of the deviation between observations and predictions on the variation of each parameter. The upper panel shows the effect of the elastic layer thickness. For low values in this variable, a moderate variation leads to sharp and strong variations in the deviation. The origin of this is the discretisation of the extended source into a finite number of point sources (see Chapter 2). The change in the depth for the elastic to viscoelastic boundary implies a change in the medium properties for a number of point sources (see Fig. 4.2), hence the deviation changes abruptly rather than continuously. The depths of the deepest point sources are shown as vertical dashed lines to illustrate this problem. The obtained result of $D \leq 46 - 48$ km may be interpreted as the thickness of the continental crust under the GPS sites, consistent with value derived from seismic refraction data (Bohm et al., 2002; Krawczyk

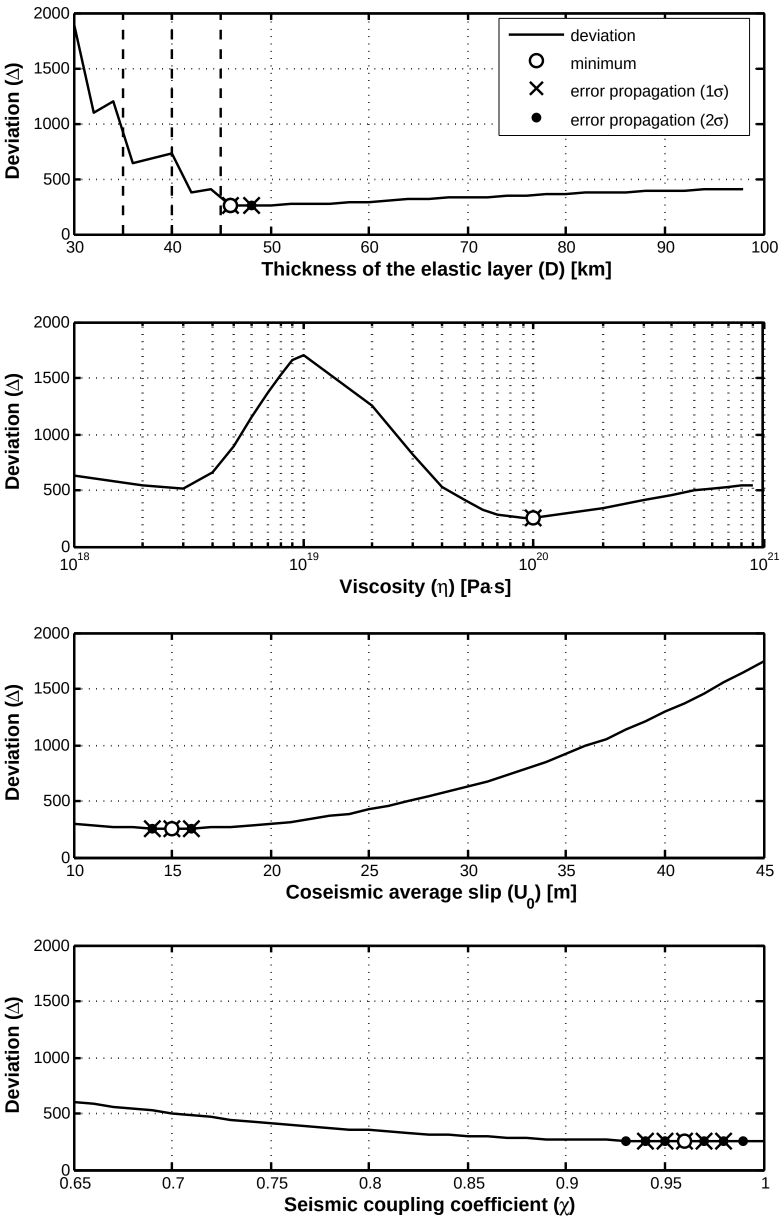

Figure 4.3: *Dependence of the deviation (Δ, Eq. 4.2) against each parameter. From top to bottom: elastic layer thickness (D), viscosity (η), coseismic average slip on the rupture surface (U_0) and seismic coupling coefficient (χ). For each panel, the three variables that are not considered were fixed to the values that led to the best-fitting model (see Table 4.3). Vertical dashed lines on the upper panel display the depth of the deepest point sources into which the rupture surface was discretized. The white circle in each panel shows the position of the minimum, crosses and dots respectively display values for models resulting from the 1σ and 2σ error propagation analysis.*

and the SPOC team, 2003). This result is also consistent with the depth of coupling between the Nazca and the South American plates, as inferred from the distribution of interplate seismicity (Tichelaar and Ruff, 1991).

The value of $\eta = 10^{20}$ Pa·s for the viscosity led to the best fit of the data (second panel, Fig. 4.3). This result agrees with previous works for this region (Piersanti, 1999) and also with other studies dealing with the viscosity of the upper mantle (Vermeersen et al., 1998). Our result is very well constrained according to the Monte-Carlo analysis. The local minimum for $\eta = 3 \cdot 10^{18}$ Pa·s corresponds to a viscosity which is usually considered too low.

A best estimate of the coseismic slip $U_0 = 14-16$ m (third panel, Fig. 4.3) is similar to the one deduced by Barrientos and Ward (1990) for their uniform slip planar model, but much smaller than the patches of high displacement of their variable slip model.

Other works consider or derive comparable values for this parameter (Khazaradze et al., 2002), although some authors suggest the possibility of a much larger average slip (Plafker and Savage, 1970). We discuss this possibility in section 4.4.2.

The best-fitting model had a seismic coupling coefficient of $\chi = 0.94 - 0.98$ (fourth panel, Fig. 4.3), meaning that the Chilean subduction zone is 94 - 98% locked. This is a reasonable result, being that the Chilean subduction zone is an area with a highly compressive strain regime (Scholz and Campos, 1995; Klotz et al., 2001; Conrad et al., 2004).

According to the error propagation analysis, these parameter estimates are stable and reliable when considered independently. Especially, the value for the viscosity in this area remains unchanged for sets of GPS velocities randomly distributed inside their 2σ error ellipses. The seismic coupling coefficient, on the other hand, is less well resolved. Given the uncertainty in the determination of this parameter, we can only conclude that the data is consistent with a highly locked fault.

We performed two further inversions from models under two special restrictions: first, the subduction zone was set to be fully locked ($\chi = 1$), such that viscoelastic relaxation and inter-seismic elastic strain were the only processes causing deformation. Second, models with no post-seismic relaxation processes were considered. The results from these inversions are summarized in Table 4.3, together with the results when all deformation types were present. The results show that including post-seismic relaxation improves the fit to the observed GPS data. If we assume that post-seismic relaxation is not taking place, or that its influence cannot be observed on the measured deformation, the deviation between modeled and observed data is 87% larger. On the other hand, excluding silent slip also leads to a good fit between modeled and observed data. This is an anticipated result, since the inversion for the general case already suggested that the subduction zone is almost completely locked.

Finally, we also carried out an inversion using the convergence rate of 78 mm/a provided by paleo-magnetic studies instead of the 66 mm/a from geodetic studies. The results from the inversion do not change, with the exception of the value for the seismic coupling coefficient (see Table 4.3). Increasing the convergence rate implies that the inter-seismic deformation caused by plate convergence is larger. As a consequence, in order to maintain the goodness of the fit, the contribution of plate motion to the total deformation must be reduced, hence the seismic coupling coefficient must be smaller (see Eq. 4.1).

4.4.2 Trade-off

Fig. 4.4 shows the trade-off between pairs of studied parameters. For each panel, the two variables that are not considered were fixed to the value that led to the best-fitting model (see Fig. 4.3 and Table 4.3). To facilitate the analysis, the field displayed is $\Delta' = 30 \cdot ln(\Delta/\Delta_{min})$. Also, the results from the 1σ and 2σ error propagation analysis are shown.

No clear trade-off between pairs of variables is observed, with the exception of viscosity and coseismic average slip. In this case, models with $\eta = 2 \cdot 10^{20}$ Pa·s and $U_0 = 26 - 31$ m, as well as models with $\eta = 3 \cdot 10^{20}$ Pa·s and $U_0 = 41 - 45$ m also provide a good fit to the GPS data. A linear regression of the viscosity on the average

Contributions to deformation	Parameters				dev. from obs. GPS data (Δ)
	elas. layer thickness (D) [km]	half-space viscosity (η) [Pa·s]	average slip (U_0) [m]	seismic c. coeff. (χ)	
$\mathbf{x}_{plate}$, $\mathbf{x}_{relax}$, $\mathbf{x}_{ss}$	46	1.0×10^{20}	15	0.96	255.0109
$\mathbf{x}_{plate}$, $\mathbf{x}_{relax}$	82	9.0×10^{18}	13	(1.0)	278.3046
$\mathbf{x}_{plate}$, $\mathbf{x}_{ss}$	46	–	–	0.72	476.5012
$\mathbf{x}_{plate}$, $\mathbf{x}_{relax}$, $\mathbf{x}_{ss}$ (NUVEL-1A)	46	1.0×10^{20}	15	0.89	255.0987

Table 4.3: *Parameter values corresponding to the best-fitting models for four different assumptions about the origin of the deformation. First, the observed velocities is fitted by deformation from plate motion, post-seismic viscoelastic relaxation and silent slip on the rupture surface. Second, the seismic coupling coefficient is fixed to $\chi = 1$, meaning that no silent slip takes place. Third, we assume that no relaxation process exists, or that its effect cannot be observed from the measured velocities. Finally, we consider the Nazca-South America convergence rate from paleo-magnetic studies (DeMets et al., 1994).*

coseismic slip produces the following relationship:

$$\begin{aligned} \eta &= aU_0 + b \\ a &= 7.27 \cdot 10^{18} \text{ Pa·s/m} \\ b &= -3.86 \cdot 10^{18} \text{ Pa·s.} \end{aligned} \tag{4.3}$$

According to this, values larger than the 15 m are possible in combination with viscosities larger than 10^{20} Pa·s. 15 m of average rupture slip corresponds to a moment $M_0 = 7.2 \cdot 10^{22}$ N·m and therefore a magnitude $M_w = 9.2$ using the Kanamori relationship, much lower than the actual $M_w = 9.5$. Consistency with the latter value would imply a seismic moment of $M_0 = 2.24 \cdot 10^{23}$ N·m, and therefore an average coseismic slip of $U_0 = 40$ m, which conflicts with recurrence time and convergence rate data (Nishenko, 1985; DeMets et al., 1994; Somoza, 1998). There are two possible explanations for this problem. First, this may be an indication that the distribution of slip on the rupture surface should be modeled non-uniformly. To check this, a better areal coverage could be very useful when inverting for the distribution of slip. The second possibility is that the average slip on the rupture surface is larger than the 15 m obtained in this study, implying a larger viscosity. Data from a later campaign will be useful in gaining a better insight into the time-development of the relaxation process, so that higher viscosity values could be confirmed or ruled out.

4.4.3 Horizontal velocity components

Fig. 4.5 shows the horizontal velocities along the W-E (left panels) and S-N (right panels) directions for three latitude intervals. The dots are the observed deformation

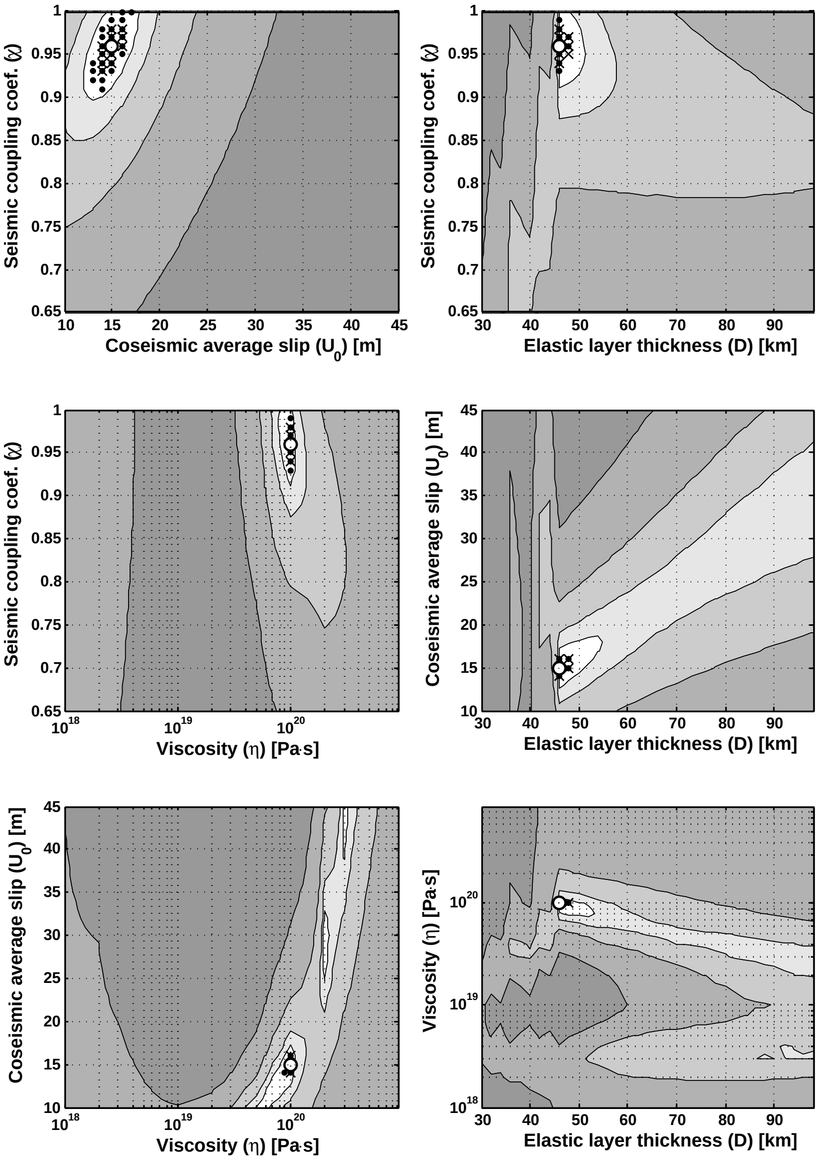

Figure 4.4: *Trade-off between pairs of the studied parameters. For each panel, the two variables that are not considered were fixed to the values that led to the best-fitting model (see Fig. 4.3 and Table 4.3). The field displayed is $\Delta' = 30 \cdot ln(\Delta/\Delta_{min})$, where Δ is the deviation between the modeled and observer velocities. The white circles show the position of the minimum, crosses and dots, respectively, display parameter values for models resulting from the 1σ and 2σ error propagation analysis. Isolines display contours for Δ' equal to 1, 3, 10 and 30.*

data for the stations corresponding to each interval, together with 1σ error bars. The solid thick line shows the W-E and S-N velocities for the best-fitting model for a trace of points at the central latitude of each interval (38^o S, 40^o S and 42^o S, respectively, see also Fig. 4.1). For the W-E velocities, the fit is in general good, with our best-fitting model reproducing the trend shown by the GPS velocities. In the case of the S-N velocities, the best fit occurs at the two southernmost profiles, although it must

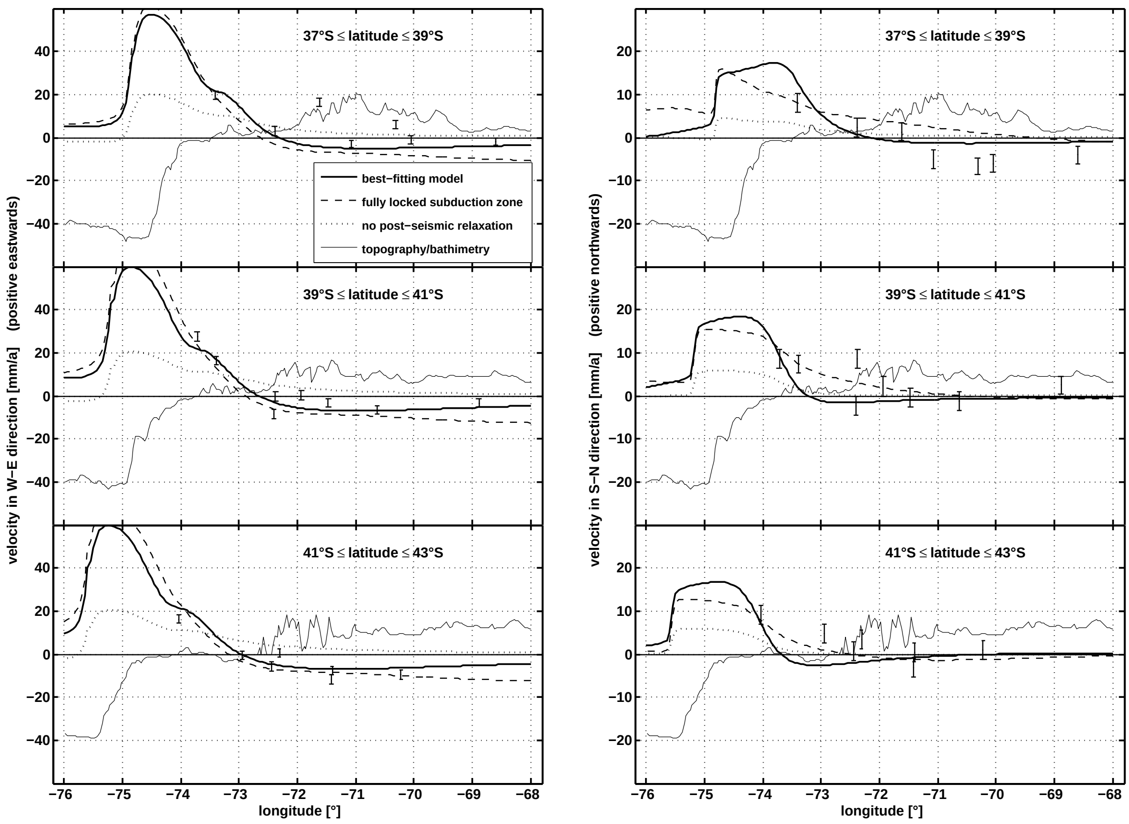

Figure 4.5: *Horizontal velocity components in the W-E (left) and S-N (right) directions for three latitude intervals (areas A, B and C, Fig. 4.1). Dots and error bars represent measured GPS velocities together with 1σ errors. The solid thick line shows W-E and S-N velocities from the best-fitting model for a trace of points at the central latitude of each interval (*38^o *S,* 40^o *S and* 42^o *S respectively). The dotted line shows the deformation when the subduction zone is fully locked (*$\chi = 1$*), so that viscoelastic relaxation and plate convergence are the only processes causing deformation. The dashed line shows the deformation when no post-seismic relaxation process is considered. Table 4.3 lists the parameters that lead to the best fit for each one of these cases.*

be noted that the magnitude of the displacement in the S-N direction is much smaller than the one in the perpendicular direction. This variation of the fit with latitude may also be a suggestion that uniform coseismic slip on the rupture surface is not adequate to describe the Valdivia event.

The dotted lines in Fig. 4.5 show the best-fitting model without the contribution from relaxation (plate convergence and silent slip only). This model creates a too-smooth deformation field and fails to fit most of the observed data, especially in the area close to the rupture surface. In addition, and most importantly, the anomalous seaward velocities are not reproduced when excluding relaxation. Hence, even though some silent slip seems to be taking place in this area, this process alone cannot explain the observed seaward velocities. Including viscoelastic post-seismic relaxation processes, on the other hand, improves significantly the fit of the data, while the anomalous velocities are well reproduced. This can only be understood as evidence for the relaxation process of the Valdivia earthquake continuing.

When we regard viscoelastic relaxation processes as source for the deformation, but exclude silent slip (dashed lines on Fig. 4.5), the fit between modeled and observed data is also good (see also Table 4.3), and the results are very similar to the ones obtained in the general case, with no systematic variation in the fit to the single stations.

4.4.4 Measurability and time-dependency of the deformation rates

The viscosity of $\eta = 10^{20}$ Pa·s obtained for the best-fitting model and the used shear modulus of $\mu = 7.25 \cdot 10^{10}$ Pa for the half-space imply a Maxwell relaxation time of $\tau_\alpha = \eta/\mu \approx 44$ a for the viscoelastic mantle. This value represents the time required for the stress to relax by a factor of $1/e$ in a homogeneous linear Maxwell body subjected to a constant strain. Because of the layering of the model and the spatial transfer of stresses, the Maxwell relaxation time does not necessarily represent the actual characteristic decay time of the post-seismic crustal motion. As a consequence, the latter is in general dependent on the observable and on the observation location.

As it can be important for future GPS campaigns to know for how long will the deformation associated with the Valdivia earthquake still be measurable and where are the locations of strongest time-dependence, we did the following analysis: Assuming 4 mm/a as a reasonable measurability threshold, the contour lines on Fig. 4.6 display the number of years after the event for which the horizontal velocities from post-seismic relaxation will still be identifiable, that is, for which the velocities will be above the threshold value of 4 mm/a. According to our results, the on-going deformation from the relaxation process of the Valdivia earthquake will be measurable for several centuries at most of the sites employed in this study. The coastal stations will be the first ones to display no effect from the relaxation process.

Fig. 4.7 shows the W-E deformation rate for a trace of points at 40^o S for the best-fitting model, both before the earthquake and the additional contribution of the event at different moments after the Valdivia earthquake. From Fig. 4.6 and 4.7 it follows that stations in the range between 70 to 73^o W will be the most adequate to further analyze the relaxation process, since the time-dependence of the deformation rate is strong in this region, and its effects will be still measurable for a long period of time.

It is worthwhile to note that we made inferences about the time-dependent relaxation process from only two GPS campaigns. The two measurements provide only one point in time for the deformation, so the time evolution of the velocity field has not been observed directly. It is the areal coverage of the GPS stations that allows us to extract information about this process.

4.5 Conclusions

By means of dislocation models we reproduced the first-order pattern of measured deformation observed in the area of the 1960 Valdivia event. According to our study, the Valdivia earthquake is the most likely explanation for the velocity component that cannot be explained by plate convergence. We derived the most likely values for the viscosity (η), the thickness of the elastic layer (D) and the seismic coupling coefficient

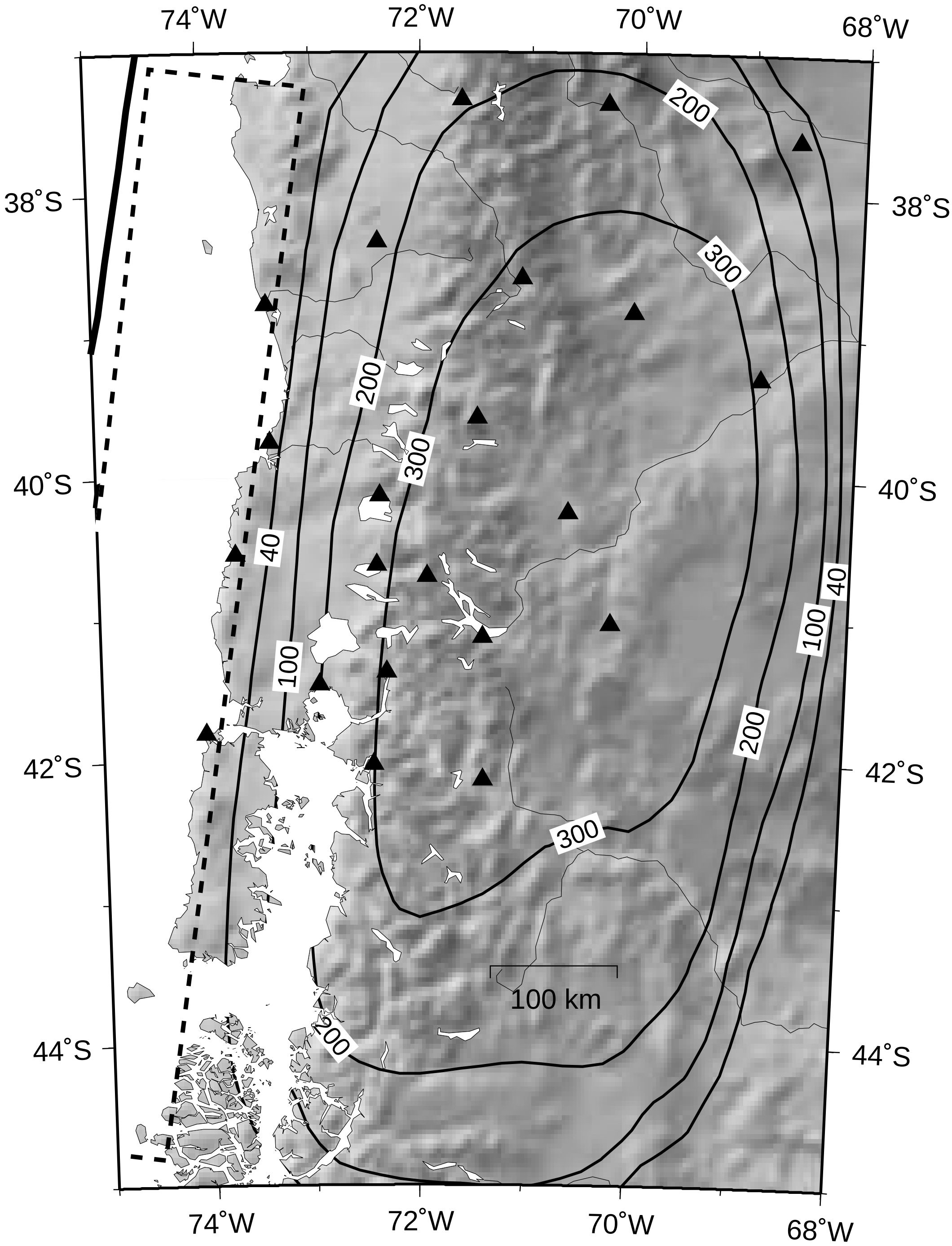

Figure 4.6: *Isochrones for the measurability of the deformation caused by post-seismic relaxation. The label for the contours display the number of years after the event during which the post-seismic relaxation produce velocities of at least 4 mm/a. The deformation was calculated by means of our best-fitting model.*

(χ) for this area, as well as the average coseismic slip on the 1960 rupture surface (U_0). Despite the simplicity of our approach and the uncertainties in several input values, our inversion was successful in retrieving the main features of the observations. The lack of precise geophysical information for the studied area does not allow us to propose

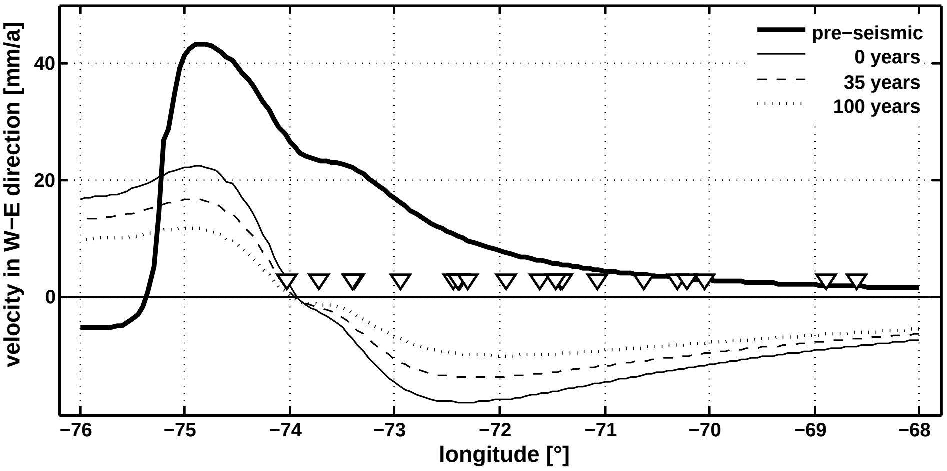

Figure 4.7: *Horizontal velocities in the W-E direction for a trace of points at* 40^o *S. Calculations made with the values for the parameters corresponding to the best fit of the data (Table 4.3, first line). The thick solid line represents the pre-seismic deformation, that is, the effects from plate convergence and silent slip. Thin lines display the additional contribution associated with the Valdivia earthquake at different points in time. Triangles display the position of the stations considered in this study.*

more complex models, with a more detailed geometry and heterogeneous slip distribution for the rupture surface. Also, the amount of data we used was very limited, so the possibility of an inversion on other parameters apart from those studied was not considered. Nevertheless, our best-fitting model reproduces the general trend of the observed velocities, including the observed anomalous seaward movement of the inland stations. Other authors proposed silent slip as a possible explanation for the measured anomalous deformation rates. Our study shows that, even though a small amount of silent slip is present, it is not sufficient to explain the observed seaward velocities on its own. The most likely explanation for these anomalies is the post-seismic relaxation associated with the Valdivia earthquake. Estimates of the values of the studied parameters are consistent with previous works, although our study provides a narrower range of possible values. Specifically, according to our error propagation analysis, the estimate for the viscosity in this area ($\eta = 10^{20}$ Pa·s) is stable and reliable when considered independent from the other parameters. However, we found a trade off between viscosity and average coseismic slip on the rupture surface, hence higher viscosities, in combination with larger coseismic slip values, must also be regarded as possible. According to the values inferred, the relaxation process will still be measurable for several decades, with decreasing deformation magnitude. New measurement campaigns could be used to extract more information about the medium and the Valdivia earthquake. A larger areal coverage would allow a better analyze of the distribution of slip on the rupture surface, the most problematic point in our study. Also, measurements at the same sites at later times would be used to better understand the time-development of the relaxation process. The speed of this process is directly linked to the viscosity value in the region. The values presented in this work provide a good first-order approximation and starting point for more detailed works.

Chapter 5

Elastic and inelastic triggering of earthquakes in the North Anatolian Fault zone

Deformation models used to explain the triggering mechanism often assume pure elastic behavior for the crust and upper mantle. In reality however, the mantle and possibly the lower crust behave viscoelasticaly, particularly over longer time scales. Consequently, the stress field of an earthquake is in general time dependent. In addition, if the elastic stress increase were enough to trigger a later earthquake, this triggered event should occur instantaneously and not many years after the triggering event. Hence, it is appropriate to include inelastic behavior when analyzing stress transfer and earthquake interaction.

In this work, we analyze a sequence of 10 magnitude $M_s > 6.5$ events along the North Anatolian Fault between 1939 and 1999 to study the evolution of the regional Coulomb stress field. We investigate the triggering of these events by stress transfer, taking viscoelastic relaxation into account. We evaluate the contribution of elastic stress changes, of post-seismic viscoelastic relaxation in the lower crust and mantle, and of steady tectonic loading to the total Coulomb stress field. We analyze the evolution of stress in the region under study, as well as on the rupture surfaces of the considered events and their epicenters. We study the state of the Coulomb stress field before the 1999 Izmit and Düzce earthquakes, as well as in the Marmara Sea region.

In general, the Coulomb stress failure criterion offers a plausible explanation for the location of these events. However, we show that using a purely elastic model disregards an important part of the actual stress increase/decrease. In several cases, post-seismic relaxation effects are important and greater in magnitude than the stress changes due to steady tectonic loading. Consequently, viscoelastic relaxation should be considered in any study dealing with Coulomb stress changes.

According to our study, and assuming that an important part of the rupture surface must be stressed for an earthquake to occur, the most likely value for the viscosity of the lower crust or mantle in this region is $5 \cdot 10^{17} - 10^{18}$ Pa·s. Our results cannot rule out the possibility of other time-dependent processes involved in the triggering of the 1999 Düzce event. However, the stress increase due to viscoelastic relaxation brought 22% of the 1999 Düzce rupture area over the threshold value of $\Delta\sigma \geq 0.01$ MPa (0.1 bar), and took the whole surface closer to failure by an average of 0.2 MPa. Finally, we argue that the Marmara Sea region is currently being loaded with positive Coulomb stresses at a much faster rate than would arise exclusively from steady tectonic loading on the North Anatolian Fault.

5.1 Introduction

The North Anatolian Fault zone (NAF) is an almost pure dextral 1500 km long fault zone running along the north of Turkey (Fig. 5.1). During the last century, several strong earthquakes have taken place along the NAF. These events or subsets of them have been the subject of numerous studies (Mogi, 1968; Toksöz et al., 1979; Purcaru and Berckhemer, 1982; Roth, 1988; Stein et al., 1997). There are several reasons for the interest: first, the events provide an unequalled possibility to analyze how the occurrence of an earthquake may trigger additional shocks. Second, the number of field investigations provides a valuable and still increasing amount of information. Third, recent events appear to be propagating westwards, with the $M_w = 7.4$ Izmit and the $M_w = 7.1$ Düzce earthquakes in 1999 as the most recent and westernmost events. If this sense of propagation continues, a strong shock west of the Izmit-Düzce rupture can be expected (Hubert-Ferrari et al., 2000; Parsons et al., 2000; Parsons, 2004). This region would be the Marmara Sea, just south of Istanbul, a mega-city with more than 12 million inhabitants. A strong earthquake in this region would therefore have catastrophic consequences, both in loss of life and monetary costs.

The triggering of earthquakes by stress transfer has been analyzed by numerous authors (Healy et al., 1968; Raleigh et al., 1972; Harris, 1998; Belardinelli et al., 1999; King and Cocco, 2001; Belardinelli et al., 2003; Hardebeck, 2004; Freed, 2005; Steacy et al., 2005). Previous deformation models often assume purely elastic behavior for the crust and upper mantle, and therefore the crust instantaneously responds to the motion on the rupture. When using the elastic approach, any time dependence of the deformation might be attributed to time-dependent fault slip (Kasahara, 1975; Linde and Silver, 1989; Barrientos et al., 1992). Several studies have shown good correlation between calculated positive elastic (co-seismic) stress change and the location of aftershocks (Reasenberg and Simpson, 1992; Stein et al., 1992; King et al., 1994; Nalbant et al., 1996; Toda et al., 1998; Deng et al., 1999; Ma et al., 2005; Nostro et al., 2005), as well as the triggering of moderate to large earthquakes (King et al., 1994; Stein et al., 1994; Harris et al., 1995; Stein et al., 1997; Nalbant et al., 1998; Stein, 1999; Nalbant et al., 2002; McCloskey et al., 2005; Nalbant et al., 2005a).

However, in the real Earth, the mantle and possibly the lower crust behave as an inelastic body, that is, any imposed stress will relax with time. The crust will first deform as an elastic body, but later deformation will continue because of stress relaxation (Thatcher et al., 1980). Since inelastic stress relaxation also leads to redistribution of the stress, it is necessary to include inelastic behavior when analyzing stress transfer and earthquake interaction. Also, an important limitation of the elastic/co-seismic stress change approach is that it cannot explain time delays of the triggered events. Post–seismic stress changes due to viscous relaxation in the lower crust and/or upper mantle have also been successfully used to explain aftershock distribution and the triggering of later events (Deng et al., 1999; Freed and Lin, 2001; Zeng, 2001; Pollitz and

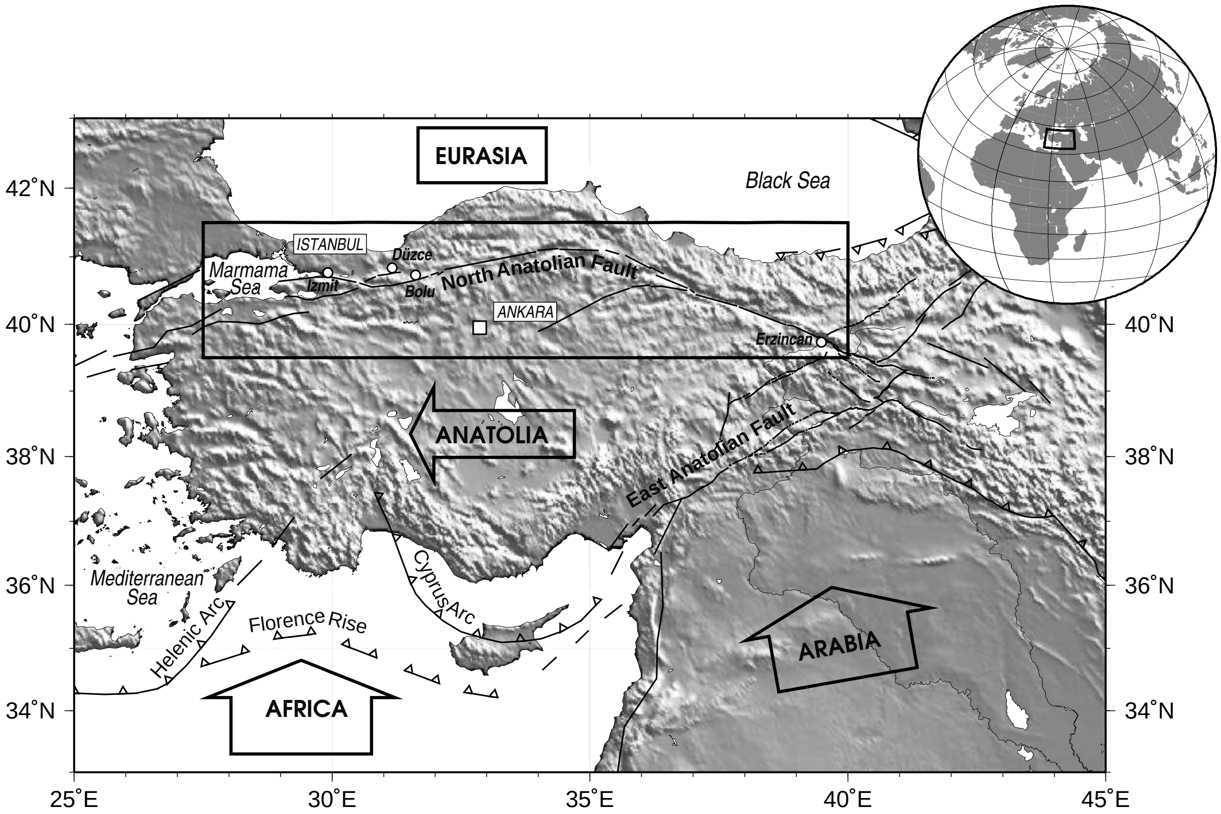
EURASIA
Black Sea
ISTANBUL
Düzce
Marmama Sea
Izmit
Bolu
North Anatolian Fault
ANKARA
Erzincan
ANATOLIA
East Anatolian Fault
Mediterranean Sea
Helenic Arc
Florence Rise
Cyprus Arc
ARABIA
AFRICA
42°N
40°N
38°N
36°N
34°N
25°E
30°E
35°E
40°E
45°E

Figure 5.1: *Map showing the major tectonic elements of Turkey. Anatolia is forced to move towards the Aegean subduction zone, moving along the North and East Anatolian faults. The box shows our study area.*

Sacks, 2002). However, only pairs of events have been considered so far to analyze whether, and how, the Coulomb stress is increased by post-seismic relaxation.

In the present study, we investigated a sequence of 10 magnitude $M_s > 6.5$ earthquakes (Table 5.1 and Fig. 5.2) that have occurred on the NAF since 1939. In contrast to Roth (1988), the geographical region considered here brackets the area from the Marmara Sea in the west to east of Erzincan. We also took into account the details in orientation and geometry of the different ruptures. In addition, further studies carried out in the last few years have allowed us to consider more realistic values than those from Roth (1988) for the medium properties and stratification, as well as for the stress build-up due to plate motion on the NAF.

The last strong events before 1939 in this region took place in the 18^{th} century (Ambraseys and Finkel, 1995; Şengör et al., 2005). We can assume therefore that the 1939 event was the first in a new seismic cycle, and that the stress field in the region has been homogenized by steady tectonic loading. Moderate events may have a locally important influence on the stress field. However, information about their location and effects is usually not accurate enough, especially for older events and/or on the center and eastern part of the NAF. Assuming 1939 as a start for the calculations and $M_s > 6.5$ as the magnitude threshold is a good compromise to consider a significantly long seismic series and information reliable enough for the correct modeling of the considered earthquakes. We studied the changes in the Coulomb stress field from the beginning of the sequence to the present day. Previous similar works (Stein et al., 1997; Çakir et al., 2003; Muller et al., 2003) considered the instantaneous response to the events and the effects of stress change due to tectonic loading from steady slip beneath the NAF. In the present study, we additionally take into account the effect of viscoelastic relaxation in the lower crust and upper mantle. We evaluated the importance of the three processes on the total stress field.

We also analyzed the time evolution of the Coulomb stress at the epicenters of the shocks, as well as the state on the rupture surfaces immediately before the earthquakes, under different assumptions. We considered the current situation in the Marmara Sea and extrapolated it to the year 2010 to evaluate the rate at which viscoelastic relaxation is increasing the stresses in the region, information that may be useful for seismic-hazard assessment in this region.

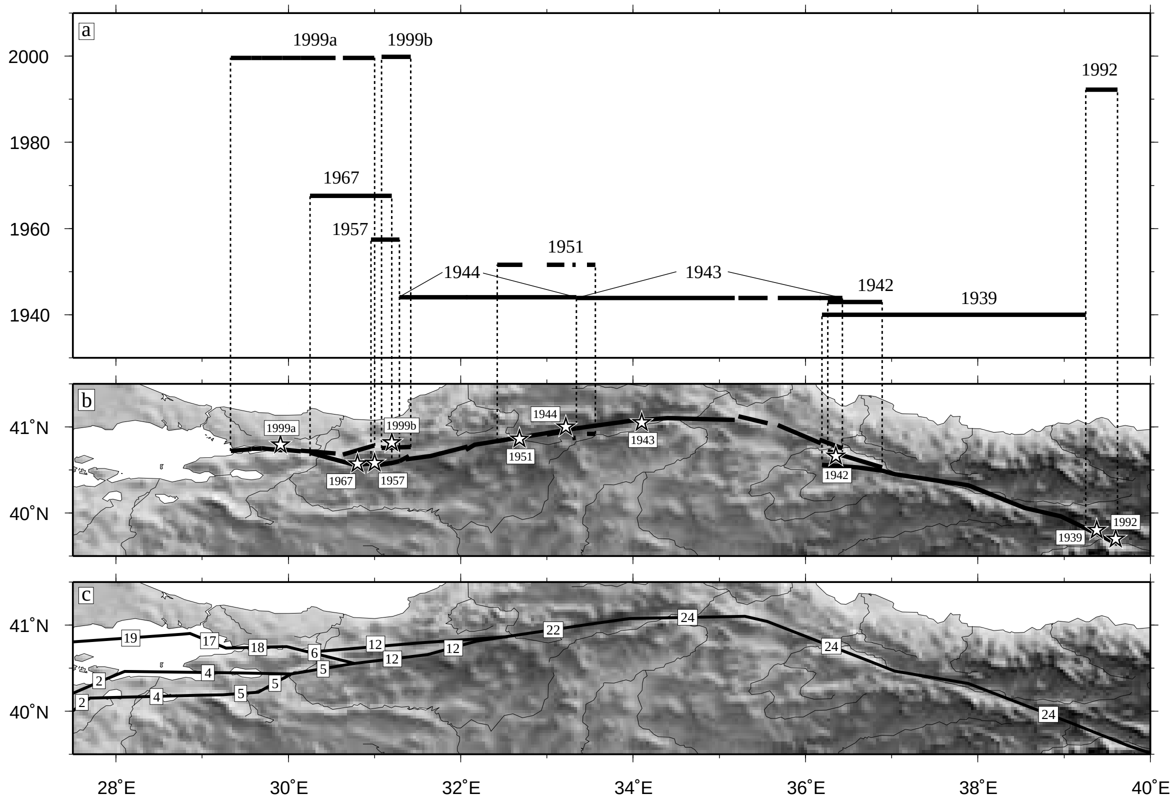

Figure 5.2: *Space-time migration of the 10 considered* $M_s > 6.5$ *earthquakes along the NAF in the period 1939 to 1999. Thick lines in (a) and (b) display the events. Stars indicate the epicenters of the shocks in the sequence (Dewey, 1976, Earthquake Research Directorate (ERD), Seismological Division, Turkey, U.S. Geological Survey (USGS)). Lines in (c) represents the geometry of the North Anatolian Fault used in the calculations. The values are the equivalent amount of slip per year on the segments in mm/a (Armijo et al., 2003; Flerit et al., 2003, 2004).*

Date			GMT	lat. [^{o} N]	lon. [^{o} E]	Ms	Mo [Nm]	references
1939	26	Dec	23:57	39.80	39.38	8.0	$4.11 \cdot 10^{20}$	3, 4, 6, 8
1942	20	Dec	14:03	40.66	36.35	7.3	$1.74 \cdot 10^{19}$	3, 4, 6, 8
1943	26	Nov	22:20	41.05	33.72	7.6	$2.51 \cdot 10^{20}$	3, 4, 6, 8
1944	01	Feb	03:23	41.00	33.22	7.6	$1.48 \cdot 10^{20}$	3, 4, 6, 8
1951	13	Aug	18:33	40.86	32.68	6.7	$2.12 \cdot 10^{19}$	1, 4, 5
1957	26	May	06:33	40.58	31.00	7.2	$1.35 \cdot 10^{19}$	3, 4, 6, 8
1967	22	Jul	16:56	40.57	30.80	7.3	$2.82 \cdot 10^{19}$	2, 3, 4, 6, 8, 14
1992	13	Mar	17:19	39.71	39.60	6.9	$1.14 \cdot 10^{19}$	6, 7, 9, 10
1999	17	Aug	00:01	40.70	29.91	7.8	$2.15 \cdot 10^{20}$	12, 13, 14
1999	12	Nov	16:57	40.818	30.198	7.3	$4.67 \cdot 10^{19}$	11, 12, 16, 17

Table 5.1: *Parameters of the sequence of earthquakes used. Epicentral coordinates are from Dewey (1976) until 1967, with the exception of the 1943 event, for which Dewey's epicentral coordinates appear to be too far East (Ambraseys, 1970; Alsan et al., 1976; Şaroğlu et al., 1992). For this event and the more recent ones, we used the coordinates provided by the Earthquake Research Directorate (ERD), Seismological Division, Turkey.* M_s *values are from the U.S. Geological Survey (USGS).* M_0 *values correspond to the geometry and slip distribution used in the present work, comparable to those of Stein et al. (1997). The references used are: 1) Pinar (1953); 2) Ambraseys and Zatopek (1969); 3) Ambraseys (1970); 4) Dewey (1976); 5) Barka and Kadinsky-Cade (1988); 6) Şaroğlu et al. (1992); 7) Pınar et al. (1994); 8) Barka (1996); 9) Nalbant et al. (1996); 10) Grosser et al. (1998); 11) Ayhan et al. (2001); 12) Tibi et al. (2001); 13) Wright et al. (2001); 14) Barka et al. (2002); 15) Muller et al. (2003); 16) Utkucu et al. (2003); and 17) Umutlu et al. (2004).*

5.2 Tectonic setting

The tectonic setting of the study region is dominated by the collision of the Arabian and African plates against the Eurasian and Anatolian ones (Fig. 5.1). The Arabian and African plates move approximately northward against the relatively stable Eurasian plate, causing the Anatolian block to move westwards from the East Anatolian Convergence Zone onto the oceanic lithosphere of the Eastern Mediterranean Sea (Şengör et al., 1985, 2005). This movement changes its direction to southwest in West Anatolia and the Aegean Sea, so that the large scale result is a counter-clockwise rotation of the Anatolian Plate (McKenzie, 1972; Jackson and McKenzie, 1988; McClusky et al., 2000). This relative westward movement of the Anatolian Plate generates strike slip on both the NAF and the East Anatolian Fault zone (EAF). Along most of the NAF, the right-lateral slip has a rate of 24 ± 1 mm/a (McClusky et al., 2000; Flerit et al., 2004).

The NAF splits into three different branches at its westernmost part. About 80% of the total slip accommodates on the northern branch and the remaining 20% is distributed between the other two (Flerit et al., 2003). The northern branch crosses the Marmara Sea, linking the Izmit segment in the east with the Ganos fault in the west (Le Pichon et al., 2001; Gokaşan et al., 2003; Armijo et al., 2005). The NAF in the Marmara Sea consists of two main parts: a western one, about 120 km long and striking N265^o E, and a 50 km long eastern segment, striking N280^o E. These two segments were the probable location of several strong and damaging historical earthquakes, the latter of which took place in 1754, 1766 and 1894 (Ambraseys and Finkel, 1991; Ambraseys, 2002; Parsons, 2004). The Marmara Sea region has also been identified as a seismic gap (Hubert-Ferrari et al., 2000).

5.3 Methodology

During the last decade, Coulomb stress modeling has become a popular and accepted tool to analyze the conditions under which earthquakes occur (King et al., 1994; Stein et al., 1997; Zeng, 2001; Muller et al., 2003; Lin and Stein, 2004). Once the components of the stress tensor have been calculated, the Coulomb stress change ($\Delta\sigma_c$) is given by:

$$\Delta\sigma_c = \Delta\tau + \mu'\Delta\sigma_N, \tag{5.1}$$

where τ is the shear stress, σ_N is the normal stress and μ' is the effective (or apparent) coefficient of friction. When Coulomb stresses surpass a certain critical value, failure occurs. Normal and shear stresses are positive when the fault is unclamped and in the corresponding slip direction respectively, so that both positive normal and shear stresses encourage failure (see Fig. 5.3, upper panels). The orientation of a known fault can be used to define the reference system to calculate normal and shear stresses. When no target fault is considered, Coulomb stresses can be calculated on so called "optimally oriented fault planes", obtaining the direction in which Coulomb stress is at its maximum (Fig. 5.3, lower panels). This approach is useful to analyze the correlation between Coulomb stress changes and aftershock distribution, since it can be assumed that a sufficient number of small faults with all orientations exist, and that the faults optimally oriented for failure will be most likely to slip in small earthquakes. The calculation of the optimum directions, however, implies knowledge of the pre-existing regional stress field (King et al., 1994).

The effective coefficient of friction is often assumed to be constant in a given area, and it is utilized to include the unknown effects of pore-fluid pressure in the crust (Harris, 1998). This parameter is not a material constant, as often implicitly assumed, and its relationship with pore pressure is not simple (Beeler et al., 2000; Cocco and Rice, 2002). A common simplification is to assume that the change in pore pressure is proportional to the normal stress. Under this assumption, μ' is related to the friction coefficient μ through the Skempton coefficient B as follows:

$$\mu' = \mu \cdot (1 - B), \tag{5.2}$$

where B describes the presence of fluids in rock, with $B = 0$ for completely drained rocks and $B = 1$ for the maximum possible presence of fluids. A coefficient of friction of $\mu = 0.85$ from laboratory values (Byerlee and Wyss, 1978) and a moderate pore pressure ($B \sim 0.5$) lead to a value of ($B \sim 0.5$). However, if fluids are expelled from the fault zone, the value for μ' will increase up to that of μ.

5.4 Model parameters

The layered model used for our calculations is described by the rock parameters summarized in Fig. 5.4 (Milkereit et al., 2000, 2004). We considered a Poisson's ration

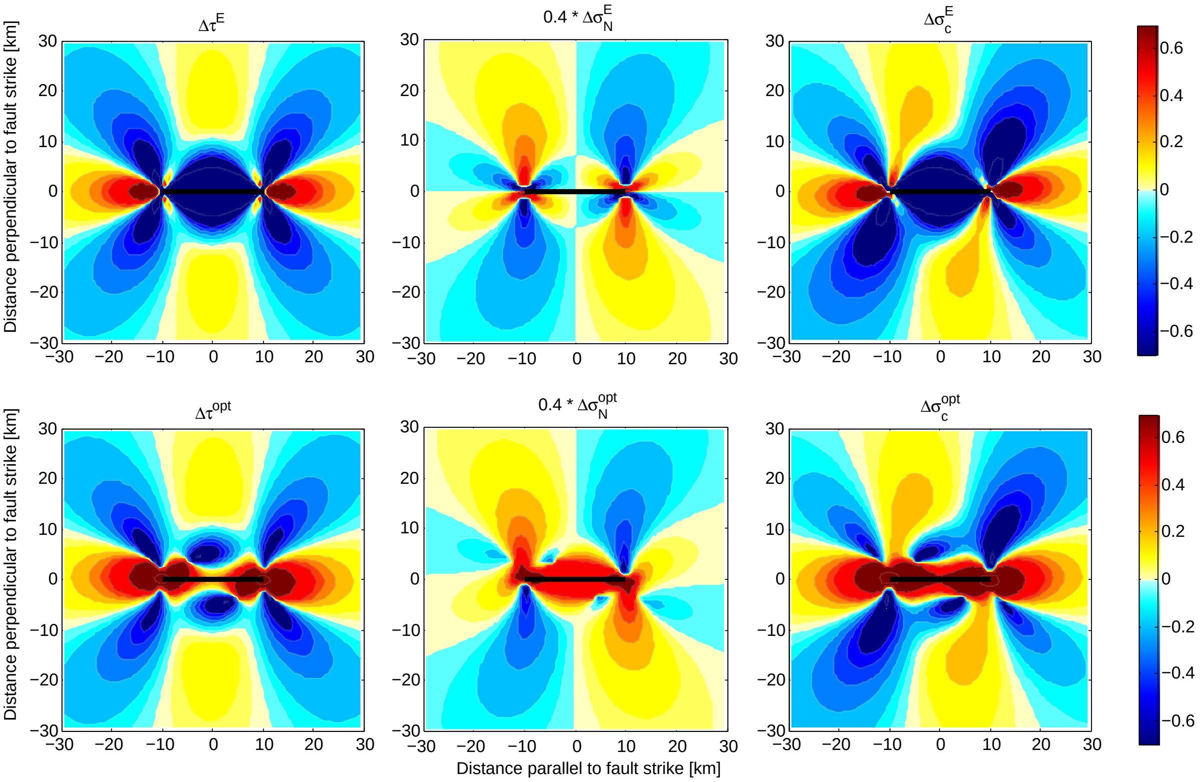

Figure 5.3: *Graphical representation of eq. 5.1 for a reference system with the x-axis parallel to the strike of the fault (upper row) and for "optimally oriented fault planes" (lower row) (this means that the stress field is rotated, for each point separately, to the orientation corresponding to the maximum Coulomb stress increase). Panels from left to right: shear stress change, normal stress change and Coulomb stress change.*

of 0.25. Concerning the rheological properties, we first considered a medium with a strong viscoelastic lower crust and a weak viscoelastic mantle (hereinafter Model 1). However, although other authors have favored similar stratification for their studies (e.g. Freed and Lin, 2001; Pollitz and Sacks, 2002), there is also the possibility that the most appropriate description of the medium is the opposite, with a weak lower crust and a strong mantle (Deng et al., 1998, 1999; Zeng, 2001), or that the lithosphere should be considered elastic over its whole depth (Casarotti and Piersanti, 2003). For this reason, we also considered two models incorporating these options (respectively Model 2 and Model 3). In all the cases, viscoelastic layers are modeled as Maxwell bodies. According to recent studies, other rheological models could be more adequate to analyze post-seismic relaxation processes, like the Standard Linear Solid rheology (Cohen, 1982; Pollitz et al., 1998) or power-law, non-linear rheologies (Pollitz et al., 2001; Freed and Bürgmann, 2004). However, from the present data we are not able to discern among different rheologies. For this reason, we prefer to use the simplest and most used linear Maxwell rheology, instead of more complicated models that would add additional unknowns to our analysis.

Fault rupture locations and geometry, as well as slip distribution, were obtained from tectonic and geological maps and published field observations (see Table 5.1). We modeled the tectonic stress loading with steady slip over the depth range 17 to 100 km, using the deep dislocation technique proposed by (Savage, 1983). The slip increases from zero at 17 km depth to its full magnitude at a depth of 35 km. The magnitude of the slip on the NAF was taken from GPS interpretations (Flerit et al., 2003, 2004). Fig. 5.2c displays the exact amount of annual fault slip used to model the different segments of the NAF.

With these parameters, we carried out calculations for a grid of 81 × 501 points, with a spacing of approximately 2 km, covering the study region outlined in Fig. 5.1. We also calculated Coulomb stress changes at a 2 km spacing along the segments. For these computations, we considered the full geometry for each rupture segments. However, only horizontal stress components were used for the calculations. Since the most important deformation along the NAF is horizontal, this is a reasonable simplification.

5.5 Results

Fig. 5.5 illustrates the evolution of the cumulative Coulomb stress changes on vertical fault planes striking in E-W direction. We choose a fixed strike direction for these calculations instead of using optimally oriented fault planes to facilitate the comparison between different snapshots. For these calculations we used Model 1, with $\mu' = 0.4$ and lower crust and mantle viscosities of $5 \cdot 10^{19}$ Pa·s and 10^{18} Pa·s, respectively. Since most of the large earthquakes along the NAF have an hypocentral depth of 10-15 km (e.g. Şengör et al., 2005), Coulomb stresses were calculated at 10 km depth, regarding this as a realistic depth for earthquake nucleation. Fig. 5.5a shows the effect of the steady

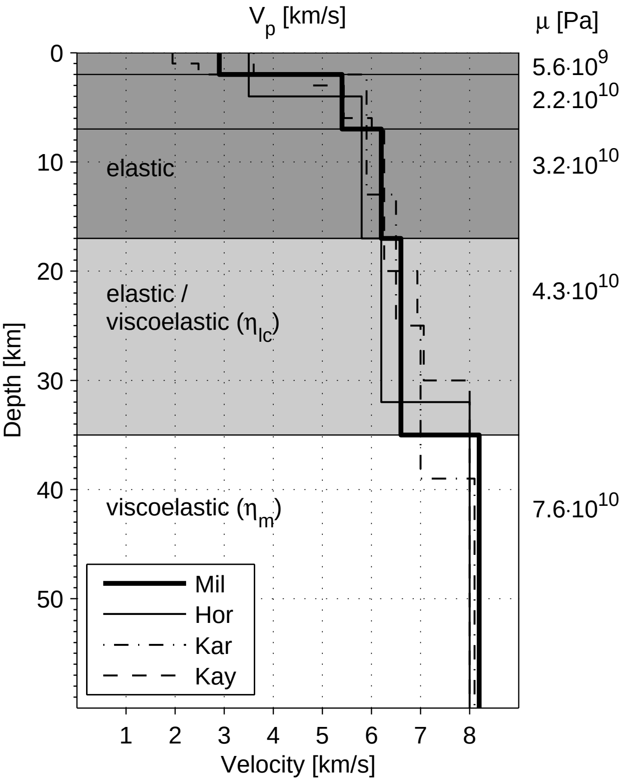

Figure 5.4: *Parameters of the horizontally stratified medium. The same stratification values have been applied for different tectonically active areas along the NAF (Milkereit et al., 2000, 2004, thick line). Results from other studies are also shown for comparison (Karahan et al., 2001; Horasan et al., 2002; Kaypak and Eyidoğan, 2005). We considered a Poisson's ration of 0.25. The lower crust and the mantle have variable viscosities* η_{lc} *and* η_m*, respectively.*

tectonic stress loading over 10 years, to illustrate the influence of this process on the total field. The state of the stress field at the beginning of the sequence is shown in Fig. 5.5b, where only the elastic response of the medium to the 1939 event is present. The evolution in time is then shown, with snapshots immediately before and after the 1943 event (Fig. 5.5c and 5.5d) and after the 1992 event (Fig. 5.5e). Fig. 5.5f displays the stress changes due exclusively to viscoelastic relaxation between 1939 and 1992, to demonstrate the effect this process has on the total stress field. Values near the NAF typically range from 0.3 to 0.5 MPa, greater in magnitude than those corresponding to steady tectonic loading for the same period. After both 1999 events, the situation is the one displayed in Fig. 5.5g, and the evolution of the field until the present time is shown in Fig. 5.5h (total stress field) and Fig. 5.5i (only the viscoelastic relaxation effect).

5.5.1 Coulomb stress on the rupture surfaces

We calculated the Coulomb stress change on the rupture surfaces of the events posterior to 1939 and separately assessed the influence of tectonic, elastic and viscoelastic loading. We regarded positive stress values below 0.01 MPa as not significant, since steady tectonic loading can cause such amounts of stress over a very short period of time (Stein et al., 1997). Table 5.2 compiles values for the maximum and average change stress at the rupture surfaces, while Table 5.3 displays the percentage of the rupture length with $\sigma_c \geq 0.01$ MPa. The values in both tables display the state immediately before the corresponding event. The values were calculated for Model 1, including results with and without steady tectonic loading, as well as for elastic and viscoelastic media. For the latter, mantle viscosity values from $\eta_m = 5 \cdot 10^{17}$ to 10^{19} Pa·s were considered. We maintained a constant ratio with the lower crust viscosity of $\eta_{lc}/\eta_m = 50$ to simplify the analysis. Previous works dealing with southern California propose ratios ranging from 3 to 100 Deng et al. (1998, 1999); Freed and Lin (2001); Zeng (2001); Pollitz and Sacks (2002), although there is no agreement on whether weak-lower-crust or weak-mantle models are more appropriate.

The joint effect of tectonic, elastic and viscoelastic loading produces positive average Coulomb stress changes on most of the rupture surfaces. The percentage of the rupture surfaces over the threshold value is at its maximum for $\eta_m = 5 \cdot 10^{17} - 10^{18}$ Pa·s. Three of the ruptures (1942, 1951 and 1967) show negative average Coulomb stress change regardless of the model assumed.

The entire length of the 1951 rupture is in a stress shadow, with the whole surface stressed by less than 0.01 MPa (Table 5.3). By contrast, the 1957 event shows, independent of the model assumptions, values above this threshold for all its length. The percentage of rupture surface above the threshold for the remaining 7 events depends on the contributions considered for the stress loading, as well as the value of the viscosity when viscoelastic models are used. In general, the influence of viscoelastic relaxation is comparable to that of tectonic loading.

We also carried out calculations using an effective coefficient of friction of 0.6 (Table 5.4a). This value accounts for a situation where most of the fluids are expelled from the fault zone. The results differ slightly from those presented above, although changes are not systematic. Most notably, when the total stress field on the 1944 rup-

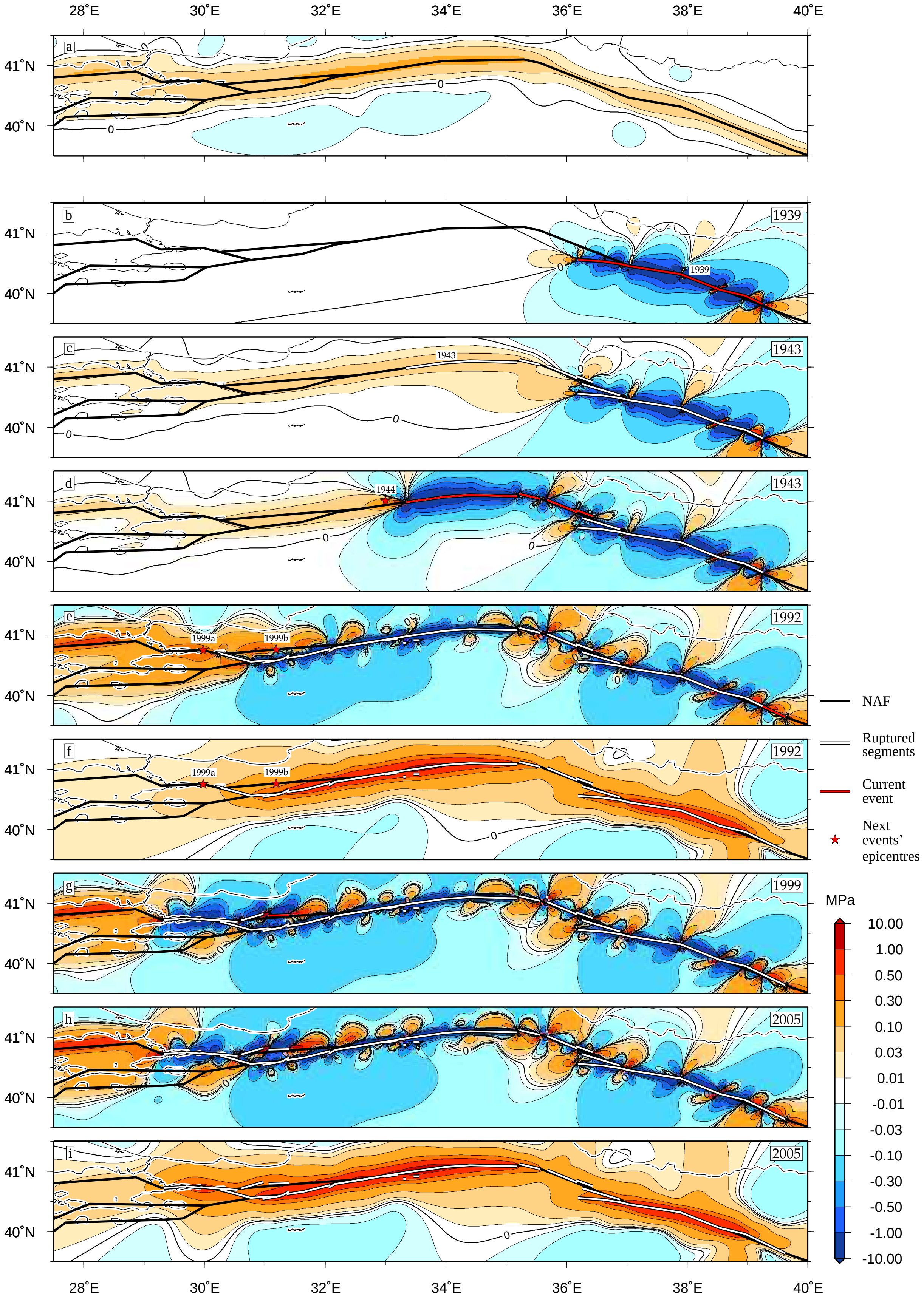
28˚E
30˚E
32˚E
34˚E
36˚E
38˚E
40˚E
41˚N
40˚N
a
0
b
1939
c
1943
0
d
1944
1943
e
1999a
1999b
1992
f
g
1999
h
2005
i
NAF
Ruptured segments
Current event
★ Next events' epicentres
MPa
10.00
1.00
0.50
0.30
0.10
0.03
0.01
-0.01
-0.03
-0.10
-0.30
-0.50
-1.00
-10.00

viscosity	1942		1943		1944		1951		1957		1967		1992		1999a		1999b	
∞	0.07	-0.67	0.11	0.04	13.37	0.36	-1.52	-3.30	4.52	0.86	0.89	-0.31	3.40	1.29	0.98	0.33	0.57	0.26
$5 \cdot 10^{17}$ Pa·s	0.17	-0.48	0.23	0.07	13.40	0.37	-1.23	-2.92	4.74	1.00	1.12	-0.16	4.22	1.80	1.14	0.44	0.80	0.50
10^{18} Pa·s	0.15	-0.53	0.20	0.07	13.38	0.37	-1.27	-2.99	4.69	0.97	1.06	-0.20	3.98	1.64	1.10	0.41	0.76	0.46
$5 \cdot 10^{18}$ Pa·s	0.09	-0.64	0.13	0.05	13.37	0.36	-1.41	-3.18	4.61	0.92	0.98	-0.25	3.68	1.46	1.05	0.39	0.71	0.41
10^{19} Pa·s	0.08	-0.66	0.12	0.05	13.37	0.36	-1.46	-3.24	4.57	0.90	0.94	-0.27	3.63	1.43	1.03	0.37	0.68	0.39
From tect. loading	0.04		0.05		0.05		0.10		0.11		0.22		0.64		0.46		0.56	

Table 5.2: *Maximum and average Coulomb stress changes ($\Delta\sigma_c$) on the ruptures immediately before each event. Values are for a purely elastic model (infinite viscosity) and for 4 different mantle viscosities, η_m. The ratio with the lower crust viscosity is kept constant at $\eta_{lc}/\eta_m = 50$. The last line displays the fraction of the results produced by steady tectonic loading. Results are for Model 1 (see text), and an effective coefficient of friction of 0.4.*

ture surface is considered, the stressed surface decreases from 100% for $\mu' = 0.4$ to 89% for $\mu' = 0.6$. The total stress field on the 1942 rupture surface increases, so that the considered percentage increases from 21% for $\mu' = 0.4$ to 29% for $\mu' = 0.6$. The elastic contribution to the 1999a event is notably larger, increasing the stressed surface from 49% for $\mu' = 0.4$ to 57% for $\mu' = 0.6$. The viscoelastic contribution to the 1943 event decreases, with the stressed surface decreasing from 44% for $\mu' = 0.4$ to 35% for $\mu' = 0.6$.

Results for Model 2 and Model 3 (Table 5.4b and c) also show localized differences. Most notably, the stressed area on the rupture surfaces of the 1942 and 1967 events increases to 36% and 78%, respectively, for Model 2. In general, the effect of viscoelastic relaxation is smaller for Model 3, as it would expected. The stressed surface of the

◁

Figure 5.5: *Evolution of the Coulomb stress field since 1939. Calculations were made for fault planes striking in an E-W direction, and the results were evaluated for 10 km depth. Black thick lines represents all segments used to model the tectonic loading at the NAF. White lines display ruptured segments and red lines unruptured segments, immediately before their activation. Panel a shows the effect of 10 years of steady tectonic loading. The rest of the panels display the situation at different points in time: (b) immediately after the 1939 event; (c) before the 1943 event; (d) after the 1943 event; (e) after the 1992 event; (f) effect of viscoelastic relaxation from 1939 to 1992; (g) after the 1999b event; (h) current state of the Coulomb stress field; (i) effect of viscoelastic relaxation from 1939 to 2005.*

	viscosity	1942	1943	1944	1951	1957	1967	1992	1999a	1999b
	∞	14	93	95	0	100	75	100	85	100
with	$5 \cdot 10^{17}$Pa·s	29	96	100	0	100	78	100	93	100
tectonic	10^{18}Pa·s	21	95	100	0	100	78	100	91	100
loading	$5 \cdot 10^{18}$Pa·s	18	93	95	0	100	75	100	88	100
	10^{19}Pa·s	14	93	95	0	100	75	100	88	100
	∞	11	20	52	0	100	70	94	49	7
without	$5 \cdot 10^{17}$Pa·s	21	59	67	0	100	75	100	81	29
tectonic	10^{18}Pa·s	21	44	57	0	100	73	100	81	29
loading	$5 \cdot 10^{18}$Pa·s	14	21	54	0	100	73	94	81	21
	10^{19}Pa·s	11	21	53	0	100	73	94	81	21

Table 5.3: *Percentage of fault rupture showing $\Delta\sigma_c \geq$ 0.01 MPa. Values when including the effects of steady tectonic loading (upper five lines) and when excluding this effects (lower five lines). Model parameters as in Table 5.2.*

1943 rupture decreases to 33% for both Model 2 and Model 3. In the latter model, the stressed surface for the 1943, 1992 and 1999b events decreases in 11%, 6% and 8%, respectively.

5.5.2 Coulomb stress at the epicenters

Fig. 5.6 displays the time evolution of the Coulomb stress at the epicenters of the events posterior to 1939. For the 9 epicenters, the effect of the corresponding rupture is a stress release. Also, the epicenters of 8 out of 9 earthquakes are stressed with high σ_c values, although there are differences regarding its magnitude. Epicenters of the events on the central and eastern part of the NAF (1942, 1943 and 1944) were loaded by about 0.1 MPa before the rupture took place. The epicenters for 1957 and 1967, on the other hand, stored stresses up to values around 0.3 MPa, and up to 0.5 MPa for the 1999a and 1999b epicenters, before the earthquakes occurred. The 1992 epicenter was loaded with more than 0.9 MPa immediately before the shock took place.

In general, it can be observed that the increase in magnitude of $\Delta\sigma_c$ due to viscoelastic relaxation is comparable, and in some cases larger, than that due to steady tectonic loading (compare the thin dashed and solid lines, Fig. 5.6).

The location of epicenters, especially the earlier ones, are subject to considerable inaccuracy. Fig. 5.7 shows the variation in the magnitude of $\Delta\sigma_c$ immediately before each event when a realistic 0.1^o inaccuracy is considered. In general, the sensitivity of Coulomb stress change to the location of the epicenter is not too strong, with the exceptions of the 1944 and 1951 events.

5.5.3 The 1999 Izmit and Düzce events

The most recent earthquakes of the westwards migrating sequence were the 1999 M_w = 7.4 Izmit/Kocaeli (1999a) and M_w = 7.1 Düzce (1999b) events. Fig. 5.8 shows the state of the total cumulative $\Delta\sigma_c$ field for optimally oriented fault planes, as well as the stress load on the rupture surfaces, immediately before both events. We

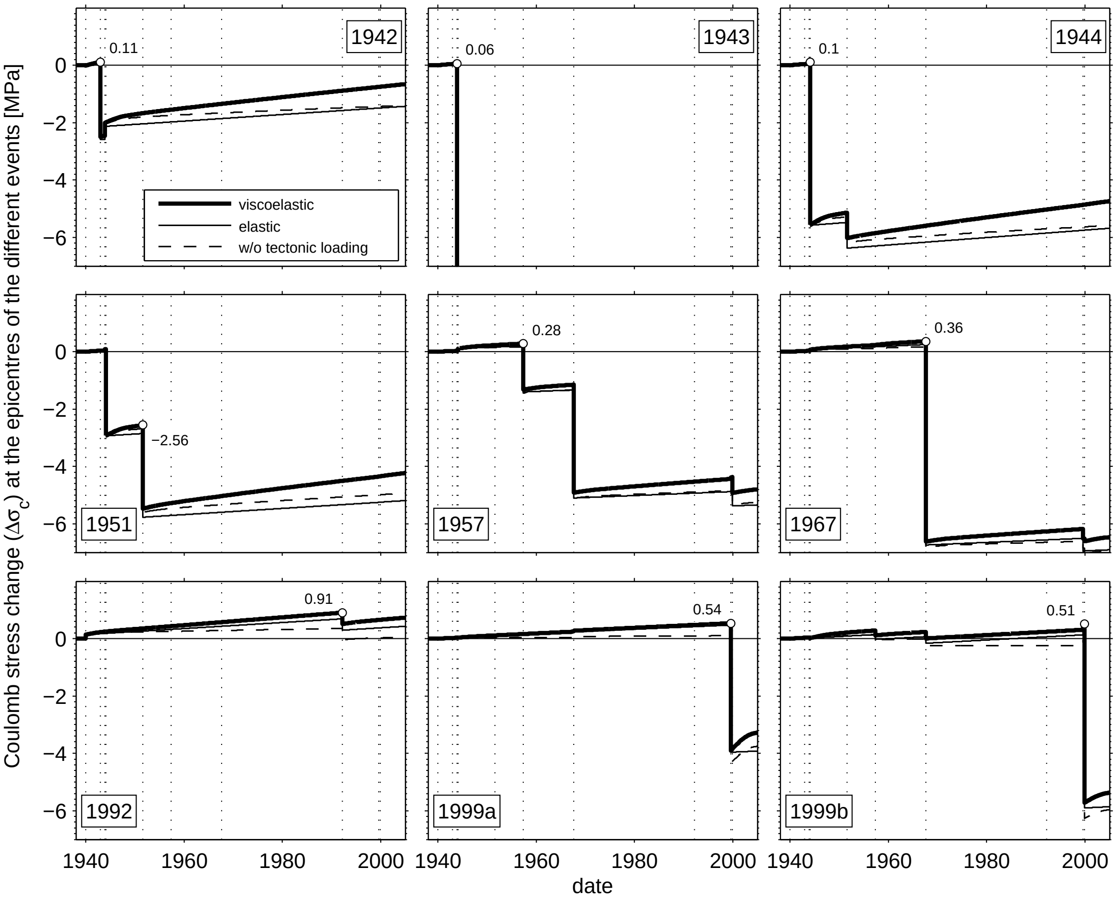

__Figure 5.6:__ Time-evolution of Coulomb stress on the epicenters of the considered events (Table 5.1). Vertical dotted lines mark the timing of each event considered. The thick solid line shows the stress development when elastic and viscoelastic stress changes, as well as tectonic loading, are considered. The thin solid line shows the development when the effect from viscoelastic relaxation is not considered. The thin dashed line displays the case where viscoelastic relaxation is considered but tectonic loading is not. The white dot marks the moment and state of stress at the epicenter when the rupture occurs. The value marked close to the dot is the Coulomb stress at that moment, in MPa.

assumed a 10 MPa uniaxial compression N120°E oriented regional stress field for the calculation of the optimally oriented fault planes (Stein et al., 1997; Hubert-Ferrari et al., 2000; Pınar et al., 2001). Most of the surface of the faults involved in the 1999a event were subjected to high Coulomb stresses at the moment of the earthquake (Fig. 5.8a). With the exception of the Sapanca-Akyazi segment, the rest of the rupture length were loaded with stress values over 0.1 MPa. Moreover, the Izmit-Sapanca Lake segment, were the epicenter was located, as well as its surroundings, were subjected to stresses over 0.3 MPa. The 1999b rupture was also mostly loaded, although the Coulomb stresses in this area were partially released by the 1944, 1957 and 1967 events. The stress changes caused by the 1999a shock induced important changes on the 1999b rupture. Stresses on the later rupture were larger than before the 1999a

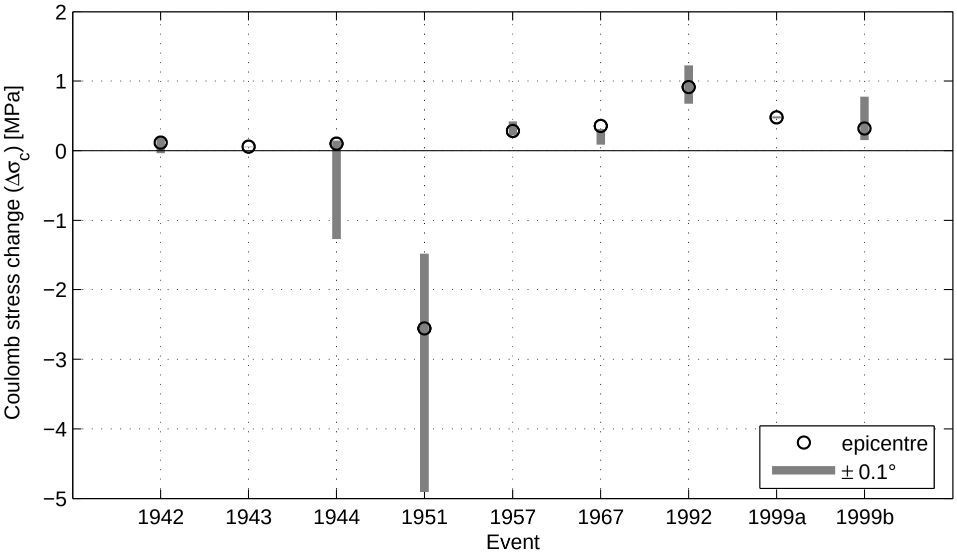

Figure 5.7: *Variation of the Coulomb stress changes when possible inaccuracies in the epicentral location are considered. The circle shows the* $\Delta\sigma_c$ *value for the epicentral location provided by the corresponding catalogue (see Table 5.1). The grey line display the variation when this location is changed by* 0.1^o *in any direction.*

shock took place (Fig. 5.8b), including at the event's epicenter (Fig. 5.6).

The local $M \geq 2$ seismicity (KOERI, 2005) correlated with the state of the $\Delta\sigma_c$ field before the 1999a event (Fig. 5.8a). In addition, there was an important cluster of activity in the place where the epicenter of the 1999a event was going to take place. After this event and before the 1999b event the correlation is less apparent (Fig. 5.8b). It should be noted that the displayed seismicity ranges from 0 to 17 km depth. For deeper regions, the calculated $\Delta\sigma_c$ field may not be representative.

5.5.4 The Marmara Sea region

The current situation in the Marmara Sea region according to our computations is displayed in Fig. 5.9a, for optimally oriented fault planes and for the two segments of the NAF in the region. We assumed a 10 MPa uniaxial compression N120^{o}E oriented regional stress field. The effect of the $M_s = 6.4$ 1963 Cinarcik event (Ambraseys and Jackson, 2000) was taken into account, since its influence in the region may not be negligible.

Most of the region shows high stress values. The effect of tectonic loading (Fig. 5.9b, for 10 years), is not as important as the stress changes induced by post-seismic stress relaxation. Figs. 5.9c and 5.9d, respectively 5 and 10 years after the last event of the sequence, show that the viscoelastic relaxation increases the stresses in the region at a faster rate than steady tectonic loading.

The local $M \geq 2$ seismicity between 0 and 17 km deep (KOERI, 2005) correlates with the calculated Coulomb stress change, with high activity rates associated with the lobe of large $\Delta\sigma_c$ values at the western end of the 1999a rupture ($\Delta\sigma_c \geq 0.3$ MPa), and more activity, in general, for areas with $\Delta\sigma_c \geq 0.1$ MPa.

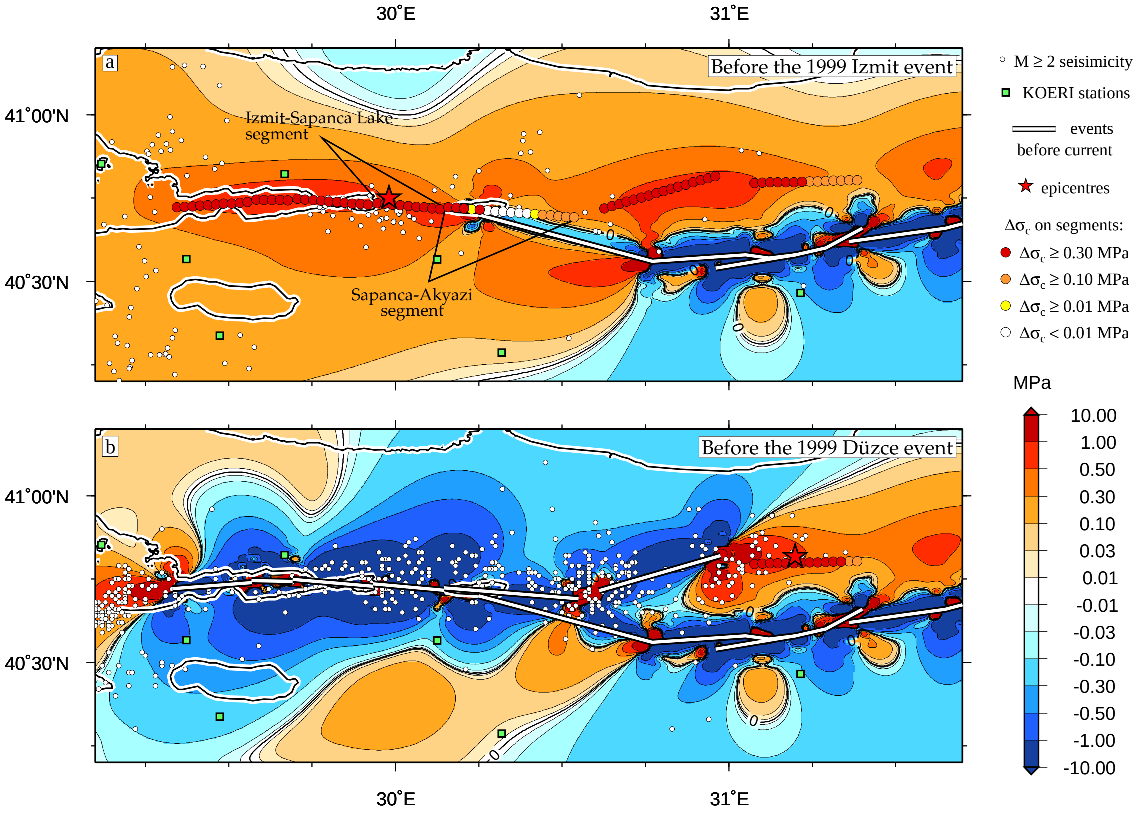
30˚E
31˚E
41˚00'N
40˚30'N
a
Before the 1999 Izmit event
Izmit-Sapanca Lake segment
Sapanca-Akyazi segment
b
Before the 1999 Düzce event
M ≥ 2 seisimicity
KOERI stations
events before current
epicentres
Δσc on segments:
Δσc ≥ 0.30 MPa
Δσc ≥ 0.10 MPa
Δσc ≥ 0.01 MPa
Δσc < 0.01 MPa
MPa
10.00
1.00
0.50
0.30
0.10
0.03
0.01
-0.01
-0.03
-0.10
-0.30
-0.50
-1.00
-10.00

Figure 5.8: *Coulomb stress change at 10 km depth on optimally oriented fault planes (color field, 10 MPa uniaxial compression, N120°E oriented regional stress field) and on given faults (filled circles), for Model 1. (a) shows the situation before the August 17th, 1999 event (1999a), and (b) before the November 12th, 1999 shock (1999b). White lines are already ruptured segments. Red stars display the location of the epicenters. Small white dots show the local $M \geq 2$ seismicity at depths between 0 and 17 km over six months before the 1999a event (a) and for the period between the 1999a and 1999b shocks (b). Green squares display the location of the Kandilli Observatory and Earthquake Research Institute (KOERI) seismic stations.*

5.6 Discussion

5.6.1 Coulomb stress on the rupture surfaces and at the epicenters

In general, the Coulomb stress criterion explains the triggering of subsequent earthquakes by preceding ones. Almost all rupture surfaces, or a large percentage of them, and/or their epicenters, were strongly stressed at the moment of the shock (Table 5.3 and Fig. 5.6). The results for the epicenters are stable with respect to the possible inaccuracies in their location (Fig. 5.7), with the exception of the 1944 and 1951 earthquakes. The 1944 epicenter was located very close to previous ruptures (1943, which took place only 2 months before the 1944). Close to the rupture, the stress change gradient is very high, hence the position of the epicenter plays a major role. At the epicenter of the 1951 event, $\Delta\sigma_c$ is strongly negative, independent of variation in its location.

It should be noted that only the ruptures of the 1944, 1957, 1992 and 1999b events were stressed over their whole surfaces under certain conditions (Table 5.3). For most of the events, the rest of the surface was probably dynamically activated during the shock, as described by the general asperity model (Lay and Kanamori, 1981). With the exception of the 1942 earthquake, over 75% of the events' ruptures was stressed before the event. This coincide with the results of (Steacy and McCloskey, 1998), according to which large events only occur when the entire fault is highly stressed relative to its strength. In general, the percentage of stressed surface does not change drastically with the viscosity chosen, and values lower than 10^{18} Pa·s for the weak layer do not lead to noteworthy improvements.

The rupture of the 1992 event was strongly stressed over its whole surface, independently of the model assumptions. The stress at the epicenter reached 0.91 MPa before the shock. However, a potentially important factor is the seismicity further to the east, and on the EAF, south of the 1992 shock. At least 3 strong events took place in these areas between 1939 and 1992, in 1949, 1966 and 1971 (Dewey, 1976), and they may have had a significant influence on the Coulomb stress on the 1992 rupture surface. In addition, recent studies show that fault distribution in the region east of the 1992 event might be more complex than the one traditionally assumed (Milkereit et al., 2004). Other authors suggest that deep steady slip may not be adequate to estimate the stress changes due to steady tectonic loading in this region (Nalbant et al., 2005b). For these reasons, it is unlikely that we would improve our understanding of this region by broadening our study area further to the east. Other than this, it would introduce several additional unknown parameters into our study. Measurements and estimates of the slip on the surface of the 1939 event are insufficient (Barka, 1996), and the 1992 event did not provide surface expressions of the rupture (Grosser et al., 1998), so that the present results about the 1992 event should be treated carefully. A more detailed study, similar to the one carried out by (Nalbant et al., 2005b), would be necessary to better understand the influence of viscoelastic relaxation in this area.

We observed that tectonic loading and viscoelastic relaxation increased the stressed surface by a comparable percentage, with the exception of the 1943, 1944 and 1999b events (Table 5.3). For these three earthquakes, the effect of steady tectonic loading is much more important than that from viscoelastic relaxation. For the 1943 and 1944 events, this is due to two factors: first, the time interval between these shocks and earlier events in the sequence is too short for viscoelastic relaxation to have a more important effect (Fig. 5.6); second, the rupture surfaces of these earthquakes were notable long, with mainly their easternmost ends loaded by the previous ruptures. For these two events, as well as for the 1939 earthquake, the steady tectonic loading during the preceding centuries seems to be the determining factor for the extension of the rupture surface, rather than the calculated Coulomb stress changes. The case of the 1999b earthquake appears to be different. For this event, the elastic/coseismic stress changes only manage to stress 7% of the rupture surface. The effect of viscoelastic relaxation since 1939 is about 0.3 MPa (see Fig. 5.5). When combined with the viscoelastic stress changes only 21-29% of the rupture surface overcomes the threshold value of 0.01 MPa (Table 5.3). The tectonic loading, on the contrary, rises the percentage of stressed surface from 7% to 100%.

The 1951 event presents a rupture surface that is totally unloaded, independent of the assumptions made. This, together with the results for the 1951 epicenter, indicate that the Coulomb stress change approach, as applied in this study, cannot offer a plausible explanation for the occurrence of this event. Some authors model this shock as a reverse slip event (Stein et al., 1997), striking parallel to the NAF. We could not find any evidence in the literature to support this possibility. On the contrary, the fault plane solution for this event is that of a strike-slip event (Stein et al., 1997; McKenzie, 1972; Şengör et al., 2005), and the studies of the surface expression of the rupture also deny the existence of significant reverse slip (Pinar, 1953; Barka and Kadinsky-Cade, 1988). In addition to the poorly known geometry and mechanism of the 1951 shock, it is possible that creep occurring on part of the 1944 rupture (Ambraseys, 1970; Kondo et al., 2005) may have played a role in the triggering of the 1951 event.

We tested the stability of our results by comparing different models. The role of the effective coefficient of friction is not trivial, as it modulates the contribution of the normal stress to the Coulomb stress. For most of the earthquakes studied in this work, the influence of the value for μ' is very limited (Table 5.4), with the exception of the 1942, 1943 and both 1999 events, for which some model assumptions cause noteworthy changes. The reason for this is the relative location of the rupture surfaces. At the center of the study region, the events in the sequence fall in line along the NAF, with each event's rupture adjacent to the previous ones. Normal stresses are small in this direction, hence Coulomb stress change is basically governed by shear stress change, and the influence of μ' disappears. Other than this, the westernmost part of the 1939 rupture occurred south from the main NAF (Barka, 1996), as well as south from the future 1943 and 1944 ruptures. Similarly, the 1999 events took place in a region where the geometry of the NAF is more complicated and shocks did not line up along the same main fault. Normal stress field gains importance when calculating $\Delta\sigma_c$ in this circumstances, and the choice for the value of μ' has a consequence on the results.

Changes in the properties of the medium (Table 5.4b and c) also led to punctual changes in the results. Results for Model 3 are lower than those for Model 1, although not drastically, while Model 2 gave results that differ significantly from those of Model 1. However, the percentage of the stressed area on the rupture surfaces does not systematically increase or decrease between the models, so that we cannot extract information about the rheological stratification of the region from the analysis of the Coulomb stress changes.

5.6.2 The 1999 Izmit and Düzce events

If we assume that an important part of the rupture surface must be stressed for an earthquake to take place, then Model 2 with $\eta_{lc} = 10^{18}$ Pa·s or Model 1 with $\eta_m = 5 \cdot 10^{17} - 10^{18}$ Pa·s are the favored models to explain the triggering of the 1999a event. In these cases, 91-94% of the rupture is stressed (Tables 5.3 and 5.4). However, the difference in the results from among the models and viscosity values is not strong. When tectonic loading is considered in addition to the earthquake related coseismic changes, the stressed surface increases from 49% to 85%. A similar increase takes place when relaxation is taken into account, with the result of 81% of the surface being stressed.

When only the coseismic stress change due to previous events is considered, only

7% of the 1999b rupture surface is brought over the threshold value of $\Delta\sigma_c \geq 0.01$ MPa (Table 5.3). When the effects of viscoelastic relaxation are also considered, the Coulomb stress change increases by an average of 0.2 MPa, and the percentage of the stressed surface raises to 29%. This increase in the Coulomb stress is comparable to 20 years of tectonic loading.

Other time-dependent processes, such as afterslip, ductile creep at depth or poroelastic diffusion processes, may have played an important role in the triggering of the 1999b event (Bürgmann et al., 2002; Hearn et al., 2002). Hearn et al. (2002) analyzed the observed post-seismic GPS deformation between the 1999a and 1999b earthquakes to evaluate which process could better explain the occurrence of the 1999b shock. They conclude that the most likely explanation is velocity-strengthening frictional afterslip, and favor this possibility against viscoelastic lower crust relaxation. The viscosity for the lower crust needed to reproduce the fit obtained by means of frictional afterslip models is $\eta = 10^{17}$ Pa·s. The authors argue that this value is much lower than most previous estimates of crustal viscosity. However, they do not consider the effects of viscoelastic relaxation in lower layers, although they point out that similar horizontal displacements are obtained when the ratio between viscosity and layer thickness is kept constant and the top of the viscoelastic layer unchanged. Our analysis of the stress field shows that the effect of a viscoelastic half-space (not only a viscoelastic layer) underlying the elastic layers is not negligible. A similar result can be expected for the surface displacement field (see Chapter 4), hence it appears more realistic to include the viscoelastic behavior of lower regions of the crust and upper mantle when modeling these displacements.

Using an elastic medium and vertical fault planes, Bürgmann et al. (2002) interpreted the post-seismic deformation with afterslip on the 1999a rupture and its prolongation in the E-W direction and with depth. According to their results, rapid slip took place at depth below the eastern part of the 1999a rupture. This would create additional stress on the future 1999b rupture surface, being therefore a potential explanation for the time delay between both 1999 events. Also, poroelastic rebound has proven to have an important role in the first months after an earthquake (Peltzer et al., 1998; Jónsson et al., 2003). Given the short time interval between the 1999a and 1999b events, it might be necessary to consider its influence. However, Hearn et al. (2002) showed that the deformation caused by poroelastic rebound alone cannot explain the measured deformation. From these previous works and the results presented here, it is most likely that the time delay between the 1999 Izmit and the 1999 Düzce events, as well as the time evolution of the observed deformation can only be explained as a combination of several different time-dependent processes.

Utkucu et al. (2003) carried out an analysis of the Coulomb stress state on the 1999 Düzce rupture surface under different conditions. Using an elastic half-space model, they find that the 1999 Izmit event increased the stress on most of the future 1999 Düzce rupture surface, with values for $\Delta\sigma_c$ over 1.2 MPa, with most of the rupture surface stressed between 0 and 0.4 MPa. According to our results, the Coulomb stress increase ranges between 0.25 and 0.05 MPa, from west to east on the 1999 Düzce rupture surface. The difference is due to the different rupture segments used by Utkucu et al. (2003) and in the present study. Utkucu et al. (2003) considered a small eastern segment striking E-W at the end of the 1999 Izmit rupture. However, the observed slip

			1942	1943	1944	1951	1957	1967	1992	1999a	1999b
a	with tectonic loading	elastic	14	94	89	0	100	75	100	88	93
		viscoelastic	29	98	89	0	100	80	100	93	100
	without tectonic loading	elastic	11	21	51	0	100	68	94	57	7
		viscoelastic	21	35	55	0	100	75	100	81	21
b	without tectonic loading	viscoelastic	39	94	95	0	100	83	100	94	100
		viscoelastic	36	33	55	0	100	78	100	78	29
c	without tectonic loading	viscoelastic	21	95	99	0	100	75	100	88	100
		viscoelastic	18	33	55	0	100	73	94	81	21

Table 5.4: *Percentage of fault rupture showing $\Delta\sigma_c \geq$ 0.01 MPa. Values for Model 1 with $\mu' = 0.6$ (a), for Model 2 with $\mu' = 0.4$ (b), and for Model 3 with $\mu' = 0.4$ (c). Both elastic and viscoelastic media are considered. The viscosities used are $\eta_m = 10^{18}$ Pa·s and $\eta_{lc}/\eta_m = 50$ for (a) and (c), and $\eta_{lc} = 10^{18}$ Pa·s with $\eta_{lc}/\eta_m = 50$ for (b).*

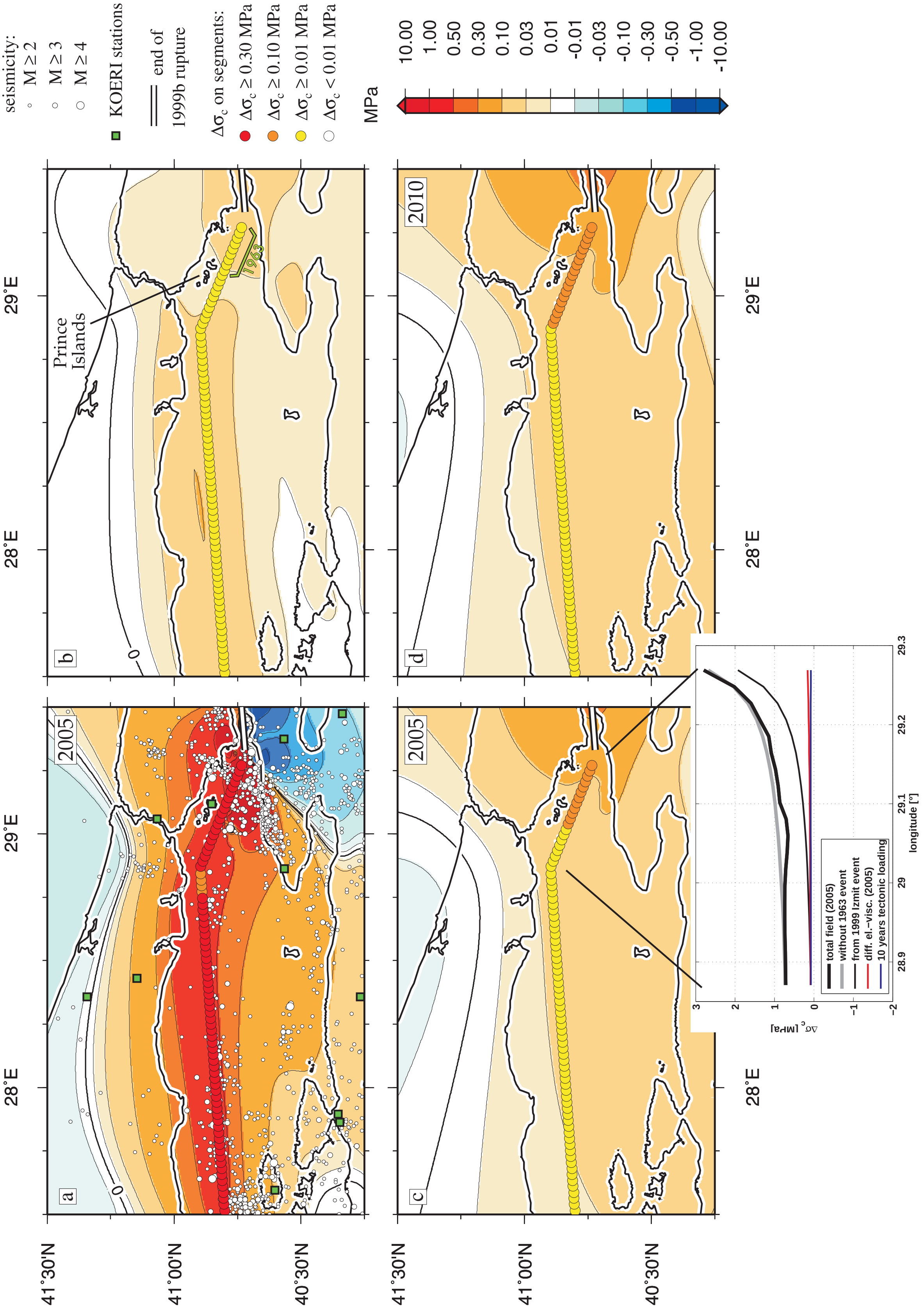
seismicity:
M ≥ 2
M ≥ 3
M ≥ 4
KOERI stations
end of 1999b rupture
$\Delta\sigma_c$ on segments:
$\Delta\sigma_c \geq 0.30$ MPa
$\Delta\sigma_c \geq 0.10$ MPa
$\Delta\sigma_c \geq 0.01$ MPa
$\Delta\sigma_c < 0.01$ MPa
MPa
10.00
1.00
0.50
0.30
0.10
0.03
0.01
-0.01
-0.03
-0.10
-0.30
-0.50
-1.00
-10.00
a
2005
b
c
2005
d
2010
Prince Islands
1963
0
28˚E
29˚E
41˚30'N
41˚00'N
40˚30'N
total field (2005)
without 1963 event
from 1999 Izmit event
diff. el.–visc. (2005)
10 years tectonic loading
$\Delta\sigma_c$ [MPa]
longitude [°]
28.9
29
29.1
29.2
29.3
3
2
1
0
−1
−2

in that area is very small (Barka et al., 2002), and it may be a secondary effect of the 1999 Izmit shock. We used the geometry obtained from the inversion of InSAR data (Wright et al., 2001), that fitted the observed deformation field without the need of an eastern E-W striking segment.

When the effect of previous events is also considered, we find that the stressed surface decreases notably, in accordance with the results of Utkucu et al. (2003). However, the influence of tectonic loading is very different. This is due to the different elements used to model the tectonic movements. Utkucu et al. (2003) consider a simplified geometry for the long-term tectonic loading model, whereas we used the more detailed results from (Flerit et al., 2003, 2004), based on GPS velocity vectors compiled by McClusky et al. (2000). Utkucu et al. (2003) model uses a plate rate of 24 mm/a along the Mudurnu Valley, where the 1967 earthquake took place. According to Flerit et al. (2003, 2004), it is more appropriate to split the 24 mm/a in this area into two branches with 12 mm/a each (Fig. 5.2c), the northernmost of which runs below the 1999b Düzce fault.

5.6.3 The Marmara Sea region

The local seismicity in the Marmara Sea region correlates with the Coulomb stress change (Fig. 5.9a). A purely elastic approach when calculating the state of the stress field neglects the important stress changes due to viscoelastic relaxation. These process loaded the eastern part of the Marmara Sea region with stresses over 0.1 MPa (Fig. 5.9c). Also, the viscoelastic effect is comparable or even larger than the stress increase due to 10 years of tectonic loading (compare Fig. 5.9b and 5.9c). Both processes generate stress changes that differ in their pattern: the influence of viscoelastic relaxation is more important to the east of the Marmara Sea region, whereas tectonic loading increases σ_c in a more homogeneous way. The eastern segment of the NAF in the Marmara Sea, which was already strongly stressed ($\Delta\sigma_c \geq 0.3$ MPa, Fig. 5.9a), is currently being loaded at a much faster rate than would be expected due to tectonic loading alone (Figs. 5.9c and 5.9d). Accordingly, stress changes due to viscoelastic re-

---

◁

Figure 5.9: *Coulomb stress change at 10 km depth on optimally oriented fault planes (color field, 10 MPa uniaxial compression, $N120^oE$ oriented regional stress field), and on given faults (filled circles), for Model 1. The 1963 $M_s = 6.4$ Cinarcik earthquake rupture surface is marked in (b), south west of the Prince Islands. The total stress field is displayed in (a); (b) shows the change in Coulomb stresses due to 10 years of steady tectonic loading; (c) and (d) show the cumulative effect of viscoelastic relaxation, for the present time and in 2010, respectively. The white framed line displays the western end of the 1999a rupture. Small white dots in (a) show the local $M \geq 2$ seismicity for the period 2000-2004 at depths between 0 and 17 km. Green squares display the location of the Kandilli Observatory and Earthquake Research Institute (KOERI) seismic stations. The inset in (c) shows the total $\Delta\sigma_c$ for the Prince Islands segment in 2005 (black thick line), when the 1963 Cinarcik event is not considered (grey thick line), the coseismic contribution from the 1999 Izmit shock (black thin line), the contribution from viscoelastic relaxation (red line) and the changes corresponding to 10 years of tectonic loading (blue line).*

laxation should be taken into account in studies focusing on the state of the Coulomb stress field in this region.

Most of the NAF in the Marmara Sea is currently strongly loaded ($\Delta\sigma_c \geq 0.3$ MPa), and the whole region displays $\Delta\sigma_c$ values up to 1 MPa. These results agree with those of Hubert-Ferrari et al. (2000). Their study also shows that aftershocks immediately after the 1999 Izmit event are absent in the area where the 1963 Cinarcik earthquake released stress. We find that the combined effect of the 1999 Izmit earthquake, tectonic loading and viscoelastic relaxation erased in the mean time any possible stress shadow around the area where the 1963 Cinarcik event took place (Fig. 5.9a). The fact that local seismicity between 2000 and 2004 does not show any noticeable decrease in this area reflects this change in the Coulomb stress field between 1999 and the present date.

When the effects of the 1963 event are not considered, Coulomb stress changes on the Prince Islands segment range from 0.73 to 2.68 MPa (Fig. 5.9c, inset). Coseismic stress changes due to the 1999 Izmit earthquake range from 0.08 to 1.93 MPa, which is higher in the eastern end than the values estimated by Hubert-Ferrari et al. (2000, 0-0.5 MPa) or Parsons (2004, 0.02-0.760 MPa). Hubert-Ferrari et al. (2000) considered a 1999 Izmit rupture surface shorter to the west than that suggested by later studies (Reilinger et al., 2000; Wright et al., 2001). Parsons (2004) considered different slip distributions for the 1999 Izmit rupture surface, other than the one used in the present study (Wright et al., 2001). More detailed slip distributions (Reilinger et al., 2000; Delouis et al., 2002) suggest less slip to the western end of the 1999 Izmit rupture, so that Coulomb stress change in the immediacy of the fault's end would also be proportionally smaller. However, there is still no agreement on the slip distribution of the 1999 Izmit earthquake (Reilinger et al., 2000; Bouchon et al., 2002; Delouis et al., 2002). In addition, the effect from details of the slip distribution vanish with distance from the rupture. Pollitz and Sacks (2002) found that the static stress pattern around the 1992 Landers rupture was sensitive to the choice of the slip model, but the post-seismic stress change depended little on this choice. The use of a simple slip model for the present study is therefore justified.

Ten years of tectonic loading causes a stress increase of 0.08 MPa along the Prince Islands segment (Fig. 5.9c, inset, blue line). Sixty six years of tectonic loading plus the coseismic effect of the 1999 Izmit earthquake create 0.52-2.37 MPa, which is comparable to the 0.5-1 MPa obtained by Utkucu et al. (2003) using the slip distribution model of Delouis et al. (2002). The contribution due to the post-seismic viscoelastic relaxation between 1999 and 2005 (Fig. 5.9c, inset, red line) ranges from 0.12 to 0.27 MPa, equivalent to 15 to 35 years of tectonic loading.

5.7 Conclusions

Our analysis presents several improvements in relation to previous works. We consider a whole sequence of earthquakes instead of single pairs of events, we used a horizontally stratified medium and included the time-dependent effects of viscoelastic relaxation. Our results show that the effects of the latter are comparable or even greater in magnitude than the stress changes induced by steady tectonic loading during the inter-seismic phase of the earthquake cycle (Figs. 5.5, 5.6 and 5.9). Viscoelastic relaxation should therefore not be neglected.

The Coulomb stress failure criterion provides good results in this area and for this sequence of events, but considering only elastic stress changes can neglect an important part of the actual stress increase/decrease. For the case of the Marmara Sea region, the current rate of stress loading is governed by viscoelastic relaxation rather than tectonic loading. Accordingly, this result should be taken into account by seismic hazard-assessment studies in this region.

There is the possibility that our modeling approach is still too coarse for these events or this region, and that a more exhaustive analysis should be carried out, taking into account a more detailed geometry and slip distribution for the events and/or additional information about the rheological properties of the lower crust and upper mantle in the area. Nevertheless, it is improbable that the importance of the viscoelastic relaxation shown here would decrease considerably when including more detailed model parameters. The viscoelastic relaxation process should therefore be considered when analyzing time-dependent deformation-related data.

Chapter 6

Summary and conclusions

In this thesis, results dealing with the time-dependent crustal deformation after strong earthquakes have been presented. The method used for the calculations was described, together with several modifications to improve the speed and accuracy of the calculations. The software that applies the methodology was used to carry out a sensitivity analysis to assess the influence that different input parameters have on the modeled displacement field: The effect of three different variables (lithospheric thickness, asthenospheric viscosity and the dip angle of the fault) was analyzed in detail for the co- and post-seismic deformation due to thrust events. We found that the dip angle has a strong influence on the co-seismic deformation, but a less important one on the post-seismic displacements. The lithospheric thickness and asthenospheric viscosity, on the contrary, influence the post-seismic deformation more strongly than the co-seismic one. The region where the deformation is larger is in general the most suitable for ascertaining the most likely value for the latter two parameters.

The application to real deformation data was twofold. First, we considered GPS observations from surveys conducted in 1994 and 1996 at sites located close to the area of the great 1960 Chilean earthquake. These observations are not consistent with deformation caused by plate motion, but show anomalous seaward velocities for the inland stations. We reproduced the first-order pattern of the observed deformation, including the observed anomalous seaward movement. According to our study, the 1960 earthquake is the most likely cause for the velocity component that cannot be explained by plate convergence. Our model also predicts that this deformation will still be measurable for several more decades.

Also for this region, we derived the most likely values for some of the medium and source parameters involved in the deformation process by means of a grid search inversion over more than a million different models. The parameters studied were viscosity, thickness of the elastic layer, average slip on the rupture surface and the seismic coupling coefficient. According to the sensitivity analysis, the influence of the dip angle on the post-seismic deformation field is small. For this reason, we fixed the value of this parameter, using results from previous studies of this region, and excluded it from the inversion. The observations unfortunately did not cover the area of maximum displacements, which was identified by the sensitivity analysis as the most appropriate to find information about viscosity and thickness of the elastic layer. However, we obtained well-constrained estimates for these two variables, which agree with the strong sensitivity of the modeled post-seismic deformation found to two parameters.

The obtained estimate for these parameters is consistent with those of previous works, but our study provided a narrower range of possible values. Specifically, according to our error propagation analysis, the estimate for the viscosity in this area is stable and reliable when considered independent from the other parameters. However, we found a trade off between viscosity and average coseismic slip on the rupture surface, hence higher viscosities, in combination with larger coseismic slip values, must also be regarded as possible.

The second application was the study of the evolution of the Coulomb stress field along the North Anatolian Fault zone, considering the effects of 10 magnitude $M_s > 6.5$ earthquakes that have taken place there since 1939. We investigated the triggering of these events by stress transfer in a way that presented several improvements in relation to previous works: We considered a whole sequence of earthquakes instead of single pairs of events, we used a horizontally stratified medium and, most importantly, we included the time-dependent effects of viscoelastic relaxation. Our results show that the effects of the latter are comparable or even greater in magnitude than the stress changes induced by steady tectonic loading during the inter-seismic phase of the earthquake cycle. For the Marmara Sea region, the current rate of stress loading is governed by viscoelastic relaxation rather than tectonic loading. Also, we concluded that the Coulomb stress failure criterion provides good results in this area and for this sequence of events, but considering only elastic stress changes would neglect an important part of the actual stress increase/decrease.

The results compiled in this thesis provide evidence that PSGRN/PSCMP, the programs that use the methodology presented, are a very powerful tool for calculating the co- and post-seismic deformation induced by earthquakes in a multi-layered viscoelastic-gravitational half-space. They provide a combination of speed, accuracy and flexibility hardly equalled by any other available program.

Our sensitivity analysis, the inversion for the area around the 1960 Chilean earthquake and the prediction about the future measurability of the deformation are potentially useful when planning future geodetic campaigns or when a numerical inversion is carried out. We also showed that the effects on the deformation (displacement or stress field) of viscoelastic relaxation after a strong event are measurable, and can be observed far away from the epicentral area and long after the event. Therefore, to neglect viscoelastic relaxation is not an acceptable simplification when analyzing time-dependent crustal deformation after a strong earthquake.

Bibliography

Alsan, E., Tezucan, L., Båth, M., 1976. An earthquake catalogue for Turkey for the interval 1913-1970. Tectonophysics 31 (1-2), T13–T19.

Álvarez, L., 1963. Studies made between Arauco and Valdivia with respect to the earthquake of 21 and 22 May 1960. Bull. Seism. Soc. Am. 53 (6), 1315–1330, translated and abridged by Pierre Saint-Amand.

Ambraseys, N., 2002. The seismic activity of the Marmara Sea region over the last 2000 years. Bull. Seism. Soc. Am. 92 (1), 1–18.

Ambraseys, N. N., 1970. Some characteristic features of the Anatolian fault zone. Tectonophys. 9, 143–165.

Ambraseys, N. N., Finkel, C. F., 1991. Long-term seismicity of Istanbul and the Marmara Sea region. Terra Nova 3, 527–539.

Ambraseys, N. N., Finkel, C. F., 1995. The Seismicity of Turkey and Adjacent Areas - A Historical Review, 1500-1800. M. S. Eren Publications and Books, Istanbul.

Ambraseys, N. N., Jackson, J. A., 2000. Seismicity of the Sea of Marmara (Turkey) since 1500. Geophys. J. Int. 141 (3), F1–F6.

Ambraseys, N. N., Zatopek, A., 1969. The Mudurnu Valley, West Anatolia, Turkey earthquake of 22 July, 1967. Bull. Seism. Soc. Am. 59, 521–589.

Angermann, D., Klotz, J., Reigber, C., 1999. Space-geodetic estimation of the Nazca-South America Euler vector. Earth and Planetary Science Letters 171, 329–334.

Araujo, M., Suárez, G., 1994. Geometry and state of stress of the subducted Nazca plate beneath central Chile and Argentina: Evidence from teleseismic data. Geophys. J. Int. 116, 283–303.

Armijo, R., Flerit, F., King, G., Meyer, B., 2003. Linear elastic fracture mechanics explains the past and present evolution of the Aegean. Earth planet. Sci. Lett. 217 (1-2), 85–95, doi: 10.1016/S0012-821X(03)00590-9.

Armijo, R., Pondard, N., Meyer, B., Uçarkus, G., de Lépinay, B. M., Malavieille, J., Dominguez, S., Gustcher, M.-A., Schmidt, S., Beck, C., Çagatay, N., Çakir, Z., Imren, C., Eris, K., Natalin, B., Özalaybey, S., Tolun, L., Lefèvre, I., Seeber, L., Gasperini, L., Rangin, C., Emre, O., Sarikavak, K., 2005. Submarine fault scarps in the Sea of Marmara pull-apart (North Anatolian Fault): Implications for seismic hazard in Istanbul. Geochem. Geophys. Geosyst. 6 (6), 1–29, citation no. Q06009, doi: 10.1029/2004GC000896.

Askew, B. L., Algermissen, S. T., 1985. Catalog of earthquakes for South America: hypocenter and intensity data 4, 6 and 7a, b and c, online Data Set available from USGS National Earthquake Information Center: http://wwwneic.cr.usgs.gov/neis/epic/epic.html.

Ayhan, M. E., Bürgmann, R., McClusky, S., Lenk, O., Aktug, B., Herece, E., Reilinger, R. E., 2001. Kinematics of the Mw = 7.2, 12 November 1999, Düzce, Turkey earthquake. Geophys. Res. Lett. 28 (2), 367–370.

Barka, A., 1996. Slip distribution along the North Anatolian fault associated with large earthquakes of the period 1939-1967. Bull. Seism. Soc. Am. 86, 1238–1254.

Barka, A., Akyüz, H. S., Altunel, E., Sunal, G., Çakir, Z., Dikbaş, A., Yerli, B., Armijo, R., Meyer, B., Chabalier, J. B., Rockwell, T., Dolan, J. R., Hartleb, R., Dawson, T., Christofferson, S., Tucker, A., Fumal, T., Langridge, R., Stenner, H., Lettis, W., Bachhuber, J., Page, W., 2002. The surface rupture and slip distribution of the 17 August 1999 Izmit earthquake (M 7.4), North Anatolian fault. Bull. Seism. Soc. Am. 92 (1), 43–60.

Barka, A., Kadinsky-Cade, K., 1988. Strike-slip fault geometry in Turkey and its influence on earthquake activity. Tectonics 7, 663–684.

Barrientos, S. E., Plafker, G., Lorca, E., 1992. Postseismic coastal uplift in Southern Chile. Geophys. Res. Lett. 19, 701–704.

Barrientos, S. E., Ward, S. N., 1990. The 1960 Chile earthquake: inversion for slip distribution from surface deformation. Geophys. J. Int. 103, 589–598.

Beeler, N. M., Simpson, R. W., Hickman, S. H., Lockner, D. A., 2000. Pore fluid pressure, apparent friction, and Coulomb failure. J. Geophys. Res. 105 (B11), 25,533–25,542.

Belardinelli, M. E., Bizzarri, A., Cocco, M., 2003. Earthquake triggering by static and dynamic stress changes. J. Geophys. Res. 108 (B3), ESE 1–1 to ESE 1–16, citation no. 2135, doi: 10.1029/2002JB001779.

Belardinelli, M. E., Cocco, M., Coutant, O., Cotton, F., 1999. Redistribution of dynamic stress during coseismic ruptures: Evidence for fault interaction and earthquake triggering. Journal of Geophysical Research 104 (B7), 14925–14945.

Ben-Menahem, A., Gillon, A., 1970. Crustal deformations by earthquakes and explosions. Bull. Seism. Soc. Am. 60, 193–215, for remark on misprints see: Jovanovich et al., Geophys. J. R. astr. Soc. (1974), vol. 39, p. 210.

Ben-Menahem, A., Israel, M., 1970. Effects of major seismic events on the rotation of the Earth. Geophys. J. R. astrom. Soc. 19, 367–393.

Ben-Menahem, A., Singh, S. J., 1968. Multipolar elastic fields in a layered half-space. Bulletin of the Seismological Society of America 58, 1519–1572, for remark on misprints see: Jovanovich, Husseini and Chinnery, Geophysical Journal of the Royal astronomical Society 39, 210, 1974.

Benioff, H., Press, F., Smith, S., 1961. Excitation of the free oscillations of the Earth by earthquakes. J. Geophys. Res. 66 (2), 605–619.

Bohm, M., Lüth, S., Echtler, H., Asch, G., Bataille, K., Bruhn, C., Rietbrock, A., Wigger, P., 2002. The Southern Andes between 36° and 40° latitude: seismicity and average seismic velocities. Tectonophysics 356, 275–289.

Bonafede, M., 1990. Axi-symmetric deformation of a thermo-poro-elastic half-space: Inflation of a magma chamber. Geophys. J. Int. 103, 289–299.

Bonafede, M., Rivalta, E., 1999. The tensile dislocation problem in a layered elastic medium. Geophysical Journal International 136 (2), 341–356.

Bouchon, M., Toksöz, M. N., Karabulut, H., Bouin, M.-P., Dietrich, M., Aktar, M., 2002. Imaging of the Izmit rupture from the strong motion records. In: Görür, N., Papadopoulos, G. A., Okay, N. (Eds.), Integration of Earth Science Research on the Turkish and Greek 1999 Earthquakes. NATO Science Series: IV. Earth and Environmental Sciences - Vol. 9. Kluwer, Dordrecht, pp. 17–34.

Bracewell, R., 1965. The Fourier Transform and its Applications. McGraw-Hill, New York.

Braslau, D., Lieber, P., 1968. Three-dimensional fields due to a Volterra dislocation embedded in a layered half-space: analytical representation of a seismic mechanism. Bull. Seism. Soc. Am. 58, 613–628.

Brown, L., Reilinger, R., Holdhal, S. R., Balazs, E. I., 1977. Postseismic crustal uplift near Anchorage, Alaska. J. Geophys. Res. 82, 3369–3378.

Bürgmann, R., Ergintav, S., Segall, P., Hearn, E. H., McClusky, S., Reilinger, R. E., Woith, H., Zschau, J., 2002. Time-dependent distributed afterslip on and deep below the Izmit earthquake rupture. Bull. Seism. Soc. Am. 92 (1), 126–137.

Byerlee, J. D., Wyss, M., 1978. Rock Friction and Earthquake Prediction. Pageoph (spec. iss.) 116, 583–991.

Cahill, T., Isacks, B. L., 1992. Seismicity and shape of the subducted Nazca plate. J. Geophys. Res. 97 (B12), 17503–17529.

Çakir, Z., de Chabalier, J.-B., Armijo, R., Meyer, B., Barka, A., Peltzer, G., 2003. Coseismic and early post-seismic slip associated with the 1999 Izmit earthquake (Turkey), from SAR interferometry and tectonic field observations. Geophysical Journal International 155 (1), 93–110.

Casarotti, E., Piersanti, A., 2003. Postseismic stress diffusion in Chile and South Peru. Earth planet. Sci. Lett. 206 (3-4), 325–333, doi: 10.1016/S0012-821X(02)01103-2.

Chase, C., 1978. Plate kinematics: The Americas, East Africa, and the rest of the world. Earth planet. Sci. Lett. 37, 355–368.

Christensen, R. M., 1971. Theory of Viscoelasticity: An Introduction. Academic, New York, second edn.

Cifuentes, I. L., Silver, P. G., 1989. Low-frequency source characteristics of the great 1960 Chilean Earthquake. J. Geophys. Res. 94, 643–663.

Cocco, M., Rice, J. R., 2002. Pore pressure and poroelasticity effects in Coulomb stress analysis of earthquake interactions. J. Geophys. Res. 107 (B2), ESE 2–1 to ESE 2–17, correction in JGR 108(B2), ESE 2-1, 2069, doi: 10.1029/2002JB002319; this article: citation number 2030, DOI: 10.1029 / 2000JB000138.

Cohen, S. C., 1980a. Postseismic viscoelastic deformation and stress - 2. Stress theory and computation; dependence of displacement, strain, and stress on fault parameters. J. Geophys. Res. 85, 3151–3158.

Cohen, S. C., 1980b. Postseismic viscoelastic surface deformation and stress - 1. Theoretical considerations, displacement and strain calculations. J. Geophys. Res. 85, 3131–3150.

Cohen, S. C., 1982. A multilayer model of time dependent deformation following an earthquake on a strike slip fault. J. Geophys. Res. 87, 5409–5421.

Cohen, S. C., 1994. Evaluation of the importance of model features for cyclic deformation due to dipslip faulting. Geophys. J. Int. 119, 831–841.

Conrad, C. P., Bilek, S., Lithgow-Bertelloni, C., 2004. Great earthquakes and slab pull: interaction between seismic coupling and plate-slab coupling. Earth planet. Sci. Lett. 218 (1-2), 109–122.

Delouis, B., Giardini, D., Lundgren, P., Salichon, J., 2002. Joint inversion of InSAR, GPS, teleseismic, and strong-motion data for the spatial and temporal distribution of earthquake slip: application to the 1999 Izmit mainshock. Bull. Seism. Soc. Am. 92 (1), 278–299.

DeMets, C., Gorden, R. G., Argus, D. F., Stein, S., 1994. Effect of recent revisions to the geomagnetic reversal timescale on estimates of current plate motion. Geophys. Res. Lett. 21, 2191–2194.

DeMets, C., Gordon, R. G., Argus, D. F., Stein, S., 1990. Current plate motions. Geophys. J. Int. 101, 425–478.

Deng, J., Gurnis, M., Kanamori, H., Hauksson, E., 1998. Viscoelastic flow in the lower crust after the 1992 Landers, California, earthquake. Science 282 (5394), 1689–1692.

Deng, J., Hudnut, K., Gurnis, M., Hauksson, E., 1999. Stress loading from viscous flow in the lower crust and triggering of aftershocks following the 1994 Northridge, California, earthquake. Geophys. Res. Lett. 26 (21), 3209–3212.

Dewey, J. W., 1976. Seismicity of northern Anatolia. Bull. Seism. Soc. Am. 66, 843–868.

Dunkin, J. W., 1965. Computation of modal solutions in layered elastic media at high frequencies. Bulletin of the Seismological Society of America 55, 335–358.

Dziewonski, A., Anderson, D. L., 1981. Preliminary reference earth model. Phys. Earth Planet. Inter. 25, 297–356.

Farrell, W. E., 1972. Deformation of the earth by surface loads. Rev. Geophys. Space Phys. 10 (3), 761–797.

Fernández, J., Rundle, J. B., 1994a. Fortran program to compute displacement, potential, and gravity changes resulting from a magma intrusion in a multilayered Earth model. Computers & Geosciences 20, 461–510.

Fernández, J., Rundle, J. B., 1994b. Gravity changes and deformation due to a magmatic intrusion in a two-layered crustal model. J. Geophys. Res. 99 (B2), 2737–2746.

Fernández, J., Rundle, J. B., 2004. Postseismic viscoelastic-gravitational half space computations: Problems and solutions. Geophys. Res. Lett. 31 (7), citation no. L07608, doi: 10.1029/2004GL019654.

Fernández, J., Rundle, J. B., Granell, R. D. R., Yu, T.-T., 1997. Programs to compute deformation due to a magma intrusion in elastic-gravitational layered earth models. Computers & Geosciences 23 (3), 231–249.

Fernández, J., Tiampo, K. F., Rundle, J. B., 2001. Viscoelastic displacement and gravity changes due to point magmatic intrusions in a gravitational layered solid earth. Geophys. J. Int. 146 (1), 155–170.

Fernández, J., Yu, T.-T., Rundle, J. B., 1996a. Deformation produced by a rectangular dipping fault in a viscoelastic-gravitational layered Earth model - Part I: Thrust fault FLTGRV and FLTGRH FORTRAN programs. Computers & Geosciences 22, 735–750, corrigenda in C&G 25 (3), 301-7, 1999.

Fernández, J., Yu, T.-T., Rundle, J. B., 1996b. Horizontal viscoelastic-gravitational displacement due to a rectangular dipping thrust fault in a layered Earth model. J. Geophys. Res. 101, 13,581–13,594, corrigenda in JGR, 103, B12, 30,283-6, 1998.

Fialko, Y., 2004. Evidence of fluid-filled upper crust from observations of postseismic deformation due to the 1992 M_w 7.3 Landers earthquake. J. Geophys. Res. 109 (B8), citation no. B08401, doi: 10.1029/2004JB002985.

Fitch, T. J., Scholz, C. H., 1971. Mechanism of underthrusting in southwest Japan: A model of convergent plate interactions. J. Geophys. Res. 76, 7260–7292.

Flerit, F., Armijo, R., King, G., Meyer, B., 2004. The mechanical interaction between the propagating North Anatolian Fault and the back-arc extension in the Aegean. Earth planet. Sci. Lett. 224 (3-4), 347–362, doi: 10.1016/j.epsl.2004.05.028.

Flerit, F., Armijo, R., King, G. C. P., Meyer, B., Barka, A., 2003. Slip partitioning in the Sea of Marmara pull-apart determined from GPS velocity vectors. Geophysical Journal International 154 (1), 1–7.

Folch, A., Fernández, J., Rundle, J. B., Martí, J., 2000. Ground deformation in a viscoelastic medium composed of a layer overlying a half-space: a comparison between point and extended sources. Geophys. J. Int. 140 (1), 37–50.

Freed, A. M., 2005. Earthquake triggering by static, dynamic and postseismic stress transfer. Annual Review of Earth and Planetary Sciences 33, 335–367.

Freed, A. M., Bürgmann, R., 2004. Evidence of power-law flow in the Mojave desert mantle. Nature 430 (6999), 548–551.

Freed, A. M., Lin, J., 2001. Delayed triggering of the 1999 Hector Mine earthquake by viscoelastic stress transfer. Nature 411 (6834), 180–183, see also: E. Harding Hearn, Nature, same issue, p. 150.

Freymueller, J. T., Cohen, S. C., Fletcher, H. J., 2000. Spatial variations in present-day deformation, Kenai Peninsula, Alaska, and their implications. J. Geophys. Res. 105 (B4), 8079–8102, doi: 10.1029/1999JB900388.

Gokaşan, E., Ustaömer, T., Gazioğlu, C., Yucel, Z. Y., Öztürk, K., Tur, H., Ecevitoğlu, B., Tok, B., 2003. Morpho-tectonic evolution of the Marmara Sea inferred from multi-beam bathymetric and seismic data. Geo-Marine Letters 23 (1), 19–33.

Grosser, H., Baumbach, M., Berckhemer, H., Baier, B., Karahan, A., Schelle, H., Krüger, F., Paulat, A., Michel, G., Demirtaş, R., Gencoğlu, S., Yılmaz, R., 1998. The Erzincan (Turkey) earthquake (M_s 6.8) of March 13, 1992 and its aftershock sequence. Pageoph 152, 465–505.

Hardebeck, J. L., 2004. Stress triggering and earthquake probability estimates. J. Geophys. Res. 109 (B4), citation no. B04310, doi: 10.1029/2003JB002437.

Harris, R. A., 1998. Introduction to special section: Stress triggers, stress shadows, and implications for seismic hazard. Journal of Geophysical Research 103 (B10), 24347–24358.

Harris, R. A., Simpson, R. W., Reasenberg, P. A., 1995. Influence of static stress changes on earthquake locations in southern California. Nature 375 (6528), 221–224.

Haskell, N. A., 1953. The dispersion of surface waves on multilayered media. Bull. Seism. Soc. Am. 43, 17–34.

Healy, J. H., Rubey, W. W., Griggs, D. T., Raleigh, C. B., 1968. The Denver earthquakes. Science 161, 1301–1310.

Hearn, E. H., Hager, B. H., Reilinger, R. E., 2002. Viscoelastic deformation from North Anatolian fault zone earthquakes and the eastern Mediterranean GPS velocity field. Geophys. Res. Lett. 29 (11), 44–1 to 44–4, citation no. 1549, doi: 10.1029/2002GL014889.

Horasan, G., Gülen, L., Pınar, A., Kalafat, D., Özel, N., Kuleli, H. S., Işıkara, A. M., 2002. Lithospheric structure of the Marmara and Aegean regions, western Turkey. Bull. Seism. Soc. Am. 92 (1), 322–329.

Hu, Y., Wang, K., He, J., Klotz, J., Khazaradze, G., 2004. Three-dimensional viscoelastic finite element model for postseismic deformation of the great 1960 Chile earthquake. J. Geophys. Res. 109 (B12), citation no. B12403, doi: 10.1029/2004JB003163.

Hubert-Ferrari, A., Barka, A., Jacques, E., Nalbant, S. S., Meyer, B., Armijo, R., Tapponnier, P., King, G. C. P., 2000. Seismic hazard in the Marmara Sea region following the 17 August 1999 Izmit earthquake. Nature 404 (6775), 269–273.

Jackson, J., McKenzie, D., 1988. The relationship between plate motions and seismic moment tensors, and the rates of active deformation in the Mediterranean and Middle East. Geophys. J. 93, 45–73.

Jacobs, A., Sandwell, D., Fialko, Y., Sichoix, L., 2002. The 1999 (Mw 7.1) Hector Mine, California, earthquake: near-field postseismic deformation from ERS interferometry. Bull. Seism. Soc. Am. 92 (4), 1433–1442, spec. iss.: The Hector Mine, California, Earthquake, ed. by Michael J. Rymer, Victoria E. Langenheim, and Egill Hauksson.

James, T. S., Clague, J. J., Wang, K., Hutchinson, I., 2000. Postglacial rebound at the northern Cascadia subduction zone. Quaternary Science Reviews 19, 1527–1541.

Jónsson, S., Segall, P., Pedersen, R., Björnsson, G., 2003. Post-earthquake ground movements correlated to pore-pressure transients. Nature 424 (6945), 179–183, doi: 10.1038/nature01776.

Jordan, T. E., Isacks, B. L., Allemendinger, R. W., Ramos, J. A., Ando, C. J., 1983. Andean tectonics related to geometry of subducted Nazca plate. Geological Study of America Bulletin 94, 341–361.

Jovanovich, D. B., Husseini, M. I., Chinnery, M. A., 1974a. Elastic dislocations in a layered half-space - I. Basic theory and numerical methods. Geophys. J. R. astr. Soc. 39, 205–217, for remark on misprints see: Roth, Geophys. J. Int.(1990), vol. 103, p. 155.

Jovanovich, D. B., Husseini, M. I., Chinnery, M. A., 1974b. Elastic dislocations in a layered half-space - II. The point source. Geophys. J. R. astr. Soc. 39, 219–239.

Kanamori, H., 1977. Energy release in great earthquakes. J. Geophys. Res. 82, 2981–2987.

Kanamori, H., Cipar, J. J., 1974. Focal process of the great Chilean earthquake May 22, 1960. Phys. Earth Plan. Int. 9, 128–136.

Karahan, A. E., Berckhemer, H., Baier, B., 2001. Crustal structure at the western end of the North Anatolian fault zone from deep seismic sounding. Annali di Geofisica 44 (1), 49–68.

Kasahara, K., 1975. Aseismic faulting following the 1973 Nemuro-oki earthquake, Hokkaido, Japan (A possibility). Pageoph 113, 127–139.

Kaypak, B., Eyidoğan, H., 2005. One-dimensional crustal structure of the Erzincan basin, Eastern Turkey and relocations of the 1992 Erzincan earthquake (Ms=6.8) aftershock sequence. Phys. Earth Plan. Int. 151 (1-2), 1–20, doi: 10.1016/j.pepi.2004.11.009.

Khazaradze, G., Klotz, J., 2003. Short- and long-term effects of GPS measured crustal deformation rates along the south central Andes. J. Geophys. Res. 108 (B6), ETG 5–1 to ETG 5–15, citation no. 2289, doi: 10.1029/2002JB001879.

Khazaradze, G., Wang, K., Klotz, J., Hu, Y., He, J., 2002. Prolonged postseismic deformation of the 1960 great Chile earthquake and implications for mantle rheology. Geophys. Res. Lett. 29 (22), 7–1 to 7–4, citation no. 2050, doi: 10.1029/2002GL015986.

Kind, R., Bock, G., Yuan, X., 2001. The structure of the lower plate from broadband seismology. Report for the period 1999-2001, SFB 267 (Collaborative Research Center ”Deformation processes in the Andes - Interaction between endogenic and exogenic processes during subduction orogenesis”) .

Kind, R., Seidl, D., 1982. Analysis of broadband seismograms from the Chile-Peru area. Bull. Seism. Soc. Am. 72, 2131–2145.

King, G., Cocco, M., 2001. Fault interaction by elastic stress change: new clues from earthquake sequence. Advances in Geophysics 44, 1–38.

King, G. C. P., Stein, R. S., Lin, J., 1994. Static stress changes and the triggering of earthquakes. Bull. Seism. Soc. Am. 84, 935–953.

Klotz, J., Khazaradze, G., Angermann, D., Reigber, C., Perdomo, R., Cifuentes, O., 2001. Earthquake cycle dominates contemporary crustal deformation in Central and Southern Andes. Earth and Planetary Science Letters 193 (3-4), 437–446.

KOERI, 2005. Recent earthquakes in Turkey. Kandilli Observatory and Earthquake Research Institute, http://www.koeri.boun.edu.tr/sismo/ defaulteng.htm; 30.06.05.

Kondo, H., Awata, Y., Yoshioka, T., Emre, O., Doğan, A., Özalp, S., Tokay, F., Yιldιrιm, C., Okumura, K., 2005. Slip distribution, fault geometry, and fault segmentation of the 1944 Bolu-Gerede earthquake rupture, North Anatolian fault, Turkey. Bulletin of the Seismological Society of America 95 (4), 1234–1249.

Krawczyk, C., the SPOC team, 2003. Amphibious seismic survey images plate interface at 1960 Chile earthquake. Eos, Trans., Am. Geophys. Un. 84 (32), 301, 304 & 305.

Lambeck, K., 1980. The Earth’s Variable Rotation: Geophysical Causes and Consequences. Cambridge University Press, London.

Lay, T., Kanamori, H., 1981. An asperity model of large earthquake sequences. In: Simpson, D., Richards, P. (Eds.), Earthquake Prediction. No. 4 in Maurice Ewing Series. AGU, Washington, D.C., pp. 579–592.

Le Pichon, X., Şengör, A. M. C., Demirbağ, E., Rangin, C., Imren, C., Armijo, R., Görür, N., Çağatay, N., Mercier de Lepinay, B., Meyer, B., Saatcılar, R., Tok, B., 2001. The active Main Marmara Fault. Earth and Planetary Science Letters 192 (4), 595–616.

Lin, J., Stein, R. S., 2004. Stress triggering in thrust and subduction earthquakes and stress interaction between the southern San Andreas and nearby thrust and strike-slip faults. J. Geophys. Res. 109 (B2), citation no. B02303, doi: 10.1029/2003JB002607.

Linde, A. T., Silver, P. G., 1989. Elevation changes and the Great 1960 Chilean earthquake: Support for aseismic slip. Geophys. Res. Lett. 16, 1305–1308.

Longman, I. M., 1963. A Green's function for determining the deformation of the Earth under surface loads II: computations and numerical results. J. Geophys. Res. 68, 485–496.

Love, A. E. H., 1911. Some Problems of Geodynamics. Cambridge Univ. Press, Cambridge.

Lüth, S., Lueth, S., Wigger, P., 2003. A crustal model along 39 °S from a seismic refraction profile - ISSA 2000. Revista geológica de Chile 30 (1), 83–101.

Ma, K.-F., Chan, C.-H., Stein, R., 2005. Response of seismicity to Coulomb stress triggers and shadows of the 1999 Mw=7.6 Chi-Chi, Taiwan, earthquake. J. Geophys. Res. 110 (5), B05S19.

Ma, X.-Q., Kusznir, N. J., 1992. 3-D subsurface displacement and strain fields for faults and fault arrays in a layered elastic half-space. Geophys. J. Int. 111, 542–558.

Ma, X.-Q., Kusznir, N. J., 1994a. Coseismic and postseismic subsurface displacements and strains for a vertical strike-slip fault in a three-layer elastic medium. Pageoph 142, 687–709.

Ma, X.-Q., Kusznir, N. J., 1994b. Effects of rigidity layering, gravity and stress relaxation on 3-D subsurface fault displacement fields. Geophys. J. Int. 118, 201–220.

Ma, X.-Q., Kusznir, N. J., 1995. Coseismic and postseismic subsurface displacements and strains for a dip-slip normal fault in a three-layer elastic-gravitational medium. J. Geophys. Res. 100, 12813–12830.

Matsu'ura, M., Sato, R., 1975. Static deformations due to the fault spreading over several layers in a multilayered medium. Part II. Strain and tilt. J. Phys. Earth 23, 1–29.

McCloskey, J., Nalbant, S., Steacy, S., 2005. Earthquake risk from co-seismic stress. Nature 434 (7031), 291.

McClusky, S., Balassanian, S., Barka, A., Demir, A., Ergintav, S., Georgiev, I., Gurkan, O., Hamburger, M., Hurst, K., Kahle, H., Kastens, K., Kekelidze, G., King, R., Kotzev, V., Lenk, O., Mahmoud, S., Mishin, A., Nadariya, M., Ouzounis, A., Paradissis, D., Peter, Y., Prilepin, M., Reilinger, R., Sanlı, I., Seeger, H., Tealeb, A., Toksöz, M. N., Veis, G., 2000. Global Positioning System constraints on plate kinematics and dynamics in the eastern Mediterranean and Caucasus. J. Geophys. Res. 105 (B3), 5695–5719.

McKenzie, D. P., 1972. Active tectonics of the Mediterranean region. Geophys. J. R. astr. Soc. 30, 109–185.

Metropolis, N., Ulam, S., 1949. The Monte Carlo Method. J. Amer. Stat. Assoc. 44, 335–341.

Milkereit, C., Grosser, H., Wang, R., Wetzel, H.-U., Woith, H., Karakısa, S., Zünbül, S., Zschau, J., 2004. Implications of the 2003 Bingöl earthquake for the interaction between the North and East Anatolian faults. Bull. Seism. Soc. Am. 94 (6), 2400–2406.

Milkereit, C., Zünbül, S., Karakısa, S., Iravul, Y., Zschau, J., Baumbach, M., Grosser, H., Günther, E., Umutlu, N., Kuru, T., Erkul, E., Klinge, K., Ibs-von Seht, M., Karahan, A., 2000. Preliminary aftershock analysis of the Mw=7.4 Izmit and Mw=7.1 Düzce earthquake in western Turkey. In: Barka, A., Kozacı, Ö., Akyüz, S., Altunel, A. (Eds.), The 1999 Izmit and Düzce Earthquakes: preliminary results. Istanbul Technical University, pp. 179–187.

Mogi, K., 1968. Migration of seismic activity. Bull. Earthq. Res. Inst. 46, 53–74.

Montesi, L. G. J., 2004. Postseismic deformation and the strength of ductile shear zones. Earth Planet Space 56, 1135–1142.

Morelli, A., Bonafede, M., Dragoni, M., 1987. Two-dimensional crack model of faulting in a layered elastic half-space. Ann. Geophys. 5B, 281–288.

Muller, J. R., Aydin, A., Maerten, F., 2003. Investigating the transition between the 1967 Mudurnu Valley and 1999 Izmit earthquakes along the North Anatolian fault with static stress changes. Geophysical Journal International 154 (2), 471–482.

Nalbant, S., Steacy, S., McCloskey, J., Sieh, K., Natawidjaja, D., 2005a. Earthquake risk on the Sunda trench. Nature 435 (7043), 756–757.

Nalbant, S. S., Barka, A. A., Alptekin, Ö., 1996. Failure stress change caused by the 1992 Erzincan earthquake ($M_s = 6.8$). Geophys. Res. Lett. 23, 1561–1564.

Nalbant, S. S., Hubert, A., King, G. C. P., 1998. Stress coupling between earthquakes in northwest Turkey and the north Aegean Sea. Journal of Geophysical Research 103 (B10), 24469–24486.

Nalbant, S. S., McCloskey, J., Steacy, S., 2005b. Lessons on the calculation of the static stress loading from the 2003 Bingöl, Turkey earthquake. Earth and Planetary Science Letters 235, 632–640.

Nalbant, S. S., McCloskey, J., Steacy, S., Barka, A. A., 2002. Stress accumulation and increased seismic risk in eastern Turkey. Earth Planet. Sci. Lett. 195 (3-4), 291–298.

Nason, R., Weertman, J., 1973. A dislocation theory analysis of fault creep events. J. Geophys. Res. 78, 7745–7751.

Nishenko, S. P., 1985. Seismic potential for large and great interplate earthquakes along the Chilean and southern Peruvian margins of South America: A quantitative reappraisal. J. Geophys. Res. 90, 3589–3615.

Norabuena, E., Leffler-Griffin, L., Mao, A., Dixon, T., Stain, S., Sacks, S. I., Ocola, L., Ellis, M., 1998. Space geodetic observations of Nazca-South America convergence across the central Andes. Science 279, 358–362.

Norabuena, E. O., Dixon, T. H., Stein, S., Harrison, C. G. A., 1999. Decelerating Nazca-South America and Nazca-Pacific plate motions. Geophys. Res. Lett. 26 (22), 3405–3408.

Nostro, C., Chiaraluce, L., Cocco, M., Baumont, D., Scotti, O., 2005. Coulomb stress changes caused by repeated normal faulting earthquakes during the 1997 Umbria-Marche (central Italy) seismic sequence. J. Geophys. Res. 110 (5), B05S20.

Nur, A., Mavko, G., 1974. Postseismic viscoelastic rebound. Science 183, 204–206.

Okada, Y., 1992. Internal deformation due to shear and tensile faults in a half-space. Bull. Seism. Soc. Am. 82, 1018–1040.

Oleskevich, D. A., Hyndman, R. D., Wang, K., 1999. The updip and downdip limits to great subduction earthquakes: Thermal and structural models of Cascadia, south Alaska, SW Japan, and Chile. Journal of Geophysical Research 104 (B7), 14947–14991.

Parsons, T., 2004. Recalculated probability of M >= 7 earthquakes beneath the Sea of Marmara, Turkey. J. Geophys. Res. 109 (B5), citation no. B05304, doi: 10.1029/2003JB002667.

Parsons, T., Toda, S., Stein, R. S., Barka, A., Dieterich, J. H., 2000. Heightened odds of large earthquakes near Istanbul: an interaction-based probability calculation. Science 288 (5466), 661–665.

Peltzer, G., Rosen, P., Rogez, F., Hudnut, K., 1998. Poroelastic rebound along the Landers 1992 earthquake surface rupture. J. Geophys. Res. 103 (B12), 30,131–30,146.

Piersanti, A., 1999. Postseismic deformation in Chile: Constraints on the asthenospheric viscosity. Geophys. Res. Lett. 26 (20), 3157–3160.

Piersanti, A., Spada, G., Sabadini, R., 1997. Global postseismic rebound of a viscoelastic Earth: Theory for finite faults and application to the 1964 Alaska earthquake. J. Geophys. Res. 102, 477–492.

Pınar, A., Honkura, Y., Kikuchi, M., 1994. Rupture process of the 1992 Erzincan earthquake and its implication for seismotectonics in eastern Turkey. Geophysical Research Letters 21 (18), 1971–1974.

Pınar, A., Honkura, Y., Kuge, K., 2001. Seismic activity triggered by the 1999 Izmit earthquake and its implications for the assessment of future seismic risk. Geophys. J. Int. 146 (1), F1–F7.

Pinar, N., 1953. Etude géologique et macrosismique du tremblement du terre de Kurşunlu (Anatolie septentrionale) du 13 août 1951. Rev. Fac. Sc. Univ. Istanbul XVIII, 131–142.

Plafker, G., 1972. Alaskan earthquake of 1964 and Chilean earthquake of 1960: Implications for arc tectonics. J. Geophys. Res. 77, 901–925.

Plafker, G., Savage, J. C., 1970. Mechanism of the Chilean earthquakes of May 21 and 22, 1960. Geol. Soc. Am. Bull. 81 (4), 1001–1030.

Pollitz, F. F., 1997. Gravitational viscoelastic postseismic relaxation on a layered spherical Earth. J. Geophys. Res. 102 (B8), 17,921–17,941.

Pollitz, F. F., Bürgmann, R., Romanowicz, B., 1998. Viscosity of oceanic asthenosphere inferred from remote triggering of earthquakes. Science 280, 1245–1249.

Pollitz, F. F., Sacks, I. S., 2002. Stress triggering of the 1999 Hector Mine earthquake by transient deformation following the 1992 Landers earthquake. Bull. Seism. Soc. Am. 92 (4), 1487–1496, spec. iss.: The Hector Mine, California, Earthquake, ed. by Michael J. Rymer, Victoria E. Langenheim, and Egill Hauksson.

Pollitz, F. F., Wicks, C., Thatcher, W., 2001. Mantle flow beneath a continental strike-slip fault: Postseismic deformation after the 1999 Hector Mine earthquake. Science 293 (5536), 1814–1818.

Press, F., Ben-Menahem, A., Toksöz, M. N., 1961. Experimental determination of earthquake fault length and rupture velocity. J. Geophys. Res. 66 (10), 3471–3485.

Purcaru, G., Berckhemer, H., 1982. Regularity patterns and zones of seismic potential for future large earthquakes in the Mediterranean region. Tectonophys. 85, 1–30.

Raleigh, C. B., Healy, J. H., Bredehoeft, J. D., 1972. Faulting and crustal stress at Rangely, Colorado. In: Heard, H., Borg, I., Carter, N., Raleigh, C. (Eds.), Flow and Fracture of Rocks. Vol. 16 of Geophysical Monograph Series. Am. Geophys. Un., Washington, D. C., pp. 275–284.

Ranalli, G., 1995. Rheology of the Earth, 2nd Edition. Chapman & Hall, London.

Reasenberg, P. A., Simpson, R. W., 1992. Response of regional seismicity to the static stress change produced by the Loma Prieta earthquake. Science 255 (5052), 1687–1690.

Reid, H. F., 1910. The mechanics of the earthquake, the California earthquake of April 18, 1906. Report of the State Investigation Commission, Vol.2, Carnegie Institution of Washington, Washington, D.C.

Reilinger, R. E., Ergintav, S., Bürgmann, R., McClusky, S., Lenk, O., Barka, A., Gurkan, O., Hearn, E., Feigl, K. L., Cakmak, R., Aktug, B., Ozener, H., Toksöz, M. N., 2000. Coseismic and postseismic fault slip for the 17 August 1999, M = 7.5, Izmit, Turkey earthquake. Science 289 (5484), 1519–1523.

Rosenman, M., Singh, S. J., 1973a. Quasi-static strains and tilts due to faulting in a viscoelastic half-space. Bull. Seism. Soc. Am. 63, 1737–1752.

Rosenman, M., Singh, S. J., 1973b. Stress relaxation in a semi-infinite viscoelastic earth model. Bull. Seism. Soc. Am. 63, 2145–2154.

Roth, F., 1983. Oberflächendeformationen und Krustenspannungen in Erdbebengebieten: Ein Modell zur Beschreibung ihrer zeitlichen änderungen. Dissertation, 184 S., Inst. f. Geophys., C.-A.-Univ. Kiel.

Roth, F., 1988. Modeling of stress patterns along the western part of the North Anatolian Fault Zone. Tectonophys. 152, 215–226, spec. iss.: Seismic Source Physics and Earthquake Prediction Research, O. Kulhánek, Ed.

Roth, F., 1990. Subsurface deformations in a layered elastic half-space. Geophys. J. Int. 103 (2), 147–155.

Roth, F., 1992. Modellierung von Vorgängen an Verwerfungen mit Hilfe der Dislokationstheorie. Habilitationsschrift, Berichte Reihe A, Inst. f. Geophys., Ruhr-Univ. Bochum, 35.

Roth, F., 1993. Deformations in a layered crust due to a system of cracks: Modeling the effect of dike injections or dilatancy. J. Geophys. Res. 98, 4543–4551.

Roth, F., 1994. New methods using dislocation theory. Proceedings of the 8th Internat. Symp. on Recent Crustal Movements (CRCM '93) of IUGG and IAG, The Local Organizing Committee for the CRCM '93, Kobe, Dec. 6-11, 1993, spec. Iss. of J. of the Geod. Soc. of Japan.

Roy, M., Royden, L. H., 2000a. Crustal rheology and faulting at strike-slip plate boundaries, 1, An analytic model. J. Geophys. Res. 105 (B3), 5583–5597.

Roy, M., Royden, L. H., 2000b. Crustal rheology and faulting at strike-slip plate boundaries, 2, Effects of lower crustal flow. J. Geophys. Res. 105 (B3), 5599–5613.

Rundle, J. B., 1980a. Numerical evaluation of a static elastic-gravitational deformation of a layered half-space by point couple-sources. Rep., Sandia National Lab., Albuquerque, N.M., SAND 80-2048.

Rundle, J. B., 1980b. Static elastic-gravitational deformation of a layered half space by point couple sources. J. Geophys. Res. 85, 5355–5363.

Rundle, J. B., 1981. Vertical displacements from a rectangular fault in layered elastic-gravitational media. J. Phys. Earth 29, 173–186.

Rundle, J. B., 1982. Viscoelastic-gravitational deformation by a rectangular thrust fault in a layered Earth. J. Geophys. Res. 87, 7787–7796.

Şaroğlu, F., Emre, O., Kuşçu, I., 1992. Active fault map of Turkey. Ankara, Turkey: Geological Research Department of the General Directorate of Mineral Research and Exploration.

Sato, R., 1971. Crustal deformation due to a dislocation in a multi-layered medium. J. Phys. Earth 19, 31–46.

Sato, R., Matsu'ura, M., 1973. Static deformation due to the fault spreading over several layers in a multi-layered medium. Part I: Displacement. J. Phys. Earth 21, 227–249.

Savage, J. C., Plafker, G., 1991. Tide gage measurements of uplift along the south coast of Alaska. J. Geophys. Res. 96, 4325–4335.

Scholz, C. H., Campos, J., 1995. On the mechanism of seismic decoupling and back arc spreading at subduction zones. J. Geophys. Res. 100, 22103–22115.

Şengör, A., Tüysüz, O., Imren, C., Sakιnç, M., Eyidoğan, H., Görür, N., Pichon, X. L., Rangin, C., 2005. The North Anatolian Fault: A new look. Annual Review of Earth and Planetary Sciences 33, 37–112.

Şengör, A. M. C., Görür, N., Saroglu, F., 1985. Strike-slip faulting and related basin formation in zones of tectonic scape: Turkey as a case study. In: Biddle, T. R., Christi-Blick, N. (Eds.), Strike-slip deformation, basin formation and sedimentation. Soc. Econ. Paleontol. Mineral., pp. 227–264.

Singh, S. J., 1971. Deformation of a multilayered half-space by stress dislocations and concentrated forces. Bull. Seism. Soc. Am. 61, 1625–1637.

Singh, S. J., Rosenman, M., 1974. Quasi-static deformation of a viscoelastic half-space by a displacement dislocation. Phys. Earth Plan. Int. 8, 87–101.

Smith, W. H. F., Sandwell, D. T., 1997. Global seafloor topography from satellite altimetry and ship depth soundings. Science 277 (5334), 1956–1962.

Smylie, D. E., Mansinha, L., 1971. The elasticity theory of dislocations in real earth models and changes in rotation of the earth. Geophys. J. R. astr. Soc. 23, 329–354, see also: Reply to a comment of Dahlen (p. 355-358) on page 359.

Somoza, R., 1998. Updated Nazca (Farallon)-South America relative motions during the last 40 My: implications for mountain building in the central Andean region. J. South American Earth Sciences 11 (3), 211–215.

Steacy, S., Gomberg, J., Cocco, M., 2005. Introduction to special section: Stress transfer, earthquake triggering, and time-dependent seismic hazard. J. Geophys. Res. 110 (5), B05S01.

Steacy, S. J., McCloskey, J., 1998. What controls an earthquake's size? Results from a heterogeneous cellular automaton. Geophys. J. Int. 133 (1), F11.

Stein, R. S., 1999. The role of stress transfer in earthquake occurrence. Nature 402 (6762), 605–609.

Stein, R. S., Barka, A. A., Dieterich, J. H., 1997. Progressive failure on the North Anatolian fault since 1939 by earthquake stress triggering. Geophys. J. Int. 128 (3), 594–604.

Stein, R. S., King, G. C., Lin, J., 1992. Change in failure stress on the southern San Andreas fault system caused by the 1992 magnitude = 7.4 Landers earthquake. Science 258 (5086), 1328–1332.

Stein, R. S., King, G. C. P., Lin, J., 1994. Stress triggering of the 1994 M=6,7 Northridge, California, earthquake by its predecessors. Science 265, 1432–1435.

Talley, H. C., Cloud, W. K., 1962. United States Earthquakes 1960. U.S. Department of Commerce, Coast and Geodetic Survey - Washington, Washington, D.C.

Thatcher, W., Matsuda, T., Kato, T., Rundle, J. B., 1980. Lithosphere loading by the 1896 Riku-u earthquake, northern Japan: Implications for plate flexure and asthenospheric rheology. J. Geophys. Res. 85, 6429–6435.

Thatcher, W., Rundle, J. B., 1979. A model for the earthquake cycle in underthrust zones. J. Geophys. Res. 84, 5540–5556.

Thatcher, W., Rundle, J. R., 1984. A viscoelastic coupling model for the cyclic deformation due to periodically repeated earthquakes at subduction zones. J. Geophys. Res. 89, 7631–7640.

Thomson, W. T., 1950. Transmission of elastic waves through a stratified medium. J. appl. Phys. 21, 89–93.

Tibi, R., Bock, G., Xia, Y., Baumbach, M., Grosser, H., Milkereit, C., Karakısa, S., Zünbül, S., Kind, R., Zschau, J., 2001. Rupture processes of the 1999 August 17 Izmit and November 12 Düzce (Turkey) earthquakes. Geophys. J. Int. 144 (2), F1–F7.

Tichelaar, B. W., Ruff, L. J., 1991. Seismic coupling along the Chilean subduction zone. J. Geophys. Res. 96, 11997–12022.

Toda, S., Stein, R. S., Reasenberg, P. A., Dieterich, J. H., Yoshida, A., 1998. Stress transferred by the 1995 Mw=6.9 Kobe, Japan, shock: Effects on aftershocks and future earthquake probabilities. Journal of Geophysical Research 103 (B10), 24543–24565.

Toksöz, M. N., Shakal, A. F., Michael, A. J., 1979. Space-time migration of earthquakes along the North Anatolian fault zone and seismic gaps. Pageoph 117, 1258–1270.

Umutlu, N., Koketsu, K., Milkereit, C., 2004. The rupture process during the 1999 Düzce, Turkey, earthquake from joint inversion of teleseismic and strong-motion data. Tectonophysics 391 (1-4), 315–324, spec. iss. on "Active Faulting and Crustal Deformation in the Eastern Mediterranean Region", edited by: T. Taymaz, R. Westaway, R. Reilinger.

Utkucu, M., Nalbant, S. S., McCloskey, J., Steacy, S., Alptekin, Ö., 2003. Slip distribution and stress changes associated with the 1999 November 12, Düzce (Turkey) earthquake (Mw=7.1). Geophysical Journal International 153 (1), 229–241.

Uyeda, S., 1982. Subduction zones: An introduction to comparative subductology. Tectonophys. 81, 133–159.

Vermeersen, L. L. A., Sabadini, R., Devoti, R., Luceri, V., Rutigliano, P., Sciarretta, C., 1998. Mantle viscosity inferences from joint inversion of Pleistocene deglaciation-induced changes in geopotential with a new SLR analysis and polar wander. Geophys. Res. Lett. 25 (23), 4261–4264.

Wang, H., 1999a. Surface vertical displacements, potential perturbations and gravity changes of a viscoelastic earth model induced by internal point dislocations. Geophysical Journal International 137 (2), 429–440.

Wang, R., 1999b. A simple orthonormalization method for the stable and efficient computation of Green's functions. Bulletin of the Seismological Society of America 89, 733–741.

Wang, R., 2005a. On the singularity problem of the elastic-gravitational dislocation theory applied to plane-earth models. Geophys. Res. Lett. 32, citation no. L06307, 2 pp., doi: 10.1029/2003GL019358.

Wang, R., 2005b. The dislocation theory: a consistent way for including the gravity effect in (visco)elastic plane-earth models. Geophys. J. Int. 161 (1), 191–196, doi: 10.1111/j.1365-246X.2005.02614.x.

Wang, R., Kümpel, H.-J., 2003. Poroelasticity: Efficient modelling of strongly coupled, slow deformation processes in a multilayered half-space. Geophysics 68 (2), 705–717.

Wang, R., Lorenzo Martín, F., Roth, F., 2003. Computation of deformation induced by earthquakes in a multi-layered elastic crust - FORTRAN programs EDGRN / EDCMP. Computers and Geosciences 29 (2), 195–207.

Wang, R., Lorenzo Martín, F., Roth, F., 2006. PSGRN/PSCMP - a new code for calculating co- and post-seismic deformation, geoid and gravity changes based on the viscoelastic-gravitational dislocation theory. Computers and Geosciences , doi:10.1016/j.cageo.2005.08.006, in press, already available online.

Wason, H. R., Singh, S. J., 1972. Static deformation of multilayered sphere by internal sources. Geophys. J. R. astr. Soc. 27, 1–14.

Wright, T., Fielding, E., Parsons, B., 2001. Triggered slip: observations of the 17 August 1999 Izmit (Turkey) earthquake using radar interferometry. Geophys. Res. Lett. 28 (6), 1079–1082.

Yu, T.-T., Rundle, J. B., Fernández, J., 1996a. Deformation produced by a rectangular dipping fault in a viscoelastic-gravitational layered Earth model - Part II: Strike slip fault STRGRV and STRGRH FORTRAN programs. Computers & Geosciences 22, 751–764, corrigenda in C&G 28, p. 89-91, 2002.

Yu, T.-T., Rundle, J. B., Fernández, J., 1996b. Surface deformation due to a strike-slip fault in an elastic gravitational layer overlying a viscoelastic gravitational half-space. J. Geophys. Res. 101, 3199–3214, corrigenda in JGR, 104, B7, 15,313-5, 1999.

Zeng, Y., 2001. Viscoelastic stress-triggering of the 1999 Hector Mine earthquake by the 1992 Landers earthquake. Geophys. Res. Lett. 28 (15), 3007–3010.

Zweck, C., Freymueller, J. T., Cohen, S. C., 2002. Three-dimensional elastic dislocation modeling of the postseismic response to the 1964 Alaska earthquake. J. Geophys. Res. 107 (B4), ECV 1–1 to ECV 1–11, citation no. 2064, doi: 10.1029/2001JB000409.

Appendix A

Expansion of the deformation field equation in terms of poloidal and toroidal modes

A.1 Introduction to the Hankel transform

(Note: Throughout this Appendix, the dependency of functions on variables is often skipped for clarity, as long as this does not lead to misunderstandings. We will write, for instance, Y_k^m instead of $Y_k^m(r, \theta)$.)

The scalar cylindrical surface harmonics are defined by

$$Y_k^m(r, \theta) \;=\; J_m(kr)e^{im\theta}, \tag{A.1.1}$$

for $(0 \leq k < \infty,\ m \in \mathbb{Z})$, where $J_m(x)$ are the Bessel functions of the first kind. It is trivial to show the following recursive relationships, that will be repeatedly applied in the following sections

$$\begin{aligned} \frac{\partial^2 Y_k^m}{\partial r^2} + \frac{1}{r}\frac{\partial Y_k^m}{\partial r} - \frac{m^2}{r^2}Y_k^m \;&=\; -k^2 Y_k^m, && \text{(A.1.2)} \\ \frac{\partial^2 Y_k^m}{\partial \theta^2} \;&=\; -m^2 Y_k^m. && \text{(A.1.3)} \end{aligned}$$

We define the scalar Hankel transform (c.f. Bracewell, 1965, pp. 244) as

$$\boxed{s(r, \theta) = \sum_{m=0}^{\infty} \int\limits_0^{\infty} S_m(k) Y_k^m k dk, \qquad \text{(A.1.4)}}$$

where $S_m(k)$ are the wavenumber spectra of the scalar function $s(r, \theta)$.

A vector Hankel transform can be defined in a similar manner, where the vector harmonics are given by

$$\mathbf{Z}_k^m(r,\theta) \;=\; \mathbf{e}_z Y_k^m, \tag{A.1.5}$$

$$\mathbf{R}_k^m(r,\theta) \;=\; \left(\frac{\mathbf{e}_r}{k}\frac{\partial}{\partial r} + \frac{\mathbf{e}_\theta}{kr}\frac{\partial}{\partial \theta}\right) Y_k^m, \tag{A.1.6}$$

$$\mathbf{T}_k^m(r,\theta) \;=\; \left(\frac{\mathbf{e}_r}{kr}\frac{\partial}{\partial \theta} - \frac{\mathbf{e}_\theta}{k}\frac{\partial}{\partial r}\right) Y_k^m, \tag{A.1.7}$$

These vectors provide a complete and orthogonal base, and can be used to define the vector Hankel transform as follows

$$\boxed{\mathbf{V}(r,\theta) \;=\; \sum_m \int_0^\infty \left(A_m(k)\mathbf{Z}_k^m + B_m(k)\mathbf{R}_k^m + C_m(k)\mathbf{T}_k^m\right) k dk,} \tag{A.1.8}$$

where A_m, B_m and C_m are the wavenumber spectra of the vector function $\mathbf{V}(z,r,\theta)$. We need to obtain expressions for these spectra, as the inverse transform to that of Eq. A.1.8. For this, we will make use of the orthogonality property of the exponential function:

$$\int_0^{2\pi} e^{i\,m\,\theta}\, e^{-i\,m'\,\theta} d\theta = 2\pi\delta_{mm'}, \tag{A.1.9}$$

where $\delta_{mm'}$ is the Kronecker delta, and the closure equation of the Bessel functions of the first kind:

$$\int_0^\infty J_m(kr)\, J_m(k'r)\, r\, dr = \frac{1}{k}\,\delta(k-k'), \tag{A.1.10}$$

where $\delta(k-k')$ is the Dirac delta function.

Multiplying both sides of Eq. A.1.8 by $\overline{\mathbf{Z}_{k'}^{m'}}(r,\theta)$ (notation for the conjugate of $\mathbf{Z}_{k'}^{m'}(r,\theta)$), for $m' \in \mathbb{N}$ and $k' \in \mathbb{R}^+$, integrating and applying A.1.9, A.1.10 and the orthogonality of $\mathbf{Z}_k^m$, $\mathbf{R}_k^m$ and $\mathbf{T}_k^m$, we find

$$\begin{aligned}
\int_0^\infty\int_0^{2\pi} \mathbf{V}\cdot\overline{\mathbf{Z}_{k'}^{m'}} r d\theta dr &= \sum_m \int_0^\infty\int_0^\infty\int_0^{2\pi} A_m \mathbf{Z}_k^m \cdot \overline{\mathbf{Z}_{k'}^{m'}} k r d\theta dr dk \\
&= \sum_m \int_0^\infty A_m k \int_0^\infty\int_0^{2\pi} Y_k^m \overline{Y_{k'}^{m'}} r d\theta dr dk \\
&= \sum_m \int_0^\infty A_m k \int_0^\infty J_m(kr) J_{m'}(k'r) r \int_0^{2\pi} e^{im\theta} e^{-im'\theta} d\theta dr dk \\
&= 2\pi \int_0^\infty A_{m'}(z,k) k \int_0^\infty J_{m'}(kr) J_{m'}(k'r) r dr dk \\
&= 2\pi A_{m'}(z,k').
\end{aligned} \tag{A.1.11}$$

Dropping the apostrophe we therefore have

$$\boxed{A_m(z,k) = \frac{1}{2\pi}\int_0^{2\pi}\int_0^{\infty} V_z(z,r,\theta)\overline{Y_k^m}(r,\theta)\,r\,dr\,d\theta. \qquad \text{(A.1.12)}}$$

To obtain an expression for the wavenumber spectrum $B_m(z,k)$ we follow a similar procedure. Multiplying both sides of Eq. A.1.8 by $\overline{\mathbf{R}_{k'}^{m'}}(r,\theta)$ and integrating we find

$$\begin{aligned}
\int_0^{\infty}\int_0^{2\pi}\mathbf{V}\cdot\overline{\mathbf{R}_{k'}^{m'}}\,r\,d\theta\,dr &= \sum_m\int_0^{\infty}\int_0^{\infty}\int_0^{2\pi} B_m\mathbf{R}_k^m\cdot\overline{\mathbf{R}_{k'}^{m'}}\,k\,r\,d\theta\,dr\,dk \\
&= \sum_m\int_0^{\infty} B_m k\int_0^{\infty}\int_0^{2\pi}\frac{1}{kk'}\left[\frac{\partial Y_k^m}{\partial r}\frac{\partial\overline{Y_{k'}^{m'}}}{\partial r}+\frac{1}{r^2}\frac{\partial Y_k^m}{\partial\theta}\frac{\partial\overline{Y_{k'}^{m'}}}{\partial\theta}\right] r\,d\theta\,dr\,dk \\
&= \sum_m\int_0^{\infty} B_m k\int_0^{\infty}\int_0^{2\pi}\left[\frac{\partial J_m(kr)}{\partial r}\frac{\partial J_{m'}(k'r)}{\partial r}\right. \\
&\qquad\left.+\frac{m}{kr}J_m(kr)\frac{m'}{k'r}J_{m'}(k'r)\right]e^{i(m-m')\theta}\,r\,d\theta\,dr\,dk \\
&= 2\pi\int_0^{\infty} B_{m'}k\int_0^{\infty}\left[\frac{\partial J_{m'}(kr)}{\partial r}\frac{\partial J_{m'}(k'r)}{\partial r}\right. \\
&\qquad\left.+\frac{m}{kr}J_{m'}(kr)\frac{m'}{k'r}J_{m'}(k'r)\right] r\,dr\,dk. \qquad \text{(A.1.13)}
\end{aligned}$$

Now we can apply the following properties of the Bessel functions of the first kind

$$\begin{aligned}
\frac{\partial J_m(x)}{\partial x} &= \frac{1}{2}\left[J_{m-1}(x)-J_{m+1}(x)\right] \qquad \text{(A.1.14)} \\
\frac{m}{x}J_m(x) &= \frac{1}{2}\left[J_{m-1}(x)+J_{m+1}(x)\right]. \qquad \text{(A.1.15)}
\end{aligned}$$

These relationships, together with the orthogonality of the Bessel functions lead to

$$\begin{aligned}
\int_0^{\infty}\int_0^{2\pi}\mathbf{V}\cdot\overline{\mathbf{R}_{k'}^{m'}}\,r\,d\theta\,dr &= 2\pi\int_0^{\infty} B_{m'}k\int_0^{\infty}\frac{1}{2}\left[J_{m'-1}(kr)J_{m'-1}(k'r)\right. \\
&\qquad\left.+\,J_{m'+1}(kr)J_{m'+1}(k'r)\right] r\,dr\,dk \\
&= 2\pi\int_0^{\infty} B_{m'}\delta(k-k')\,dk \\
&= 2\pi B_{m'}(z,k'). \qquad \text{(A.1.16)}
\end{aligned}$$

Therefore

$$B_m(z,k) = \frac{1}{2\pi}\int_0^\infty\int_0^{2\pi} \mathbf{V}\cdot\overline{\mathbf{R}_k^m} r d\theta dr$$

$$= \frac{1}{2\pi}\int_0^\infty\int_0^{2\pi}\left[V_r(z,r,\theta)\frac{1}{k}\frac{\partial\overline{Y_k^m}(r,\theta)}{\partial r} + V_\theta(z,r,\theta)\frac{1}{kr}\frac{\partial\overline{Y_k^m}(r,\theta)}{\partial\theta}\right] r dr d\theta, \quad \text{(A.1.17)}$$

or, equivalently

$$\boxed{B_m(z,k) = \frac{1}{2\pi}\int_S \mathbf{V}\cdot\nabla\overline{Y_k^m}\, dS. \qquad \text{(A.1.18)}}$$

For $C_m(z,k)$ we make use of the property

$$\mathbf{T}_k^m(r,\theta) = \mathbf{R}_k^m(r,\theta)\times\mathbf{e}_z. \quad \text{(A.1.19)}$$

so that

$$\mathbf{T}_k^m\cdot\overline{\mathbf{T}_{k'}^{m'}} = (\mathbf{R}_k^m\times\mathbf{e}_z)\cdot(\overline{\mathbf{R}_{k'}^{m'}}\times\mathbf{e}_z), = \mathbf{R}_k^m\cdot\overline{\mathbf{R}_{k'}^{m'}} \quad \text{(A.1.20)}$$

and applying the previous calculations we find

$$C_m(z,k) = \int_0^\infty\int_0^{2\pi} \mathbf{V}\cdot\overline{\mathbf{T}_k^m} r d\theta dr$$

$$= \frac{1}{2\pi}\int_0^\infty\int_0^{2\pi}\left[V_r(z,r,\theta)\frac{1}{kr}\frac{\partial\overline{Y_k^m}(r,\theta)}{\partial\theta} - V_\theta(z,r,\theta)\frac{1}{k}\frac{\partial\overline{Y_k^m}(r,\theta)}{\partial r}\right] r dr d\theta, \quad \text{(A.1.21)}$$

or, equivalently

$$\boxed{C_m(z,k) = \frac{1}{2\pi}\int_S \mathbf{V}\cdot\left(\nabla\overline{Y_k^m}\times\mathbf{e}_z\right) dS. \qquad \text{(A.1.22)}}$$

A.2 Hankel transform of Hooke's law

Using tensor notation, Hooke's linear constitutive relation between stress and strain (cf. Ranalli, 1995, pp. 51) can be written as

$$\mathbf{\Gamma} \;=\; (\lambda\nabla\cdot\mathbf{u})\,\mathbf{I} + \mu\left(\nabla\mathbf{u} + (\nabla\mathbf{u})^t\right), \quad \text{(A.2.23)}$$

where $\mathbf{\Gamma}$ is the stress tensor, $\mathbf{I}$ is the unit tensor and $(\nabla\mathbf{u})^t$ denotes the tensor transpose of $\nabla\mathbf{u}$. In particular

$$\sigma_{zz} = (\lambda+2\mu)\frac{\partial u_z}{\partial z} + \lambda\left(\frac{\partial u_r}{\partial r} + \frac{1}{r}u_r + \frac{1}{r}\frac{\partial u_\theta}{\partial \theta}\right) = \lambda\Theta + 2\mu\epsilon_{zz}, \tag{A.2.24}$$

$$\tau_{zr} = \mu\left(\frac{\partial u_r}{\partial z} + \frac{\partial u_z}{\partial r}\right) = 2\mu\epsilon_{zr}, \tag{A.2.25}$$

$$\tau_{zr} = \mu\left(\frac{\partial u_\theta}{\partial z} + \frac{1}{r}\frac{\partial u_z}{\partial \theta}\right) = 2\mu\epsilon_{z\theta}, \tag{A.2.26}$$

where σ denotes normal stress, τ shear stress, ϵ strain and $\Theta = \nabla\cdot\mathbf{u}$ is the strain dilatation. These relations between stress components and the first derivatives of the displacement vector have their equivalent in the wavenumber domain, which can be obtained as we show in the following.

If we consider the vectors $\mathbf{u}(z,r,\theta)$ and $\mathbf{e}_z\cdot\mathbf{\Gamma}(z,r,\theta)$, we have the following Hankel transforms:

$$\mathbf{u}(z,r,\theta) = \sum_m \int_0^\infty \left(U_m\mathbf{Z}_k^m + V_m\mathbf{R}_k^m + W_m\mathbf{T}_k^m\right)kdk, \tag{A.2.27}$$

$$\mathbf{e}_z\cdot\mathbf{\Gamma}(z,r,\theta) = \sum_m \int_0^\infty \left(E_m\mathbf{Z}_k^m + F_m\mathbf{R}_k^m + G_m\mathbf{T}_k^m\right)kdk, \tag{A.2.28}$$

where $\mathbf{\Gamma}$ is the stress tensor and U_m, V_m, …are the wavenumber spectra of the displacement and stress field. These two Hankel transforms, together with the stress-strain relations given by Eqs. A.2.24 to A.2.26 will provide three expressions relating the first derivatives of the displacement wavenumber spectra with the stress and displacement spectra themselves.

A.2.1 Derivative of the displacement wavenumber spectrum $U_m(z,k)$

We consider the function $\left(\nabla\cdot\mathbf{u} - \frac{\partial u_z}{\partial z}\right)Y_k^m$ and integrate it between two arbitrary values of z, z_1 and z_2:

$$\begin{aligned}
&\int_{z_1}^{z_2}\int_S \left(\nabla\cdot\mathbf{u} - \frac{\partial u_z}{\partial z}\right)Y_k^m dSdz = \int_V \left(\nabla\cdot\mathbf{u} - \frac{\partial u_z}{\partial z}\right)Y_k^m dV \\
&= \int_V \left((\nabla\cdot\mathbf{u})\,Y_k^m + \mathbf{u}\cdot\nabla Y_k^m - \mathbf{u}\cdot\nabla Y_k^m\right)dV - \int_V \frac{\partial u_z}{\partial z}Y_k^m dV \\
&= \int_V \nabla\cdot\left(\mathbf{u}Y_k^m\right)dV - \int_{z_1}^{z_2}\int_S \mathbf{u}\cdot\nabla Y_k^m dV - \int_V \frac{\partial u_z}{\partial z}Y_k^m dV \\
&= I_1 - I_2 - I_3.
\end{aligned} \tag{A.2.29}$$

To calculate the first addend in the last integral, we can use the divergence theorem, which states that the volume integral of the divergence $\nabla\cdot\mathbf{F}$ of $\mathbf{F}$ over the volume V

and the surface integral of $\mathbf{F}$ over the boundary S of V are related by

$$\int_V (\nabla \cdot \mathbf{F})\, dV = \int_S \mathbf{F} \cdot d\mathbf{S}. \tag{A.2.30}$$

Therefore

$$\begin{aligned} I_1 &= \int_S \left(-\mathbf{e}_z \cdot \mathbf{u}|_{z_1} Y_k^m\right) dS + \int_S \left(\mathbf{e}_z \cdot \mathbf{u}|_{z_2} Y_k^m\right) dS \\ &= \int_S \left[u_z(z_2, r, \theta) Y_k^m - u_z(z_1, r, \theta) Y_k^m\right] dS \\ &= \int_S \int_{z_1}^{z_2} \frac{\partial u_z}{\partial z}\, dz\; Y_k^m dV = \int_V \frac{\partial u_z}{\partial z} Y_k^m dV = I_3. \end{aligned} \tag{A.2.31}$$

Hence, and since z_1 and z_2 can be any two arbitrary values, we have

$$\int_S \left(\nabla \cdot \mathbf{u} - \frac{\partial u_z}{\partial z}\right) Y_k^m dS = -\int_S \mathbf{u} \cdot \nabla Y_k^m dS \tag{A.2.32}$$

Applying this result to the expression for V_m corresponding to Eq. A.1.18, taking into account that Y_k^m does not depend on z and applying the expression for σ_{zz} given by Eq. A.2.24, we obtain

$$\begin{aligned} V_m(z,k) &= \frac{1}{\pi} \int_S \left[u_r(z,r) \frac{1}{k} \frac{\partial \overline{Y_k^m}(r,\theta)}{\partial r} + u_\theta(z,r) \frac{1}{kr} \frac{\partial \overline{Y_k^m}(r,\theta)}{\partial \theta}\right] dS \\ &= \frac{1}{2\pi k} \int_S \mathbf{u} \cdot \nabla_1 \overline{Y_k^m} dS \\ &= \frac{1}{2\pi k} \int_S \mathbf{u} \cdot \nabla \overline{Y_k^m} dS \\ &= -\frac{1}{2\pi k} \int_S \left(\nabla \cdot \mathbf{u} - \frac{\partial u_z}{\partial z}\right) \overline{Y_k^m} dS \\ &= -\frac{1}{2\pi k} \int_S \left(\frac{\partial u_r}{\partial r} + \frac{1}{r}\left(u_r + \frac{\partial u_\theta}{\partial \theta}\right)\right) \overline{Y_k^m} dS \\ &= \frac{1}{2\pi k} \int_S \left(\frac{\lambda + 2\mu}{\lambda} \frac{\partial u_z}{\partial z} - \frac{1}{\lambda} \sigma_{zz}\right) \overline{Y_k^m} dS, \end{aligned} \tag{A.2.33}$$

and therefore

$$\boxed{\frac{\partial U_m(z,k)}{\partial z} = \frac{1}{\lambda + 2\mu} E_m(z,k) + \frac{\lambda k}{\lambda + 2\mu} V_m(z,k).} \tag{A.2.34}$$

A.2.2 Derivative of the displacement wavenumber spectrum $V_m(z,k)$

The expression for V_m corresponding to Eq. A.1.18 can be differentiated to obtain

$$\begin{aligned}
\frac{\partial V_m}{\partial z}(z,k) &= \frac{1}{2\pi}\int_S \left(\frac{\partial u_r}{\partial z}\frac{1}{k}\frac{\partial \overline{Y_k^m}}{\partial r} + \frac{\partial u_\theta}{\partial z}\frac{1}{kr}\frac{\partial \overline{Y_k^m}}{\partial \theta}\right) dS \\
&= \frac{1}{\mu}\frac{1}{2\pi k}\int_S \left(\tau_{zr}\frac{\partial \overline{Y_k^m}}{\partial r} + \tau_{z\theta}\frac{1}{r}\frac{\partial \overline{Y_k^m}}{\partial \theta}\right) dS \\
&\quad -\frac{1}{2\pi k}\int_S \left(\frac{\partial u_z}{\partial r}\frac{\partial \overline{Y_k^m}}{\partial r} + \frac{1}{r^2}\frac{\partial u_z}{\partial \theta}\frac{\partial \overline{Y_k^m}}{\partial \theta}\right) dS \\
&= \frac{1}{\mu}F_m - I, \qquad \text{(A.2.35)}
\end{aligned}$$

where

$$I = \frac{1}{2\pi k}\int_S \left(\frac{\partial u_z}{\partial r}\frac{\partial \overline{Y_k^m}}{\partial r} + \frac{1}{r^2}\frac{\partial u_z}{\partial \theta}\frac{\partial \overline{Y_k^m}}{\partial \theta}\right) dS = \frac{1}{2\pi k}\int_s \nabla u_z \cdot \nabla \overline{Y_k^m} dS. \qquad \text{(A.2.36)}$$

To manipulate Eq. A.2.36 we will use the functions

$$y_k^m(z,r,\theta) = e^{-kz}Y_k^m(r,\theta). \qquad \text{(A.2.37)}$$

We have

$$\nabla Y_k^m = e^{kz}\nabla y_k^m + kY_k^m \mathbf{e}_z, \qquad \text{(A.2.38)}$$

and therefore

$$I = \frac{e^{kz}}{2\pi k}\int_S \nabla u_z \cdot \nabla \overline{y_k^m} dS + \frac{1}{2\pi}\int_S \nabla u_z \cdot \nabla\left(\overline{Y_k^m}\cdot \mathbf{e}_z\right) dS. \qquad \text{(A.2.39)}$$

Since y_k^m is a harmonic function, we find that

$$\nabla u_z \cdot \nabla \overline{y_k^m} = \nabla\cdot\left(u_z \nabla \overline{y_k^m}\right) - u_z \nabla^2 \overline{y_k^m} = \nabla\cdot\left(u_z \nabla \overline{y_k^m}\right), \qquad \text{(A.2.40)}$$

hence

$$I = \frac{e^{kz}}{2\pi k}\int_S \nabla\cdot\left(u_z \nabla \overline{y_k^m}\right) dS + \frac{1}{2\pi}\int_S \nabla u_z \cdot \nabla\left(\overline{Y_k^m}\cdot \mathbf{e}_z\right) dS. \qquad \text{(A.2.41)}$$

Integrating the first surface integral in the last expression between two arbitrary values of z, z_1 and z_2, and applying the divergence theorem, as stated in Eq. A.2.30, we find

$$\begin{aligned}
\int_{z_1}^{z_2}\int_S \nabla\cdot\left(u_z \nabla \overline{y_k^m}\right) dSdz &= \int_S \left[-\mathbf{e}_z\cdot\left(u_z \nabla \overline{y_k^m}\right)\Big|_{z_1} + \mathbf{e}_z\cdot\left(u_z \nabla \overline{y_k^m}\right)\Big|_{z_2}\right] dS \\
&= -k\int_S u_z \overline{y_k^m}\Big|_{z_1}^{z_2} dS \\
&= -k\int_S \int_{z_1}^{z_2} \frac{\partial\left(u_z \overline{y_k^m}\right)}{\partial z} dzdS \qquad \text{(A.2.42)}
\end{aligned}$$

and therefore

$$\begin{aligned}
\int_S \nabla \cdot \left(u_z \nabla \overline{y_k^m}\right) dS &= -k \int_S \frac{\partial \left(u_z \overline{y_k^m}\right)}{\partial z} dS \\
&= -k \int_S \frac{\partial u_z}{\partial z} \overline{y_k^m} dS + k^2 \int_S u_z \overline{y_k^m} dS \\
&= -k e^{-kz} \int_S \frac{\partial u_z}{\partial z} \overline{Y_k^m} dS + k^2 e^{-kz} \int_S u_z \overline{Y_k^m} dS \qquad \text{(A.2.43)}
\end{aligned}$$

Substituting

$$\begin{aligned}
I &= \frac{e^{kz}}{2\pi k} \int_S \nabla \cdot \left(u_z \nabla \overline{y_k^m}\right) dS + \frac{1}{2\pi} \int_S \frac{\partial u_z}{\partial z} \overline{Y_k^m} dS \\
&= -\frac{1}{2\pi} \int_S \frac{\partial u_z}{\partial z} \overline{Y_k^m} dS + \frac{k}{2\pi} \int_S u_z \overline{Y_k^m} dS + \frac{1}{2\pi} \int_S \frac{\partial u_z}{\partial z} \overline{Y_k^m} dS \\
&= \frac{k}{2\pi} \int_S u_z \overline{Y_k^m} dS = k \; U_m. \qquad \text{(A.2.44)}
\end{aligned}$$

Hence, we can finally write

$$\boxed{\frac{\partial V_m(z,k)}{\partial z} = \frac{1}{\mu} F_m(z,k) - k \, U_m(z,k). \qquad \text{(A.2.45)}}$$

A.2.3 Derivative of the displacement wavenumber spectrum $W_m(z,k)$

Finally, from the expression for W_m corresponding to Eq. A.1.22 we find

$$\begin{aligned}
\frac{\partial W_m}{\partial z}(z,k) &= \frac{1}{2\pi k} \int_S \left(\frac{\partial u_r}{\partial z} \frac{1}{r} \frac{\partial \overline{Y_k^m}}{\partial \theta} - \frac{\partial u_\theta}{\partial z} \frac{\partial \overline{Y_k^m}}{\partial r} \right) dS \\
&= \frac{1}{2\pi k} \int_S \left[\left(\frac{\partial u_r}{\partial z} + \frac{\partial u_z}{\partial r} \right) \frac{1}{r} \frac{\partial \overline{Y_k^m}}{\partial \theta} \right. \\
&\quad \left. - \left(\frac{\partial u_\theta}{\partial z} + \frac{1}{r} \frac{\partial u_z}{\partial \theta} \right) \frac{\partial \overline{Y_k^m}}{\partial r} \right] - \frac{1}{r} \left(\frac{\partial u_z}{\partial r} \frac{\partial \overline{Y_k^m}}{\partial \theta} - \frac{\partial u_z}{\partial \theta} \frac{\partial \overline{Y_k^m}}{\partial r} \right) dS \\
&= \frac{1}{2\pi k} \frac{1}{\mu} \int_S \left(\tau_{zr} \frac{1}{r} \frac{\partial \overline{Y_k^m}}{\partial \theta} - \tau_{z\theta} \frac{\partial \overline{Y_k^m}}{\partial r} \right) dS \\
&\quad - \frac{1}{2\pi k} \int_S \frac{1}{r} \left(\frac{\partial u_z}{\partial r} \frac{\partial \overline{Y_k^m}}{\partial \theta} - \frac{\partial u_z}{\partial \theta} \frac{\partial \overline{Y_k^m}}{\partial r} \right) dS \\
&= \frac{1}{\mu} G_m - \frac{1}{2\pi k} \int_S \nabla u_z \cdot \left(\nabla \overline{Y_k^m} \times \mathbf{e}_z \right) dS. \qquad \text{(A.2.46)}
\end{aligned}$$

The second integral can be manipulated as follows

$$\begin{aligned}&\int_S \nabla u_z \cdot \left(\nabla \overline{Y_k^m} \times \mathbf{e}_z\right) dS \\ &= \int_S \nabla \cdot \left(u_z \left(\nabla \overline{Y_k^m} \times \mathbf{e}_z\right)\right) - u_z \nabla \cdot \left(\nabla \overline{Y_k^m} \times \mathbf{e}_z\right) dS\end{aligned} \tag{A.2.47}$$

Using cartesian coordinates we find

$$\nabla \cdot \left(\nabla Y_k^m \times \mathbf{e}_z\right) = \nabla \cdot \left(\frac{\partial \overline{Y_k^m}}{\partial y}\mathbf{e}_x - \frac{\partial \overline{Y_k^m}}{\partial x}\mathbf{e}_y\right) = 0, \tag{A.2.48}$$

and hence

$$\int_S \nabla u_z \cdot \left(\nabla \overline{Y_k^m} \times \mathbf{e}_z\right) dS = \int_S \nabla \cdot \left(u_z \left(\nabla \overline{Y_k^m} \times \mathbf{e}_z\right)\right) dS \tag{A.2.49}$$

Using the divergence theorem once more, we have

$$\begin{aligned}&\int_{z_1}^{z_2} \int_S \nabla \cdot \left(u_z \left(\nabla \overline{Y_k^m} \times \mathbf{e}_z\right)\right) dS dz \\ &= \int_S -\mathbf{e}_z \cdot \left(u_z \left(\nabla \overline{Y_k^m} \times \mathbf{e}_z\right)\right)\Big|_{z_1} + \mathbf{e}_z \cdot \left(u_z \left(\nabla \overline{Y_k^m} \times \mathbf{e}_z\right)\right)\Big|_{z_2} dS.\end{aligned} \tag{A.2.50}$$

However, since $\nabla \overline{Y_k^m} \times \mathbf{e}_z$ is perpendicular to $\mathbf{e}_z$, the last integrand is always equal to zero. Therefore, we have

$$\boxed{\frac{\partial W_m(z,k)}{\partial z} = \frac{1}{\mu} G_m(z,k)} \tag{A.2.51}$$

In summary, Eqs. A.2.34, A.2.45 and A.2.51 provide the following system of equations:

$$\boxed{\left.\begin{aligned}\frac{\partial U_m(z,k)}{\partial z} &= \frac{1}{\lambda+2\mu} E_m(z,k) + \frac{\lambda k}{\lambda+2\mu} V_m(z,k) \\ \frac{\partial V_m(z,k)}{\partial z} &= \frac{1}{\mu} F_m(z,k) - k\, U_m(z,k) \\ \frac{\partial W_m(z,k)}{\partial z} &= \frac{1}{\mu} G_m(z,k)\end{aligned}\right\},} \tag{A.2.52}$$

which is the expression of Hooke's law in the wavenumber domain.

A.3 Hankel transform of the equations of motion

In addition to the three equations obtained by applying the Hankel transform to Hooke's law, we will also find three equations relating the displacement vector $\mathbf{u}(z,r,\theta)$

and its first and second derivatives. For this, we consider the equilibrium conditions of linear momentum (Eq. 2.7), given by

$$(\lambda + 2\mu)\,\nabla\,(\nabla\cdot\mathbf{u}) - \mu\nabla\times(\nabla\times\mathbf{u}) + \mathbf{f} \;=\; \mathbf{0}. \tag{A.3.53}$$

This equation relates the first and second partial derivatives of the displacement field $\mathbf{u}$ and the field itself. Although clear and compact in notation, this expression is not suitable for calculations. However, we can rewrite Eq. A.3.53 by means of the Hankel transform and taking into account the obtained relations obtained in the previous section. By doing this, we will transform this equation into an equivalent system of 6 equations on 6 variables. The variables will be the wavenumber spectra of the displacement and stress field, and the equations relating them will only include the spectra themselves and their first derivative with respect to z. Needless to say, such system of ordinary differential equations is more practical than the original Eq. A.3.53.

We consider the expressions for the vector Hankel transform of $\mathbf{u}(z,r,\theta)$ (Eq. A.1.8), as well as the scalar Hankel transform (Eq. A.1.4) for each of the components of $\mathbf{u}(z,r,\theta)$. Substitution of Eqs. A.1.5 to A.1.7 into Eq. A.1.8 gives

$$\begin{aligned}\mathbf{u}(z,r,\theta) \;=\; \sum_m \int_0^\infty \Bigg[& U_m\mathbf{e}_z + \frac{1}{k}\left(V_m\frac{\partial}{\partial r} + W_m\frac{1}{r}\frac{\partial}{\partial\theta}\right)\mathbf{e}_r \\ & + \frac{1}{k}\left(V_m\frac{1}{r}\frac{\partial}{\partial\theta} - W_m\frac{\partial}{\partial r}\right)\mathbf{e}_\theta\Bigg] Y_k^m k dk, \end{aligned} \tag{A.3.54}$$

We can now consider each of the three components from $\mathbf{u}(z,r,\theta)$ and obtain the following identities

$$u_z(z,r,\theta) \;=\; \sum_m \int_0^\infty U_m Y_k^m\, k\, dk, \tag{A.3.55}$$

$$\frac{\partial u_z}{\partial z} \;=\; \sum_m \int_0^\infty \frac{\partial U_m}{\partial z} Y_k^m\, k\, dk, \tag{A.3.56}$$

$$\frac{\partial u_z}{\partial r} \;=\; \sum_m \int_0^\infty U_m \frac{\partial Y_k^m}{\partial r}\, k\, dk, \tag{A.3.57}$$

$$\frac{\partial u_z}{\partial \theta} \;=\; \sum_m \int_0^\infty U_m \frac{\partial Y_k^m}{\partial \theta}\, k\, dk; \tag{A.3.58}$$

$$u_r(z,r,\theta) = \sum_m \int_0^\infty \left(V_m \frac{1}{k}\frac{\partial Y_k^m}{\partial r} + W_m \frac{1}{kr}\frac{\partial Y_k^m}{\partial \theta} \right) k\,dk, \tag{A.3.59}$$

$$\frac{\partial u_r}{\partial z} = \sum_m \int_0^\infty \left(\frac{\partial V_m}{\partial z}\frac{1}{k}\frac{\partial Y_k^m}{\partial r} + \frac{\partial W_m}{\partial z}\frac{1}{kr}\frac{\partial Y_k^m}{\partial \theta} \right) k\,dk, \tag{A.3.60}$$

$$\frac{\partial u_r}{\partial r} = \sum_m \int_0^\infty \left(V_m \frac{1}{k}\frac{\partial^2 Y_k^m}{\partial r^2} + W_m \left(\frac{1}{kr}\frac{\partial^2 Y_k^m}{\partial \theta \partial r} - \frac{1}{kr^2}\frac{\partial Y_k^m}{\partial \theta} \right) \right) k\,dk, \tag{A.3.61}$$

$$\frac{\partial u_r}{\partial \theta} = \sum_m \int_0^\infty \left(V_m \frac{1}{k}\frac{\partial^2 Y_k^m}{\partial r \partial \theta} - m^2 W_m \frac{1}{kr} Y_k^m \right) k\,dk; \tag{A.3.62}$$

$$u_\theta(z,r,\theta) = \sum_m \int_0^\infty \left(V_m \frac{1}{kr}\frac{\partial Y_k^m}{\partial \theta} - W_m \frac{1}{k}\frac{\partial Y_k^m}{\partial r} \right) k\,dk, \tag{A.3.63}$$

$$\frac{\partial u_\theta}{\partial z} = \sum_m \int_0^\infty \left(\frac{\partial V_m}{\partial z}\frac{1}{kr}\frac{\partial Y_k^m}{\partial \theta} - \frac{\partial W_m}{\partial z}\frac{1}{k}\frac{\partial Y_k^m}{\partial r} \right) k\,dk, \tag{A.3.64}$$

$$\frac{\partial u_\theta}{\partial r} = \sum_m \int_0^\infty \left(V_m \left(\frac{1}{kr}\frac{\partial^2 Y_k^m}{\partial r \partial \theta} - \frac{1}{kr^2}\frac{\partial Y_k^m}{\partial \theta} \right) - W_m \frac{1}{k}\frac{\partial^2 Y_k^m}{\partial r^2} \right) k\,dk, \tag{A.3.65}$$

$$\frac{\partial u_\theta}{\partial \theta} = \sum_m \int_0^\infty \left(-m^2 V_m \frac{1}{kr} Y_k^m - W_m \frac{1}{k}\frac{\partial^2 Y_k^m}{\partial r \partial \theta} \right) k\,dk. \tag{A.3.66}$$

In cylindrical coordinates, we have

$$\nabla \cdot \mathbf{u} = \frac{\partial u_z}{\partial z} + \frac{\partial u_r}{\partial r} + \frac{1}{r}\left(u_r + \frac{\partial u_\theta}{\partial \theta} \right) \tag{A.3.67}$$

Substituting from Eqs. A.3.55 to A.3.66 and applying the relationship given by Eq. A.1.2 we find

$$\begin{aligned} \nabla \cdot \mathbf{u} &= \sum_m \int_0^\infty \left[\frac{\partial U_m}{\partial z} Y_k^m + V_m \frac{\partial^2 Y_k^m}{\partial r^2} + W_m \left(\frac{1}{r}\frac{\partial^2 Y_k^m}{\partial \theta \partial r} - \frac{1}{r^2}\frac{\partial Y_k^m}{\partial \theta} \right) \right. \\ &\quad \left. + \frac{1}{r}\left(V_m \frac{\partial Y_k^m}{\partial r} + W_m \frac{1}{r}\frac{\partial Y_k^m}{\partial \theta} \right) + \frac{1}{r}\left(-m^2 V_m \frac{1}{r} Y_k^m - W_m \frac{\partial^2 Y_k^m}{\partial r \partial \theta} \right) \right] k\,dk \\ &= \sum_m \int_0^\infty \frac{\partial U_m}{\partial z} Y_k^m + V_m \left(\frac{\partial^2 Y_k^m}{\partial r^2} + \frac{1}{r}\frac{\partial Y_k^m}{\partial r} - \frac{m^2}{r^2} Y_k^m \right) dk \\ &= \sum_m \int_0^\infty \left(\frac{\partial U_m}{\partial z} - k V_m \right) Y_k^m k dk. \end{aligned} \tag{A.3.68}$$

Therefore

$$\nabla\left(\nabla\cdot\mathbf{u}\right)=\frac{\partial\nabla\cdot\mathbf{u}}{\partial z}\mathbf{e}_z+\frac{\partial\nabla\cdot\mathbf{u}}{\partial r}\mathbf{e}_r+\frac{1}{r}\frac{\partial\nabla\cdot\mathbf{u}}{\partial\theta}\mathbf{e}_\theta, \tag{A.3.69}$$

where

$$\frac{\partial\nabla\cdot\mathbf{u}}{\partial z} = \sum_m\int_0^\infty\left(\frac{\partial^2U_m}{\partial z^2}-k\frac{\partial V_m}{\partial z}\right)Y_k^m kdk, \tag{A.3.70}$$

$$\frac{\partial\nabla\cdot\mathbf{u}}{\partial r} = \sum_m\int_0^\infty\left(\frac{\partial U_m}{\partial z}-kV_m\right)\frac{\partial Y_k^m}{\partial r}kdk, \tag{A.3.71}$$

$$\frac{1}{r}\frac{\partial\nabla\cdot\mathbf{u}}{\partial\theta} = \sum_m\int_0^\infty\left(\frac{\partial U_m}{\partial z}-kV_m\right)\frac{\partial Y_k^m}{\partial\theta}kdk. \tag{A.3.72}$$

Using the expressions Eqs. A.1.5 to A.1.7 for the cylindrical surface harmonics, we obtain

$$\boxed{\nabla\left(\nabla\cdot\mathbf{u}\right)=\sum_m\int_0^\infty\left(\left(\frac{\partial^2U_m}{\partial z^2}-k\frac{\partial V_m}{\partial z}\right)\mathbf{Z}_k^m+k\left(\frac{\partial U_m}{\partial z}-kV_m\right)\mathbf{R}_k^m\right)k\,dk} \tag{A.3.73}$$

Similarly, the curl of **u** in cylindrical coordinates can be calculated as

$$\nabla\times\mathbf{u}=\frac{1}{r}\begin{vmatrix}\mathbf{e}_z & \mathbf{e}_r & r\mathbf{e}_\theta\\ \frac{\partial}{\partial z} & \frac{\partial}{\partial r} & \frac{\partial}{\partial\theta}\\ u_z & u_r & ru_\theta\end{vmatrix}=\mathbf{a} \tag{A.3.74}$$

Again, substituting from Eqs. A.3.55 to A.3.66 into A.3.74 and applying Eq. A.1.2

$$\begin{aligned}
a_z &= \frac{\partial u_\theta}{\partial r} + \frac{1}{r}\left(u_\theta - \frac{\partial u_r}{\partial \theta}\right) \\
&= \sum_m \int_0^\infty \left[V_m \left(\frac{1}{r}\frac{\partial^2 Y_k^m}{\partial r \partial \theta} - \frac{1}{r^2}\frac{\partial Y_k^m}{\partial \theta} \right) - W_m \frac{\partial^2 Y_k^m}{\partial r^2} \right. \\
&\quad \left. + \frac{1}{r}\left(V_m \frac{1}{r}\frac{\partial Y_k^m}{\partial \theta} - W_m \frac{\partial Y_k^m}{\partial r} - V_m \frac{\partial^2 Y_k^m}{\partial r \partial \theta} + m^2 W_m \frac{1}{r} Y_k^m \right)\right] dk \\
&= \sum_m \int_0^\infty \left(\frac{m^2}{r^2} Y_k^m - \frac{\partial^2 Y_k^m}{\partial r^2} - \frac{1}{r}\frac{\partial Y_k^m}{\partial r} \right) W_m dk \\
&= \sum_m \int_0^\infty W_m Y_k^m k^2 dk, \qquad \text{(A.3.75)}
\end{aligned}$$

$$\begin{aligned}
a_r &= \frac{1}{r}\frac{\partial u_z}{\partial \theta} - \frac{\partial u_\theta}{\partial z} \\
&= \sum_m \int_0^\infty \left(\frac{\partial W_m}{\partial z}\frac{\partial Y_k^m}{\partial r} + \left(U_m k - \frac{\partial V_m}{\partial z} \right) \frac{1}{r}\frac{\partial Y_k^m}{\partial \theta} \right) dk, \qquad \text{(A.3.76)}
\end{aligned}$$

$$\begin{aligned}
a_\theta &= \frac{\partial u_r}{\partial z} - \frac{\partial u_z}{\partial r} \\
&= \sum_m \int_0^\infty \left(\frac{\partial W_m}{\partial z}\frac{1}{r}\frac{\partial Y_k^m}{\partial \theta} - \left(U_m k - \frac{\partial V_m}{\partial z} \right) \frac{\partial Y_k^m}{\partial r} \right) dk. \qquad \text{(A.3.77)}
\end{aligned}$$

Expressions A.3.75 to A.3.77 can be used to calculate the following partial derivatives

$$\begin{aligned}
\frac{\partial a_z}{\partial r} &= \sum_m \int_0^\infty W_m \frac{\partial Y_k^m}{\partial r} k^2 dk, \qquad \text{(A.3.78)} \\
\frac{\partial a_z}{\partial \theta} &= \sum_m \int_0^\infty W_m \frac{\partial Y_k^m}{\partial \theta} k^2 dk, \qquad \text{(A.3.79)} \\
\frac{\partial a_r}{\partial z} &= \sum_m \int_0^\infty \left(\frac{\partial^2 W_m}{\partial z^2}\frac{\partial Y_k^m}{\partial r} + \left(\frac{\partial U_m}{\partial z} k - \frac{\partial^2 V_m}{\partial z^2} \right) \frac{1}{r}\frac{\partial Y_k^m}{\partial \theta} \right) dk, \qquad \text{(A.3.80)} \\
\frac{\partial a_r}{\partial \theta} &= \sum_m \int_0^\infty \left(\frac{\partial W_m}{\partial z}\frac{\partial^2 Y_k^m}{\partial r \partial \theta} - m^2 \frac{1}{r} \left(U_m k - \frac{\partial V_m}{\partial z} \right) Y_k^m \right) dk, \qquad \text{(A.3.81)}
\end{aligned}$$

$$\frac{\partial a_\theta}{\partial z} = \sum_m \int_0^\infty \left(\frac{\partial^2 W_m}{\partial z^2} \frac{1}{r} \frac{\partial Y_k^m}{\partial \theta} - \left(\frac{\partial U_m}{\partial z} k - \frac{\partial^2 V_m}{\partial z^2} \right) \frac{\partial Y_k^m}{\partial r} \right) dk, \tag{A.3.82}$$

$$\begin{aligned} \frac{\partial a_\theta}{\partial r} = & \sum_m \int_0^\infty \left(\frac{\partial W_m}{\partial z} \left(\frac{1}{r} \frac{\partial^2 Y_k^m}{\partial r \partial \theta} - \frac{1}{r^2} \frac{\partial Y_k^m}{\partial \theta} \right) \right. \\ & \left. - \left(U_m k - \frac{\partial V_m}{\partial z} \right) \frac{\partial^2 Y_k^m}{\partial r^2} \right) dk, \end{aligned} \tag{A.3.83}$$

which need to be considered when calculating $\nabla \times (\nabla \times \mathbf{u})$

$$\nabla \times (\nabla \times \mathbf{u}) = \nabla \times \mathbf{a} = \frac{1}{r} \begin{vmatrix} \mathbf{e}_z & \mathbf{e}_r & r\mathbf{e}_\theta \\ \frac{\partial}{\partial z} & \frac{\partial}{\partial r} & \frac{\partial}{\partial \theta} \\ a_z & a_r & r\, a_\theta \end{vmatrix} = \mathbf{b} \tag{A.3.84}$$

Substitution of the expressions A.3.80 to A.3.83 into A.3.84 gives

$$\begin{aligned} b_z = & \frac{\partial a_\theta}{\partial r} + \frac{1}{r} \left(a_\theta - \frac{\partial a_r}{\partial \theta} \right) \\ = & \sum_m \int_0^\infty \left[\frac{\partial W_m}{\partial z} \left(\frac{1}{r} \frac{\partial^2 Y_k^m}{\partial r \partial \theta} - \frac{1}{r^2} \frac{\partial Y_k^m}{\partial \theta} \right) - \left(U_m k - \frac{\partial V_m}{\partial z} \right) \frac{\partial^2 Y_k^m}{\partial r^2} \right. \\ & + \frac{1}{r} \left(\frac{\partial W_m}{\partial z} \frac{1}{r} \frac{\partial Y_k^m}{\partial \theta} - \left(U_m k - \frac{\partial V_m}{\partial z} \right) \frac{\partial Y_k^m}{\partial r} \right. \\ & \left. \left. - \frac{\partial W_m}{\partial z} \frac{\partial^2 Y_k^m}{\partial r \partial \theta} + m^2 \frac{1}{r} \left(U_m k - \frac{\partial V_m}{\partial z} \right) Y_k^m \right) \right] dk \\ = & \sum_m \int_0^\infty \left(\frac{\partial V_m}{\partial z} - U_m k \right) \left(\frac{\partial^2 Y_k^m}{\partial r^2} + \frac{1}{r} \frac{\partial Y_k^m}{\partial r} - \frac{m^2}{r^2} Y_k^m \right) dk \\ = & \sum_m \int_0^\infty \left(U_m k - \frac{\partial V_m}{\partial z} \right) Y_k^m k^2 dk, \end{aligned} \tag{A.3.85}$$

$$\begin{aligned} b_r = & \frac{1}{r} \frac{\partial a_z}{\partial \theta} - \frac{\partial a_\theta}{\partial z} \\ = & \sum_m \int_0^\infty \left(\left(\frac{\partial U_m}{\partial z} k - \frac{\partial^2 V_m}{\partial z^2} \right) \frac{\partial Y_k^m}{\partial r} + \left(k^2 W_m - \frac{\partial^2 W_m}{\partial z^2} \right) \frac{1}{r} \frac{\partial Y_k^m}{\partial \theta} \right) dk, \end{aligned} \tag{A.3.86}$$

$$\begin{aligned} b_\theta = & \frac{\partial a_r}{\partial z} - \frac{\partial a_z}{\partial r} \\ = & \sum_m \int_0^\infty \left(\left(\frac{\partial U_m}{\partial z} k - \frac{\partial^2 V_m}{\partial z^2} \right) \frac{1}{r} \frac{\partial Y_k^m}{\partial \theta} - \left(k^2 W_m - \frac{\partial^2 W_m}{\partial z^2} \right) \frac{\partial Y_k^m}{\partial r} \right) dk. \end{aligned} \tag{A.3.87}$$

Using the expressions Eqs. A.1.5 to A.1.7 for the cylindrical surface harmonics, we can hence write $\nabla \times (\nabla \times \mathbf{u})$ as

$$\begin{aligned}\nabla \times (\nabla \times \mathbf{u}) = \sum_m \int_0^\infty \Bigg[& k^2 \left(U_m k - \frac{\partial V_m}{\partial z} \right) Y_k^m \mathbf{e}_z \\ & + \left(\left(\frac{\partial U_m}{\partial z} k - \frac{\partial^2 V_m}{\partial z^2} \right) \frac{\partial Y_k^m}{\partial r} + \left(k^2 W_m - \frac{\partial^2 W_m}{\partial z^2} \right) \frac{1}{r} \frac{\partial Y_k^m}{\partial \theta} \right) \mathbf{e}_r \\ & + \left(\left(\frac{\partial U_m}{\partial z} k - \frac{\partial^2 V_m}{\partial z^2} \right) \frac{1}{r} \frac{\partial Y_k^m}{\partial \theta} - \left(k^2 W_m - \frac{\partial^2 W_m}{\partial z^2} \right) \frac{\partial Y_k^m}{\partial r} \right) \mathbf{e}_\theta \Bigg] dk, \quad \text{(A.3.88)}\end{aligned}$$

that is

$$\boxed{\begin{aligned}\nabla \times (\nabla \times \mathbf{u}) = \sum_m \int_0^\infty \Bigg[& k \left(U_m k - \frac{\partial V_m}{\partial z} \right) \mathbf{Z}_k^m \\ & + \left(\frac{\partial U_m}{\partial z} k - \frac{\partial^2 V_m}{\partial z^2} \right) \mathbf{R}_k^m + \left(k^2 W_m - \frac{\partial^2 W_m}{\partial z^2} \right) \mathbf{T}_k^m \Bigg] k dk. \quad \text{(A.3.89)}\end{aligned}}$$

Since $(\mathbf{Z}_k^m, \mathbf{R}_k^m, \mathbf{T}_k^m)$ form an orthogonal vector basis, when substituting Eqs. A.3.73 and A.3.89 into the equation of motion given by Eq. A.3.53, we can split each of the three components, finding that the equation of motion in the wavenumber domain can be written as the following system

$$\boxed{\left.\begin{aligned}(\lambda + 2\mu) \tfrac{\partial^2 U_m}{\partial z^2} - (\lambda + \mu) k \tfrac{\partial V_m}{\partial z} - \mu k^2 U_m = 0 \\ \mu \tfrac{\partial^2 V_m}{\partial z^2} + (\lambda + \mu) k \tfrac{\partial U_m}{\partial z} - (\lambda + 2\mu) k^2 V_m = 0 \\ \mu k^2 W_m - \mu \tfrac{\partial^2 W_m}{\partial z^2} = 0\end{aligned}\right\} . \quad \text{(A.3.90)}}$$

For the source conditions we need to substitute the right side of the latter homogeneous system by the source functions, which depend upon the body force **f** used to describe the source. For a single force and a point dislocation, Table 2.1 shows the Hankel transformed source functions.

A.4 The poloidal- and toroidal-mode systems

The relations given by Eqs. A.3.90 and the relationships found for the first derivatives of U_m, V_m and W_m, Eqs. A.2.52 can be combined as follows. Deriving Eq. A.2.52a and using Eq. A.3.90a, we find

$$\begin{aligned}\frac{\partial E_m(z,k)}{\partial z} &= (\lambda + 2\mu) \frac{\partial^2 U_m(z,k)}{\partial z^2} - \lambda k \frac{\partial V_m(z,k)}{\partial z} \\ &= \mu k \frac{\partial V_m(z,k)}{\partial z} + \mu k^2 U_m(z,k) - L_m(z,k) \\ &= k F_m(z,k) - L_m(z,k). \quad \text{(A.4.91)}\end{aligned}$$

The derivative of Eq. A.2.52b can be combined with Eq. A.3.90b as follows

$$\begin{aligned}\frac{\partial F_m(z,k)}{\partial z} &= \mu\frac{\partial^2 V_m(z,k)}{\partial z^2} + \mu k\frac{\partial U_m(z,k)}{\partial z} \\ &= -\lambda k\frac{\partial U_m(z,k)}{\partial z} + (\lambda+2\mu)\,k^2 V_m(z,k) - M_m(z,k) \\ &= -\frac{\lambda k}{\lambda+2\mu}E_m(z,k) + \frac{4\mu\,(\lambda+\mu)\,k^2}{\lambda+2\mu}V_m(z,k) - M_m(z,k). \qquad \text{(A.4.92)}\end{aligned}$$

Finally, the derivative of Eq. A.2.52c combined with Eq. A.3.90c give

$$\frac{\partial G_m(z,k)}{\partial z} = \mu k^2 W_m(z,k) + N_m(z,k). \qquad \text{(A.4.93)}$$

Defining the vectors $\mathbf{y}_m = (U_m, E_m, V_m, F_m)^t$ and $\mathbf{x}_m = (W_m, G_m)^t$ we can write the last three results in matrix format, together with those from Eqs. A.2.52:

$$\frac{d}{dz}\mathbf{y}_m = \mathbf{A}\,\mathbf{y}_m, \qquad \text{(A.4.94)}$$

$$\mathbf{A} = \begin{pmatrix} 0 & \frac{1}{\lambda+2\mu} & \frac{\lambda k}{\lambda+2\mu} & 0 \\ 0 & 0 & 0 & k \\ -k & 0 & 0 & \frac{1}{\mu} \\ 0 & -\frac{\lambda k}{\lambda+2\mu} & \frac{4k^2\mu\,(\lambda+\mu)}{\lambda+2\mu} & 0 \end{pmatrix}; \qquad \text{(A.4.95)}$$

$$\frac{d}{dz}\mathbf{x}_m = \mathbf{B}\,\mathbf{x}_m, \qquad \text{(A.4.96)}$$

$$\mathbf{B} = \begin{pmatrix} 0 & \frac{1}{\mu} \\ \mu k^2 & 0 \end{pmatrix}. \qquad \text{(A.4.97)}$$

which are the poloidal- and toroidal-mode systems of ordinary differential equations.

Appendix B

Previous published modeling results for gravitational viscoelastic post-seismic relaxation on a layered Earth model

This appendix compiles four figures displaying results from Pollitz (1997), obtained by means of his layered spherical model (Figs. B.1 and B.2), as well as two figures from the work of Rundle (1982), showing his modeling results using his layered viscoelastic gravitational half-space model (Fig. B.3). Both Pollitz's and Rundle's approaches are still widely used and accepted. For this reason, we compared the results from our modeling method to these. The results from our calculations can be seen in Figs. 2.6, which is comparable to Figs. 9 and 10 from Pollitz (1997) (Fig. B.2 in this Appendix), and Fig. 2.7, comparable with Figs. 3 and 6 from Pollitz (1997) (Fig. B.1 in this Appendix) and with Figs. 6 and 7 from Rundle (1982) (Fig. B.3 in this Appendix).

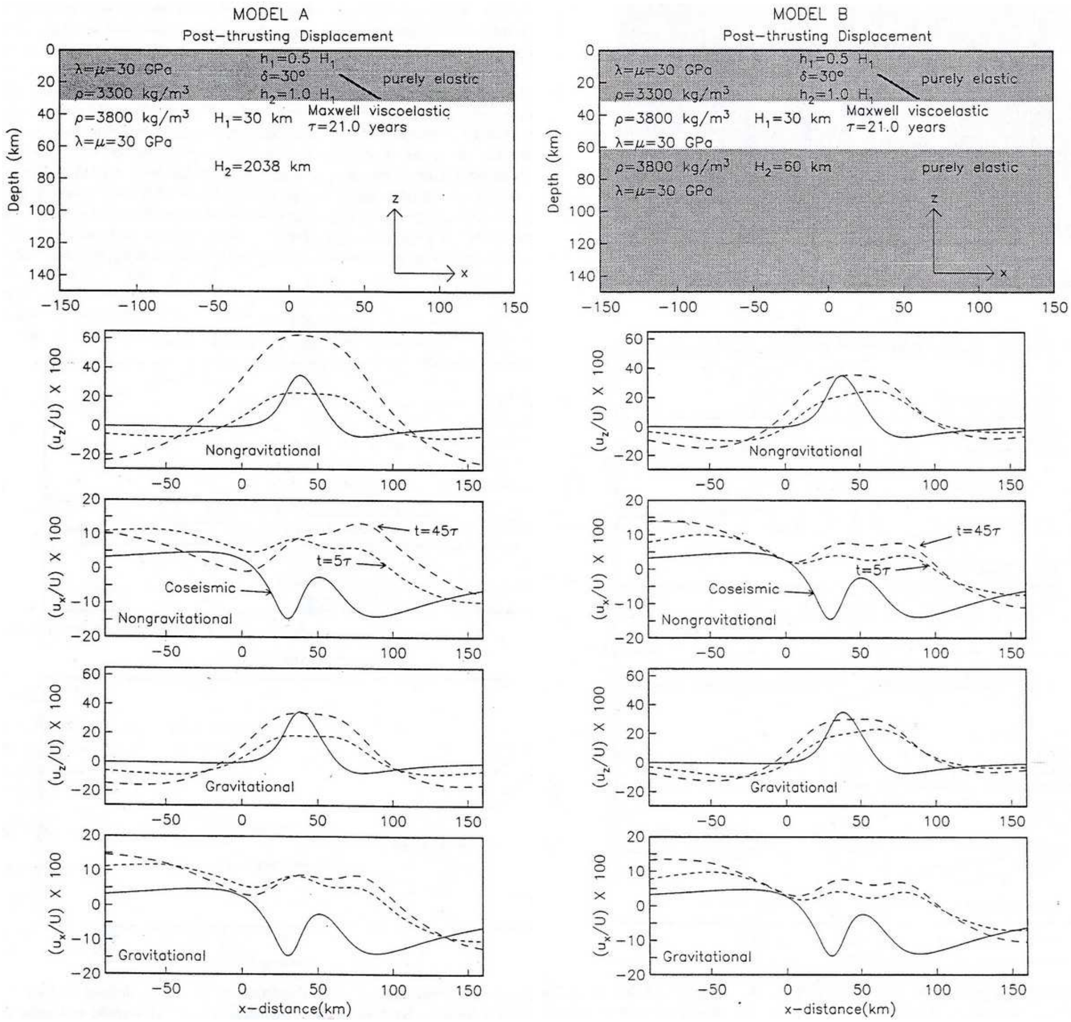

Figure B.1: *(Figs. 3 and 6 from Pollitz (1997)) Co-seismic and additional post-thrusting displacement at the surface predicted by Model A (top left) and B (top right) on a profile perpendicular to the fault strike and bisecting the fault plane. U represents the magnitude of slip on the fault plane, and u_x and u_z are displacement perpendicular to the fault strike and in the vertical direction, respectively. Variables λ and μ are the Lame parameters, and ρ is the density.*

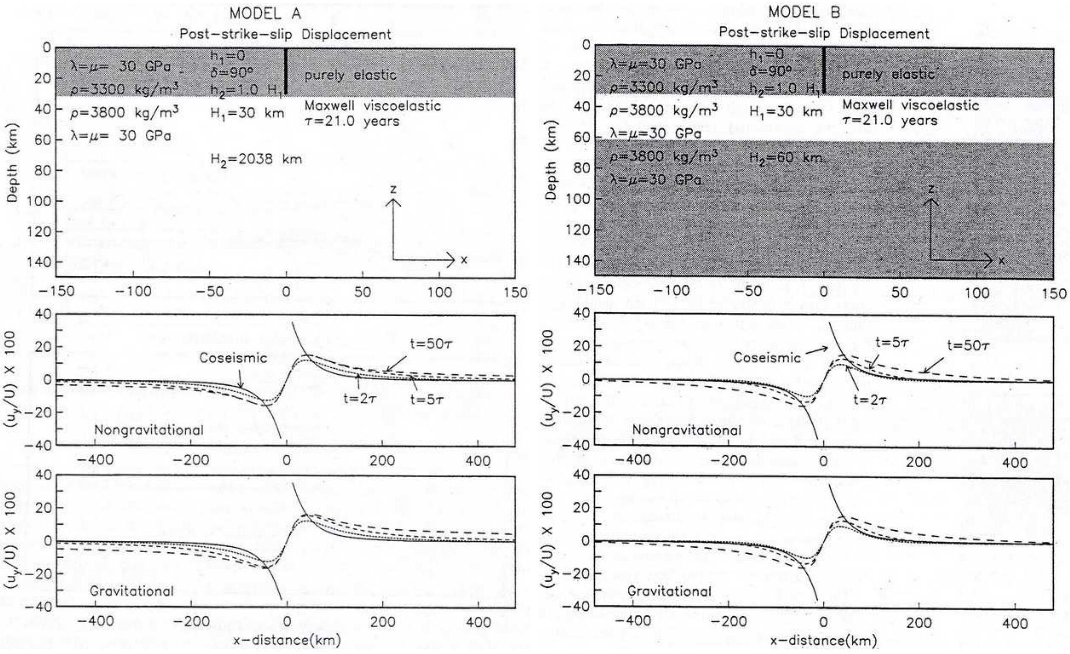

Figure B.2: *(Figs. 9 and 10 from Pollitz (1997)) Co-seismic and post-strike-slip displacement predicted by Model A (top left) and B (top right). Symbols are as defined in Fig. B.1.*

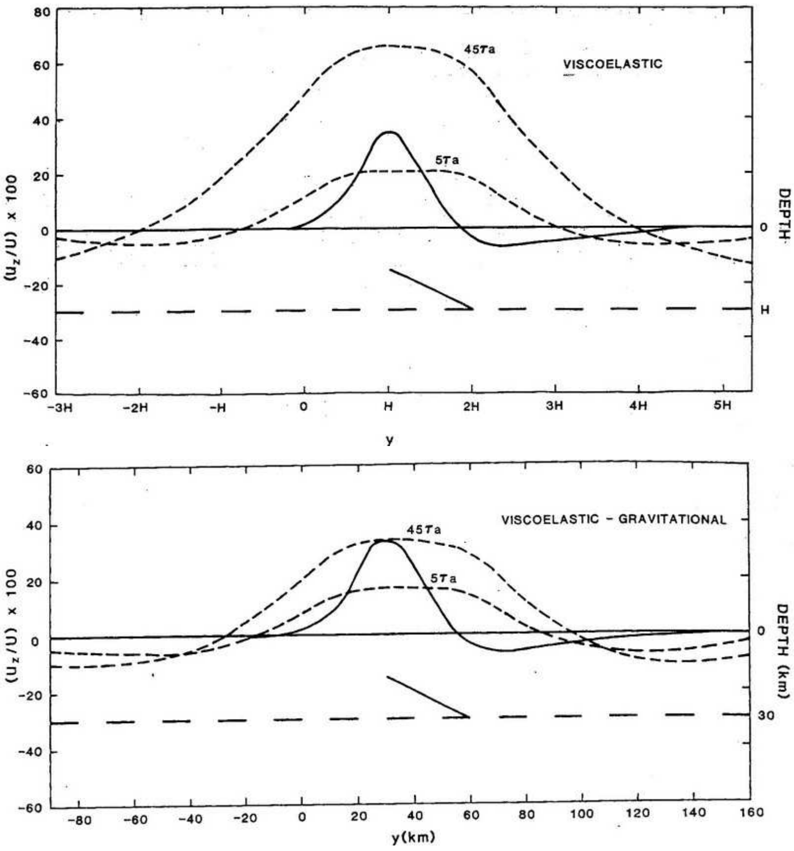

Figure B.3: *(Figs. 6 and 7 from Rundle (1982)) Surface displacements due to a 30º dipping thrust fault in an elastic layer over a viscoelastic half-space (upper panel) and in an elastic-gravitational layer over a viscoelastic-gravitational half-space (lower panel). Long-dashed line is layer-half-space boundary, slanted line is edge-on view of fault plane. Fault is* $2L = 20H/3$ *long,* $D = H/2$*, and* $W = H$ *(*$2L$ *is the length of the fault along strike,* W *is its width,* D *is the depth of its upper limit and* H *is the thickness of the elastic layer). Solid curve is the initial co-seismic displacement, short-dashed curves show changes in surface displacements due to viscoelastic stress relaxation after* $5\tau_\alpha$ *and* $45\tau_\alpha$*. Left vertical axis is cm/m of slip, horizontal axis is distance normal to fault strike, and right vertical axis is depth.*